Abstract

Black Hole Growth and Host Galaxy Co-Evolution Over 8 Billion Years of Cosmic Time

Brooke D Simmons

2012

Although much progress has been made in the investigation of the co-evolution of black holes and galaxies, the nature of AGN accretion triggers and AGN-host feedback remain open questions. Using samples of hard X-ray selected, moderate-luminosity AGN and their host galaxies from $0.25 < z < 2.67$ in the GOODS deep multi-wavelength survey fields, this thesis assesses the growth rates and histories of these black holes, and uses their host galaxy morphologies and colors to test the applicability of established quasar-triggering models to lower-powered AGN. The analysis includes simulations of over 50,000 AGN+host galaxy images to assess the reliability of AGN-host decomposition, as well as a new technique to separate the spectral energy distribution of an obscured AGN from its dominant host galaxy.

Moderate-luminosity AGN span a range of growth rates but are typically in a phase of slow growth (with $\approx 80\%$ of the sample growing at less than 10% of the Eddington limit) with relatively high black hole masses ($\approx 75\%$ of the sample has $M_{\mathrm{BH}} > 5 \times 10^7 M_{\odot}$), implying that they must have been growing at higher rates in the past in order to grow to the masses we observe. Additionally, a significant fraction of the host galaxies of moderate-luminosity AGN are disk-dominated: at the highest redshifts of the sample more than half of the host galaxies have at least 80% of their optical light from a disk. A further one-quarter to one-third of the sample (depending on redshift) has a significant disk contribution, with a stronger, but likely not dominant, bulge. Because major mergers both form bulges and destroy disks, this result indicates

that models requiring major mergers to trigger the growth of black holes do not describe the majority of AGN. The range of both black hole growth rates and host galaxy colors and morphologies in the sample imply that secular processes are important to the growth of moderate-luminosity AGN, which collectively comprise a substantial fraction of the overall black hole growth in the universe.

Black Hole Growth and Host Galaxy

Co-Evolution Over 8 Billion Years of Cosmic

Time

A Dissertation
Presented to the Faculty of the Graduate School
of
Yale University
in Candidacy for the Degree of
Doctor of Philosophy

by
Brooke D Simmons

Dissertation Directors: C. Megan Urry

December 2012

Acknowledgments

Some people bring a single-minded determination to their first day of graduate school and apply it continuously, never wavering in their path, untouched by uncertainty or the vicissitudes of life.

Me? Not so much.

My particular path to the PhD means I have a lot of people to thank. I can't possibly name all those who provided support and guidance along the way, but I hope I will have the chance to thank everyone individually and in person. What follows is a very incomplete (and possibly irreverent) list:

Meg Urry: That students probably thank their advisors for their patience and support all the time doesn't mean exceptional amounts of both weren't required in my case. You have been more generous to me than I had any right to expect, both within and beyond the student-advisor relationship. It's not just that you're great at so many things; you also freely share your knowledge in both formal and informal situations. Casual conversation over croque monsieurs often turns to important topics like politics, careers, or pure science. You have been an advisor, a mentor and a friend, and I truly hope I will justify your faith in me in the coming years.

Charles Bailyn: You have mentored me since the first day of graduate school. I value both the official and the unofficial advice: I still remember a time just before my qualifying exam when you corrected me after I expressed a lack of confidence. At the time I had never heard of Impostor Syndrome; I just knew someone I respected was telling me to quit thinking I wasn't good enough. For that and many other moments, thank you.

David Spergel, Neta Bahcall, Jim Gunn, and Suzanne Staggs: Without your patient guidance and support, I would never have gotten into graduate school in the first place. I can think of nobody better from whom to learn the fundamentals of science and research.

iii

Laura: If I'm not mistaken, you would be graduating from college right about now. We could have celebrated together. How I feel about you is very complicated, and I'm certainly not going to thank you for the choice you made, but I will acknowledge that you re-opened my eyes to the most important things in life. I wish I could see you in a cap and gown. I wish you could see this. I wish you knew how much we all loved you (and still do).

Tim: I'm supposed to be the wise older sister, but you've taught me so much about following one's passion. Even though ours are very different, we're still similar in so many ways. (It's like we're related or something.) When you come to the final push of your own dissertation, I will repeat to you the sage motivational advice you offered me: "It's game face time. . . stick that tongue out and go all Michael Jordan on this [thing]." It turns out self-motivational trash talk really works.

Mom and Dad: someday I may find a way to repay you for your endless support and love. I know you'd say that I don't have to, or that I already have. But that's exactly why I want to keep trying. Thank you.

Contents

List of Figures

List of Tables

Chapter 1

Introduction & Background

1.1   Galaxies and Active Galactic Nuclei

The means by which galaxies and their central supermassive black holes (SMBHs) grow and co-evolve is one of the fundamental questions in galaxy evolution. Galaxies appear to have formed hierarchically via mergers of smaller galaxies to form the complex universe we see today (White & Rees 1978; Kauffmann et al. 1993), but the evolutionary pathways by which galaxies and SMBHs evolve in tandem are not yet well understood.

The seeds of SMBHs are thought to have formed in the early universe, either via direct collapse of low-metallicity gas clouds (Lodato & Natarajan 2006, 2007; Volonteri et al. 2008) or as the compact remnants of the first stars (e.g., Madau & Rees 2001; Heger et al. 2003). Seed black holes had masses at least several orders of magnitude below the masses we observe in SMBHs today (e.g., Devecchi et al. 2012). Therefore, SMBHs grow via accretion of matter throughout the history of the universe.

1.1.1 The Growth Of Supermassive Black Holes

Because the matter in the accretion region around a SMBH is dissipative, it typically collapses to a disk (e.g., Shakura & Sunyaev 1973). Owing to the lack of spherical symmetry, varying the angle of the line of sight with respect to the system leads to very different observed states for the same phenomenon: an accreting SMBH (Antonucci 1993; Urry & Padovani 1995). In addition, the total amount of matter falling into black holes can vary (from system to system, and within the same system, given enough time) by orders of magnitude. Growing black holes can accrete for prolonged periods at any rate up to the limit where the radiation pressure balances the gravitational force. This is known as the Eddington limit:

$$L_{\mathrm{Edd}} = 1.3 \times 10^{38} \frac{M_{\mathrm{BH}}}{M_{\odot}}.$$

There is no theoretical lower limit on the accretion rate of a black hole: lower luminosity limits to observed samples of growing SMBHs are most likely purely due to flux limits and observational selection effects (Woo & Urry 2002; Aird et al. 2012).

As matter falls into the gravitational potential of a SMBH, it releases enormous amounts of energy, so much that the energy from this relatively tiny region can outshine its entire host galaxy. Some classes of accreting black holes are among the most luminous objects in the universe (Glikman et al. 2004, 2007), although in fact these tend to be the most rare of active galactic nuclei (AGN). The bright lighthouses of a population are often those discovered first (Schmidt 1963) even though they do not represent the typical example of the underlying population.

In this thesis, I use the term AGN to refer generally to any growing supermassive black hole, including very luminous quasars and lower- and moderate-luminosity SMBHs (sometimes referred to elsewhere as Seyferts). Supermassive black holes gen-

erally range from $10^5 - 10^{10} M_\odot$; bolometric luminosities of confirmed AGN range from low luminosities of $\sim 10^{40}$ erg s^{-1} to the most luminous objects radiating at $\sim 10^{46}$ erg s^{-1} and higher.

The luminosity function of AGN resembles a broken power law at a range of redshifts (e.g., Croom et al. 2004; Hasinger et al. 2005; Glikman et al. 2010), with lower-luminosity AGN being far more common than their high-luminosity cousins. The slopes of the luminosity function vary little (if at all) with redshift, but the knee of the luminosity function evolves to higher luminosities at higher redshifts (see Croom et al. 2004, for a discussion of this at redshifts relevant to this thesis). Figure 1.1 (from Hasinger et al. 2005) shows that moderate-luminosity AGN (with $10^{43} \leq L_{bol} \leq 10^{45}$ erg s^{-1}) collectively dominate AGN emissivity at $z < 4$, owing to their being relatively common and also relatively energetic.

I study these moderate-luminosity AGN in this thesis; they provide a means of studying one of the most common and energetically important mechanisms of black hole growth.

1.1.2 Supermassive Black Holes Co-Evolve With Their Host Galaxies

Figure 1.1 also shows the evolution of AGN activity with redshift: the overall energy output of AGN has been falling since $z \sim 1.5$, when it peaked after a steady rise in the early universe (Fan et al. 2001). Likewise, the total amount of star formation in galaxies peaks at $z \approx 1 - 3$, a result first reported by Lilly et al. (1996) and Madau et al. (1998). The growth of galaxies and black holes peak at roughly the same epoch, and have both been declining since.

This macroscopic evidence of co-evolution of black holes and galaxies is echoed
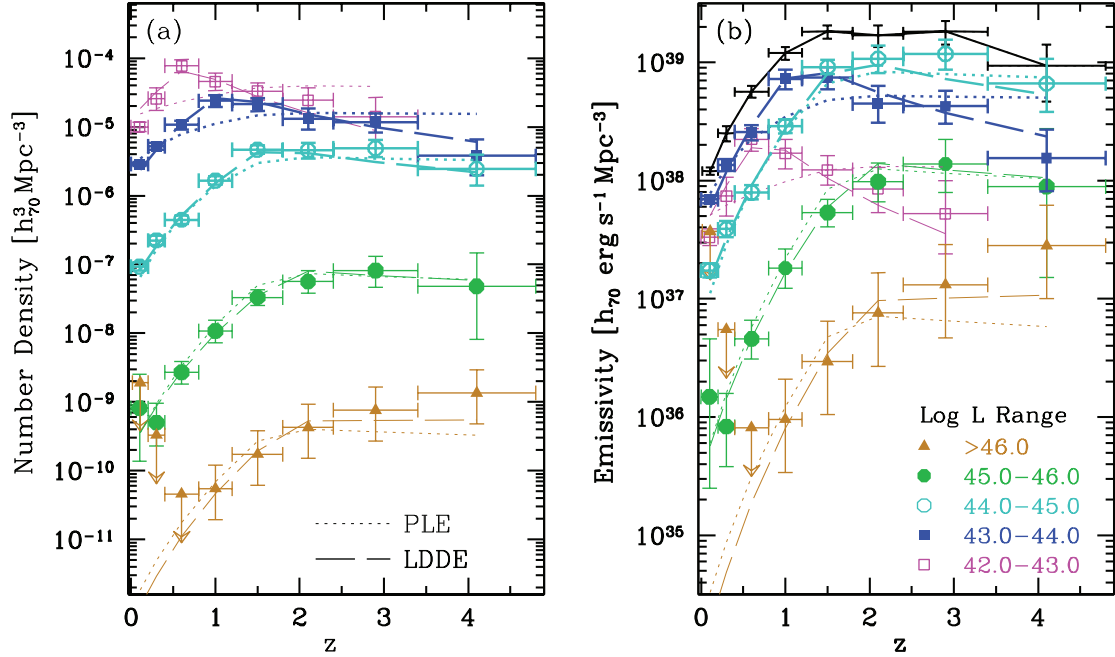
Fig. 1.1.— (From Hasinger et al. 2005) *Left:* AGN number density with redshift in several luminosity bins. *Right:* Total AGN emissivity with redshift in several different luminosity bins. Due to a combination of high numbers and moderate luminosity, AGN with $10^{43} \leq L_{bol} \leq 10^{45}$) erg s^{-1} collectively dominate AGN emissivity at $z < 4$.

by detailed observations of the black hole-galaxy connection, initially via observing the properties of black holes and bulges at local redshifts (e.g., Magorrian et al. 1998; Tremaine et al. 2002; Ferrarese & Ford 1999; Gebhardt et al. 2000; Marconi & Hunt 2003; Häring & Rix 2004). The work measuring black holes and galaxies has now been extended to more moderate redshifts (Treu et al. 2004; Woo et al. 2005; Peng et al. 2006; Bennert et al. 2010, 2011a). The strong evidence that galaxies and SMBHs evolve in tandem comes from a variety of analysis methods (see Figure 1.1.2 for an example from Gültekin et al. 2009 using bulge velocity dispersion, σ) and includes precise measurements of the SMBH at the center of the Milky Way (Genzel et al. 1997; Ghez et al. 2005). Nearly all galaxies we can observe, including our own, have the same galaxy-black hole relation, namely that the mass of the black hole is approximately 10^{-3} that of the mass of the galaxy/bulge (e.g., Merloni et al. 2010).

This may seem somewhat surprising given the vastly different scales involved. Star formation and growth across a galaxy involves scales of kiloparsecs or tens of kpc, while the accretion region around a SMBH is roughly a few light days across (or $\sim 10^{-3}$ pc, about the size of the orbit of Sedna). The small scale of the SMBH sphere of influence presents a physical challenge for its own growth: for a black hole to grow from a smaller seed mass to $10^{6-10} M_{\odot}$, it must capture a large amount of matter, but angular momentum conservation prevents large amounts of matter from migrating inward from the outer regions of a galaxy.

A proposed solution to this problem posits that mergers of galaxies – expected in most galaxies via normal hierarchical evolution – could disrupt the regular processes in a galaxy and channel large quantities of material inward, allowing rapid feeding of a SMBH and also affecting the evolution of a host galaxy, first triggering a burst of star formation in a ULIRG phase (Ultra-Luminous InfraRed Galaxy; e.g., Sanders et al. 1988; Kartaltepe 2009; Kartaltepe et al. 2011), after which the AGN accretion rate de-
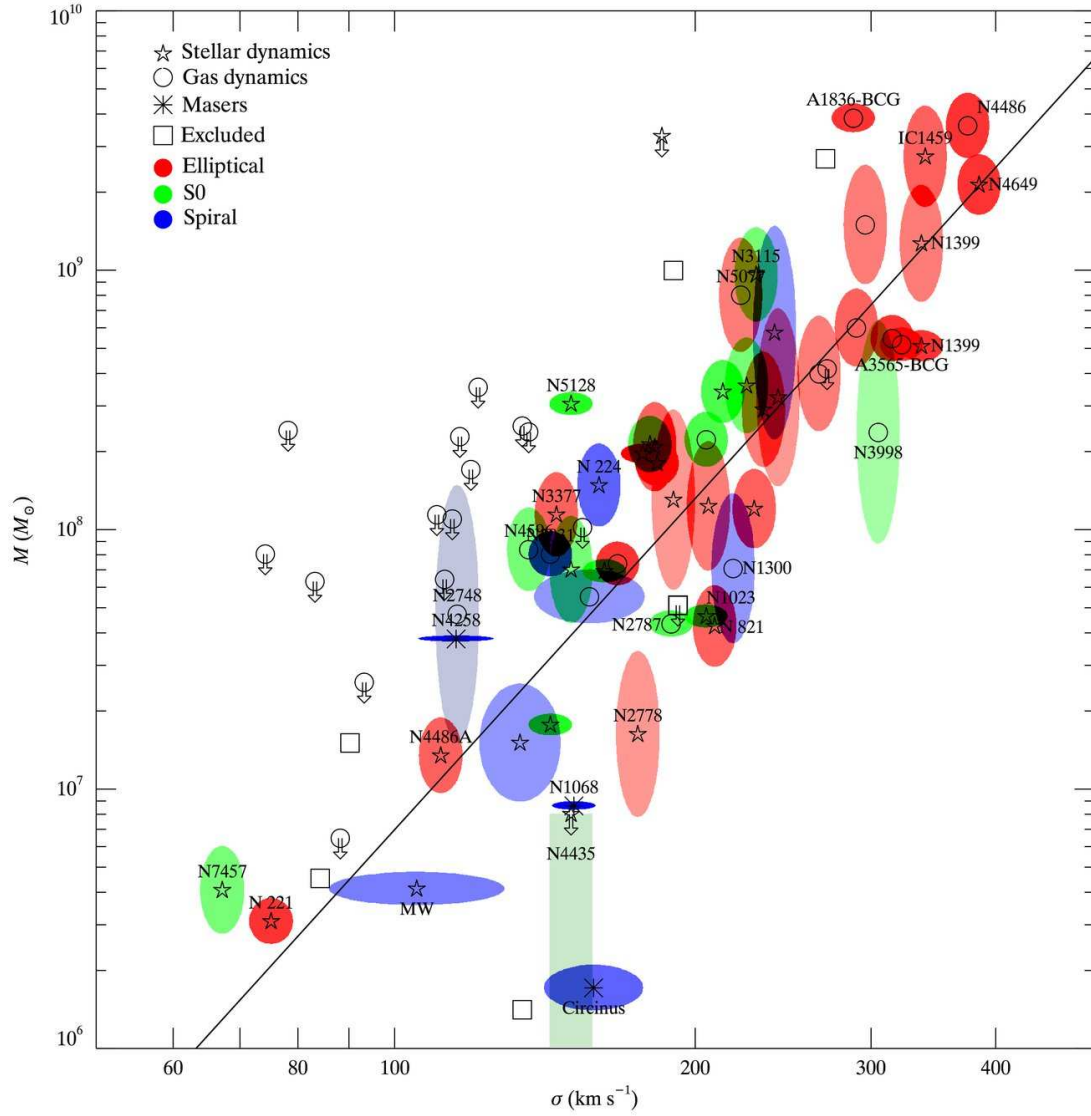
Fig. 1.2.— (From Gültekin et al. 2009) Black hole mass versus bulge velocity dispersion, measured several different ways. The $M - \sigma$ relation demonstrates that galaxies and black holes individually co-evolve together to follow the same relation between bulge velocity dispersion and black hole mass. Similar relations have been shown for bulge and galaxy mass (e.g., Marconi & Hunt 2003; Häring & Rix 2004).

cays predictably and the galaxy evolves to a massive, red elliptical with a correspondingly massive SMBH at its center (Kauffmann & Haehnelt 2000; Di Matteo et al. 2005; Croton et al. 2006; Hopkins et al. 2006a). Slightly more minor mergers may have less dramatic effects, but would still leave imprints on the host galaxy well after the signs of merger activity have faded (at which point the system might be observed as a moderate-luminosity AGN) via the formation of a galactic bulge (e.g., Toomre 1977; Walker et al. 1996; Hopkins et al. 2012; Martig et al. 2012).

1.1.3 Open Questions

While the merger-induced co-evolution hypothesis fits into the current overall picture of galaxy evolution via hierarchical merging, and even appears at least not *in*consistent with the most massive, luminous AGN (dust-reddened quasars; Glikman et al. 2004, 2007; Urrutia et al. 2008), the extent to which it can explain anything but the brightest, rarest of AGN remains an open question.

Broadly speaking, the first detailed studies of AGN and their host galaxies at a range of AGN luminosities tend to show a range of host galaxy morphologies, with elliptical and bulge-dominated morphologies more commonly hosting more luminous AGN (Bahcall et al. 1997; Malkan et al. 1998; Urry et al. 1999; McLure & Dunlop 2001, 2002). However, these studies took place prior to the advent of deep, multi-wavelength surveys and are difficult to compare due to their variety of sample sizes, depths, redshift limits, filters used, selection criteria, and morphological analysis methods. Additionally, these studies typically examined AGN and host galaxies at redshifts below the cosmic peak of AGN and star formation activity.

Later studies addressed some of these issues (e.g., Sánchez et al. 2004; Grogin et al. 2005), but although they hinted that more moderate-luminosity AGN lacked the same connection to ongoing mergers as the highest-luminosity quasars, placing quantitative

constraints on the merger history of the sample was more difficult due to several unanswered questions related to the way in which observed quantities in AGN host galaxies map to intrinsic quantities: *Can morphological analysis reliably separate host galaxy from AGN? How does the presence of a bright nuclear point source affect the recovery of host galaxy morphologies? How well does the observed galaxy light profile map to the intrinsic bulge-to-total ratio? Does the observed morphology of the same host galaxy change with redshift?*

A detailed analysis of the extent to which the merger co-evolution hypothesis is consistent with observed moderate-luminosity AGN and their host galaxies requires a large, uniform sample of AGN with high-resolution, rest-frame optical images and robust separation of AGN from host galaxy light. This allows for estimates of the growth rates of SMBHs in moderate-luminosity AGN and parallel analysis of the host galaxies to determine the rate of ongoing mergers and the extent to which the sample is consistent with being the bulge-dominated remnants of major mergers. Ideally such an analysis would extend to at least $z \sim 2$, where both the star formation and AGN activity in the universe are seen to peak. A suite of simulated AGN+host galaxies must underpin this analysis to determine the biases introduced in morphological analysis by the presence of a central AGN and quantify the limits of such analysis.

1.2 Studying AGN host galaxies at high redshift

As previously discussed, the accretion region of an AGN is so small that it is unresolved at even the best optical and near-infrared resolution for all but the nearest galaxies (e.g., our own). Depending on the amount of optical obscuration, the central point source of an AGN has the capacity to swamp the host galaxy light. This is less likely to happen for a moderate-luminosity AGN than for the brightest broad-line objects, but the pres-

ence (or possible presence) of a bright nucleus still presents significant obstacles to host galaxy analysis from ground-based data at all but the most local redshifts. Additionally, accurate separation of AGN from host galaxy light requires a well-characterized and ideally very stable PSF. The latter can make ground-based analysis of AGN hosts with adaptive optics difficult.

Therefore, space-based observations are ideal for studying host galaxies separately from AGN at redshifts where AGN activity peaks. The Advanced Camera for Surveys (ACS) and Wide Field Camera-3 (WFC3) instruments on the *Hubble Space Telescope* (*HST*) provide rest-frame optical coverage to $z \approx 2.7$. Because moderate-luminosity AGN are fairly common, it is possible to observe a statistically significant sample of moderate-luminosity AGN host galaxies on a small area of the sky, given enough depth. To learn as much as possible about the AGN+hosts, multi-wavelength observations beyond *HST* are required.

In particular, hard X-ray observations allow for a relatively unbiased sample of AGN, because the hard X-ray (energies above 2 keV) is far less sensitive to obscuration than optical wavelengths. Using the *Chandra* $2-8$ keV band selects all but the most obscured AGN, and is far less prone to contamination from star formation than infrared selection techniques, especially at higher redshifts. Near-infrared data, however, is useful for determination of host galaxy stellar masses and rest-frame $U - V$ colors. The best sample of AGN and host galaxies from $z \sim 1-3$ therefore requires a very deep survey with multi-band *HST* images, uniform hard X-ray coverage, and ground- and space-based observational follow-up.

1.2.1 GOODS: A Deep Multi-wavelength Legacy Survey

The Great Observatories Origins Deep Survey (GOODS; Giavalisco et al. 2004) is just such a project. GOODS covers 320 square arcminutes split into two fields, the *Chandra*

Deep Field-North (CDF-N) and the *Chandra* Deep Field-South (CDF-S). The observations include *HST*-ACS coverage in $BVIz$, providing rest-frame B observations at $z < 1.25$ with a 10σ point-source sensitivity of 27.8 mag in the ACS V (F606w) band; deep *Chandra* coverage in each field (Alexander et al. 2003); *Spitzer* IRAC and MIPS coverage from 3.6-24 μm; and ground-based follow-up in $UBVRIJHK$ from a multitude of telescopes and instruments (Giavalisco et al. 2004).

Recently, the Cosmic Assembly Near-infrared Deep Extragalactic Legacy Survey (CANDELS; Grogin et al. 2011) has observed the southern GOODS field with the new J and H bands on the *HST*-WFC3 instrument, enabling high-resolution rest-frame B analysis of AGN and their host galaxy morphologies to $z \approx 2.7$. Within the CDF-S, the identification of fainter AGN has also recently become possible with additional X-ray observations, bringing the total to 4 Ms of exposure for the CDF-S (Xue et al. 2011).

1.3 Galaxy Morphology

Morphology (the study of shapes) is at once a simple concept and a complex undertaking. A galaxy's morphology contains information about its past, present and future. The presence or absence of a structural feature indicates whether the mechanisms giving rise to that feature have been an important part of a galaxy's formation history, or are currently affecting the galaxy. For example, whether a galaxy has a dynamically hot stellar bulge component (and its relative strength compared to the cold, coherent disk) is an indicator of its merger history. If a significant merger is ongoing, that is typically immediately apparent upon visual inspection of an image. And an assessment of nearby neighbors of a galaxy can shed light on the number of mergers a galaxy will undergo in the future.

The study of galaxy morphology yields a unique kind of access to a galaxy's param-

eter space, and it has a long history. Galaxy classifications based on visual morphology have early roots (e.g., Hubble 1926) and are still quite useful today, especially when confirmed by many classifiers and quantified with modern techniques (as in the Galaxy Zoo project; Lintott et al. 2008).

Fully quantitative morphologies are a somewhat more modern invention and allow for a different kind of analysis. Many parametric morphologies collapse a galaxy into one dimension and reduce it to a single number, such as the Concentration or Asymmetry indices (Conselice 2003). These are certainly useful (Grogin et al. 2005; Schawinski et al. 2009; Hambleton et al. 2011), especially when examining very low surface brightness features, or for images that are near the noise limit, where summing along isophotes can extract additional information.

For deeper surveys, however, it can be more enlightening to retain the two-dimensional information when analyzing a galaxy's morphology. Parameterizing a 2-D image is possible in a myriad of ways and with a complexity limited only by computational power, but adding complexity to a model can quickly lead to a loss of meaning in the recovered information. It may be theoretically possible to perfectly model a galaxy using an infinite number of Fourier modes, but such a model would present a challenge for physical interpretation even if it were computationally approachable.

Two-dimensional parametric morphological analysis that models a galaxy with an axisymmetric profile strikes a balance between parameterization and simplicity: it uses as much of a galaxy image as possible and preserves asymmetric information in the residuals while characterizing a galaxy with parameters that have physical meaning, such as the half-light radius, surface brightness, and axis ratio.

1.3.1 The Sérsic profile

One such model is the Sérsic profile (Sérsic 1968), which models a galaxy's surface brightness profile with an exponent n (see Figure 1.3):

$$I \propto e^{-R^{\frac{1}{n}}}.$$

If $n = 1$, the Sérsic profile reduces to a standard exponential disk profile. If $n = 4$, the profile is equivalent to that of a deVaucouleur bulge. In practice, the distinction between disk and bulge is robust, although pure spheroidal bulges and elliptical galaxies can have Sérsic indices that range from $3 \lesssim n \lesssim 8$ (Graham 2001; Ravindranath et al. 2004). Although the value of n can theoretically vary between $0 < n < \infty$, galaxies with $n > 8$ are rare.

It is possible to model a galaxy with several simultaneous Sérsic profiles (using a fitting program such as GALFIT; Peng et al. 2002, 2010), allowing independent estimates of multiple galaxy components such as a bulge and a disk. Alternatively, galaxies that intrinsically have both a bulge and disk and are modeled with a single Sérsic profile typically recover an intermediate index of $1.5 \leq n \leq 3$, although prior to the work in this thesis the exact mapping between a single-Sérsic fit and the intrinsic bulge-to-total ratio was not known for AGN host galaxies. However, even before this work it was generally accepted that the difference between a Sérsic profile fit of $n = 1$ and one of $n = 4$ reflects major differences in a galaxy's dynamical structure (Binney & Tremaine 1987).

1.3.2 AGN Host Morphologies

The image of an AGN+host galaxy has an additional (potential) component: the central point source. This nuclear point source may vary in luminosity by band and by source,
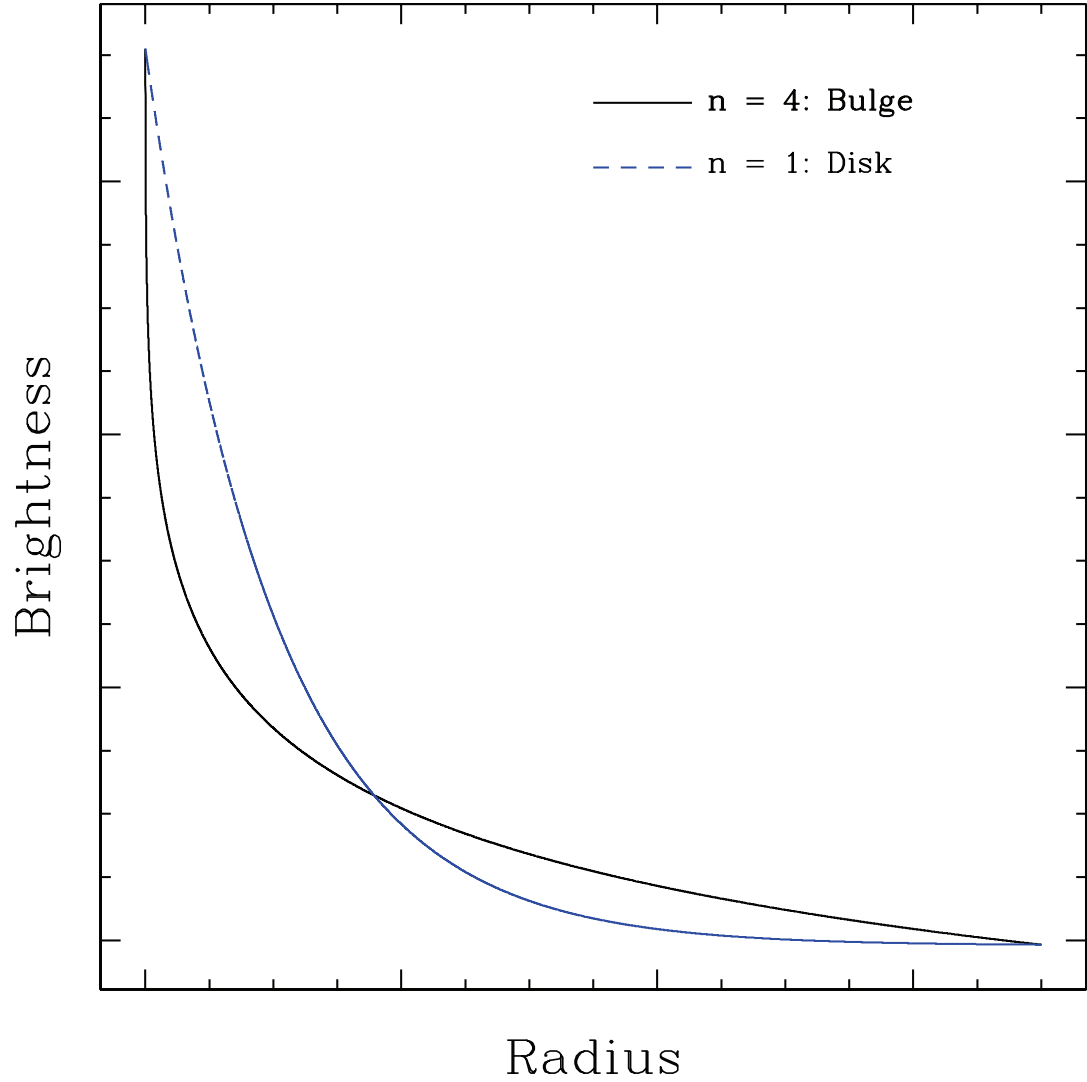
Fig. 1.3.— One-dimensional representations of two Sérsic profiles. The solid line shows $n = 4$, a deVaucouleur bulge. The dashed line shows $n = 1$, an exponential disk. When a two-dimensional profile is used, axis-ratio and position angle information is additionally modeled along with brightness, effective radius, and n.

and while it contains information about the central engine, it may also make the host galaxy morphology more difficult to detect. One of the primary limitations of the analysis of AGN host galaxies prior to this work was a lack of systematic understanding of how the presence of a central point source affects the recovery of the host galaxy morphologies.

1.4   Thesis Outline

Chapter 2 describes and analyzes a suite of extensive simulations, comprising $\approx 55,000$ simulated galaxy+AGN images with a variety of $L_{\mathrm{host}}/L_{\mathrm{AGN}}$ ratios and spanning a wide range of physically realistic host galaxy parameters, including pure bulges, pure disks, and composite galaxies spanning all possible bulge-to-total ratios. The simulations include galaxies at redshifts from $0.125 \leq z \leq 1.075$ whose intrinsic morphologies are known. From these simulations it is possible not only to characterize how well one can generally separate AGN from host galaxy, but whether recovered host morphologies change with redshift (even if the underlying population does not) and how well the Sérsic profile maps to the intrinsic bulge-to-total ratio of an AGN host galaxy.

Chapter 3 examines the growth of black holes in host galaxies at redshifts from $0.5 \leq z \leq 1.25$, covering the range at which the ACS filters on *HST* correspond to the rest-frame B band. Using known host-to-black hole correlations and accounting for possible redshift evolution of those correlations enables analysis of growth rates (Eddington ratios) of a large sample of moderate-luminosity AGN in host galaxies with a diverse morphological mix.

Chapter 4 extends this analysis to $1.25 \leq z \leq 2.67$ using the latest data from the WFC3 camera on *HST*. At these redshifts where star formation and the growth of black holes in the universe both peak, the fraction of the host galaxies of moderate-luminosity

AGN that are consistent with having a history of major mergers, or currently undergoing a merger, is a direct test of the merger co-evolution hypothesis as a primary driver of black hole-galaxy co-evolution.

Chapter 5 summarizes and synthesizes the results of Chapters 2-4 and suggests directions for future research.

Chapter 2

The Accuracy of Morphological

Decomposition of AGN Host Galaxies

Abstract

In order to assess the accuracy with which we can determine the morphologies of AGN host galaxies, we have simulated more than 50,000 ACS images of galaxies with $z < 1.25$, using image and noise properties appropriate for the GOODS survey. We test the effect of central point-source brightness on host galaxy parameter recovery with a set of simulated AGN host galaxies made by adding point sources to the centers of normal galaxies. We extend this analysis and also quantify the recovery of intrinsic morphological parameters of AGN host galaxies with a set of fully simulated inactive and AGN host galaxies.

We can reliably separate good from poor fit results using a combination of reasonable error cuts, in the regime where $(L_{\mathrm{host}}/L_{\mathrm{PS}}) > 1 : 4$. We give quantitative estimates of parameter errors as a function of host-to-point-source ratio. In general, we separate host

---

[1]This Chapter has been published as a paper in the Astrophysical Journal, Volume 683, pp. 644-658 (2008).

and point-source magnitudes reliably at all redshifts; point sources are well recovered more than 90% of the time, although spurious detection of central point sources can be as high as 25% for bulge-dominated sources. We find a general correlation between Sérsic index and intrinsic bulge-to-total ratio, such that a host galaxy with Sérsic $n < 1.5$ generally has at least 80% of its light from a disk component. Likewise, "bulge-dominated" galaxies with $n > 4$ typically derive at least 70% of their total host galaxy light from a bulge, but this number can be as low as 55%. Single-component Sérsic fits to an AGN host galaxy are statistically very reliable to $z < 1.25$ (for ACS survey data like ours). In contrast, two-component fits involving separate bulge and disk components tend to over-estimate the bulge fraction by $\sim 10\%$, with uncertainty of order 50%.

2.1   Introduction

Morphological analysis of two-dimensional light profiles of galaxies in large data surveys provides detailed information about galaxy populations and their evolution (*e.g.,* Simard et al. 1999; Ravindranath et al. 2004; Jogee et al. 2004; Sheth et al. 2008). Simulations of both large and small galaxy samples show that two-dimensional parametric and non-parametric morphological analysis of normal galaxies is extremely robust (Marleau & Simard 1998; Graham 2001; Conselice 2003; Trujillo & Aguerri 2004; Häussler et al. 2007).

Studies of AGN host galaxies give us the opportunity to study not just the galaxies themselves, but also the well-established connection between galaxies and central supermassive black holes (Kormendy & Richstone 1995; Magorrian et al. 1998; Ferrarese & Merritt 2000; Gebhardt et al. 2000; McLure & Dunlop 2002; Marconi & Hunt 2003). In cases where central black hole masses are independently determined, accurate decompositions of AGN host galaxies from their central point-source light contributions allow

for the direct study of how galaxy light distribution relates to black hole properties. Alternatively, when time-intensive observations of black hole mass are not available, we can use established bulge-black hole relations to determine the black hole masses from bulge luminosities.

However, two-dimensional morphological fitting of AGN host galaxies is more complicated than that of "normal" (or "inactive") galaxies because of the presence of a central point source, which is often quite bright. In order to extract host galaxy properties from a source comprised of a host plus a central AGN, spatial resolution is critical. Thus the Advanced Camera for Surveys (ACS) on the *Hubble Space Telescope* (*HST*) is the instrument of choice for many AGN host galaxy studies to date (Sánchez et al. 2004; Alonso-Herrero et al. 2008; Ballo et al. 2007).

Of the large multi-wavelength surveys currently available, the Great Observatories Origins Deep Survey (GOODS; Giavalisco et al. 2004) provides some of the deepest multicolor ACS data. AGN identification is possible because of deep X-ray imaging with Chandra, as well as ground-based optical and infrared spectroscopic follow up. Spitzer data provide additional information on total light but insufficient spatial resolution to separate the galaxy from the active nucleus. We performed detailed morphological analysis on the GOODS-ACS data set using GALFIT (Peng et al. 2002), the results of which were presented in Simmons et al. (2011) and Simmons et al. (2012, submitted). In order to understand the accuracy of those results – in particular, to probe the well-known effects of surface brightness dimming and dependence of physical resolution on redshift in the presence of a central point source whose size does not change with redshift – extensive simulations of host galaxy morphology are required.

Previously, Sánchez et al. (2004) simulated 1880 single-component host galaxies with point sources fainter than the host galaxy. Here we present a full treatment of over 50,000 simulated AGN host galaxies in the redshift range $0.1 < z < 1.1$, with

both single-component and two-component bulge-plus-disk morphologies, and central point sources that are both brighter and fainter than the host galaxy. Results of these simulations are intended to inform data analysis of AGN host morphologies, to better infer intrinsic host galaxy shapes from fitted morphological parameters in the presence of a central point source.

We discuss the data from which we draw our noise properties and simulated sample in Section 2.2. The detailed fit procedures and the simulation parameter space are presented in Section 2.3, and we assess the ability of our fitting procedure to recover accurate host galaxy and point-source parameters from GOODS-like images of AGN host galaxies in Section 2.4.

2.2 Data

2.2.1 *HST* ACS Data

The GOODS fields each cover an area of approximately $10' \times 16'$ with a total of 398 *HST* orbits in both fields. The Advanced Camera for Surveys has a resolution of $0''.05$ per pixel, and observations were taken in the F435W, F606W, F775W, and F850LP ACS bands, hereafter referred to as B, V, I, and z'. Data acquisition and reduction are detailed in Giavalisco et al. (2004) and Koekemoer et al. (2002). Each of the five epochs of data were processed via the basic ACS pipeline and a further processing task called multidrizzle, which finds an astrometric solution for all 5 epochs in order to correct for geometric distortion, and at the same time removes cosmic rays from the image (Koekemoer et al. 2002). The final images have resolution of $0''.03$ per pixel, and the magnitude limits for extended sources are $B < 28.4$ mag, $V < 28.4$ mag, $I < 27.7$ mag, and $z < 27.3$ mag.

From the reduced data, we randomly selected 450 inactive galaxies with stellarity class less than 0.8 (*i.e.,* objects which are not point sources) and magnitude $z' < 24.0$ mag for use in those of our simulations which include real data (§2.3.3). Since the majority of AGN host galaxies selected for morphological analysis in current surveys using *HST* have redshifts such that their I-band data lie in the rest-frame B band ($0.575 < z < 0.9$), we performed simulations using the I-band images and noise properties.

2.2.2 Noise Properties

For fully simulated galaxies (described in §2.3.4), noise appropriate to the GOODS-ACS fields was added. The task of simulating the noise in the GOODS-ACS fields is complicated by the dithering process, which correlates the noise among nearby pixels. We therefore use actual noise pixels (*i.e.*, source-free pixels) from the final GOODS-N and GOODS-S images rather than statistical models. We sampled 150 sub-sections of the GOODS images that contained no sources, 75 in the North field and 75 in the South, for a total of over 2.5 million noise pixels. Each of these sub-sections was cut into tiles of size 50×50 pixels; this resulted in 1042 tiles. These were then used to create 500 noise images of the same size as our data images by arranging random mosaics of the 50×50 noise tiles. We have verified that these new noise mosaics have the same overall noise properties (distribution of pixel intensities) as the original noise-only subsections of the GOODS images (Figure 2.1).

We also tested noise mosaics created from 10×10 tiles of background noise, but found the distribution of pixel intensities was shifted compared to the correlated noise properties of the dithered ACS images. We thus used only the 50×50 pixel noise images to create our final noise mosaics. The noise value distributions of the 50×50 and 10×10 noise mosaics are compared to the actual GOODS noise distribution in Figure 2.1.
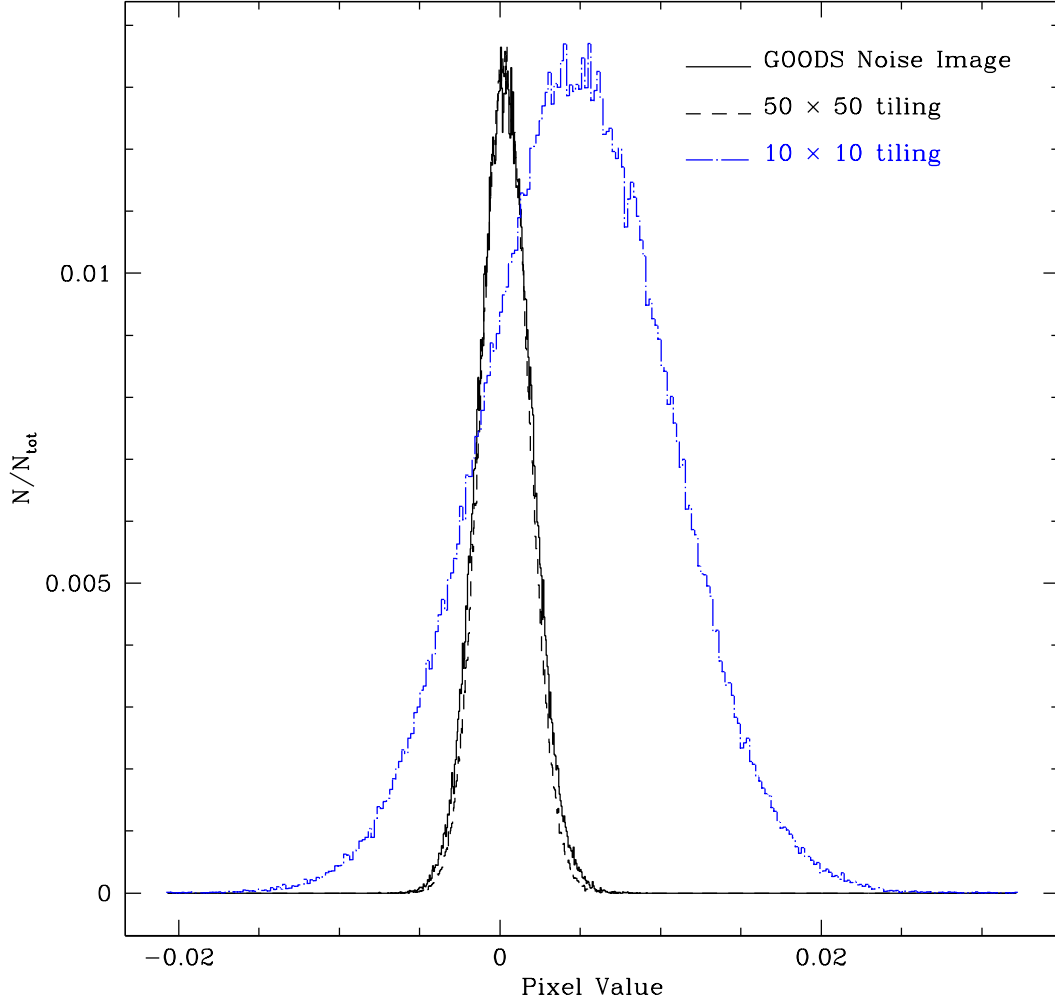
Fig. 2.1.— Histograms of pixel intensities for GOODS noise (solid), noise mosaics using a 50×50-pixel sampling of the GOODS noise (dashed), and using a 10×10-pixel sampling of the GOODS noise (blue, dot-dashed). The histogram for the mosaic using 10×10-pixel tiles is significantly different from the intrinsic noise distribution. The distribution of pixel intensity of the 50×50 noise mosaic is nearly indistinguishable from that of the intrinsic GOODS noise distribution.

2.3   Creation and Morphological Fitting of Simulated Samples

We performed two distinct sets of simulations to test the accuracy of derived morphological parameters. First, we used a sample of 450 real galaxies from the GOODS fields and added point sources to their centers. This allowed us to test the ability of GALFIT to extract point sources from the centers of real galaxies. It also informed our choice of parameters and galaxy types for the second, more extensive, set of simulations. In this latter set of simulations, we created a sample of 12,592 completely simulated GOODS galaxies, in order to additionally test the recovery of a wide range of host galaxy parameters. We fit all of our simulated galaxies with our batch-fitting algorithm (described below). We also simulated the redshifting of these galaxies to quantify redshift-dependent effects, and we added noise taken directly from real GOODS data.

2.3.1   Fit Procedure

We performed morphological analysis in two dimensions using GALFIT, which can simultaneously fit an arbitrary number of components to an image (Peng et al. 2002). The program uses a χ^2 minimization method to determine the best-fit parameters. We used the Sérsic profile, which models the light distribution of a galaxy as an exponential function with a variable half-light radius, r_e, and an exponential parameter, n, called the Sérsic index (Sérsic 1968). When n is fixed at a value of 1, the Sérsic profile is equivalent to an exponential disk; when $n = 4$, the Sérsic profile is equivalent to a deVaucouleur bulge. Each of our simulated galaxies was fit twice: once using a single Sérsic function with a variable index, and once with two Sérsics with fixed $n = 4$ and $n = 1$ (bulge + disk). We also simultaneously fitted point source (PS) components using the point spread function of the data, determination of which is based on GOODS field

stars and is described in Simmons et al. (2011).

We developed a batch-fitting algorithm to fit AGN host galaxies in GALFIT (described in detail in Simmons et al. 2011), which we use here on our simulated galaxies. The batch-fitting algorithm uses a series of initial guesses to execute a first-pass fit of the central region of each AGN host galaxy, fitting the individual centroid positions of each component (Sérsic plus point source, or deVaucouleur bulge plus exponential disk plus point source). The second fit iteration zooms out to include the full extended galaxy, and fits the central point source magnitude and AGN host galaxy parameters (Sérsic index or bulge/disk decomposition, half-light radius, axial ratio, etc.). Finally, a third iteration is performed where all parameters are allowed to vary (except n in cases of a bulge + disk fit).

It is important to note that, while these simulations include thousands of AGN host galaxies, even the largest (current) galaxy surveys using ACS data provide no more than hundreds of AGN host galaxies that can be reasonably fit with GALFIT. We can therefore follow up the batch fits by hand, using the results of the batch-mode fitting as initial guesses to further constrain the results for each AGN host galaxy. Due to the size of the simulated galaxy sample in this paper, we did not do this final hand-fitting step. Thus our conclusions about the fraction of cases for which accurate morphological parameters are recovered should be considered conservative when compared to a sample of galaxies whose fits are adjusted and verified individually.

2.3.2   Determination of Initial Parameter Guesses

For our real host galaxy sample, we use magnitude, flux radius, and position angle from the GOODS catalogs, which were created using SExtractor (Bertin & Arnouts 1996). Our simulated galaxies do not have a SExtractor catalog, but we simulated initial parameter guesses by introducing random errors into the true values.

Specifically, when determining initial guesses for parameters that can be measured from a data image, we assume the guess value is accurate to within the following: $\pm(2.0, 2.0)$ pixels in position, ± 0.5 in total magnitude, 10% in r_e and b/a, and 10 degrees in position angle. We assumed no *a priori* knowledge of the Sérsic index n of each simulated galaxy, nor of whether each simulated galaxy was a two-component bulge plus disk system, or a system with either a pure bulge or disk. Our initial guess for the Sérsic index (or indices) of each fit is $n = 2.5$.

In the case of a multi-component fit, we assume that the total magnitude is split evenly among the components (i.e., that we have no prior knowledge of Host:PS contrast ratio or bulge-to-total ratio), and we additionally assume that the measured position angle and axial ratio is the average of the actual values for each separate component after adding the random fluctuation to the sum.

2.3.3   Real Galaxies with Added Point Sources

In order to test whether we can recover central point sources from galaxies, we selected 450 I-band images of normal galaxies (*i.e.*, not X-ray detected) from the GOODS-North and GOODS-South fields. The selection was performed so the sample has the same the magnitude distribution as the full sample of galaxies in each of the GOODS fields, but was otherwise random. We assumed no knowledge of redshifts within the sample.

We fit each of these galaxies with a single Sérsic profile in order to determine the baseline set of morphological parameters for each galaxy. These fit parameters (Sérsic n, magnitude, half-light radius r_e, etc.) were taken to be the "actual" galaxy parameters.

We then made 9 copies of each galaxy, adding one point source to each, centered on the central pixel of the galaxy. The added point sources ranged in I-band magnitude from 21 to 29, in increments of 1 magnitude. This gave us a total of 4050 simulated AGN from the original 450 galaxies, with a large range of host galaxy to point source contrast

ratios, from ~1000:1 to 1:100. These provide a straightforward means of assessing the effect of a central point source on the recovered parameters of a real galaxy.

Our convergence rate for the fitting routine depends on the magnitude of the added central point source. Of the models with $I_{PS} = 21$, 88% converge, whereas 64% of models with $I_{ps} = 29$ (significantly below the flux limit of our I-band sample) converged. This is due to the fitting program being unable to converge to a value for the central point-source magnitude. Examples of fit results for typical galaxies in our sample are shown in Figure 2.2.

2.3.4   Simulated Galaxies

The simulated hosts described in §2.3.3 provide information on how the presence of a central point source changes the fitted host galaxy parameters, but they do not allow us to explore redshift effects or quantify the absolute accuracy of the fit parameters. This can only be accomplished with a set of simulations for which we know the intrinsic properties of each simulated galaxy.

To that end, we simulated three kinds of galaxies with a range of parameters: pure deVaucouleur bulge (B) galaxies with fixed Sérsic $n = 4$, pure exponential disk (D) galaxies with $n = 1$, and composite galaxies with both bulge and disk (B+D) components in varying proportions. The galaxy parameters were chosen to be typical of bright, local galaxies (Binney & Merrifield 1998) and placed at $z = 0.125$. Redshifted samples were developed from these, as described below.

For the B and D type galaxies, the component parameters occupy a grid of four values for each parameter across the ranges $16.9 \leq I_{AB} \leq 20.4$ and $1.5 \leq r_e \leq 6.0$ kpc (for bulges); $4.0 \leq r_e \leq 10.0$ kpc (for disks), with axis ratios $0.25 \leq b/a \leq 1.0$. For the single-component fits, the position angle was fixed at 45.0 degrees. This results in 64 B and 64 D galaxies, each of which is "inactive", *i.e.*, without a central point
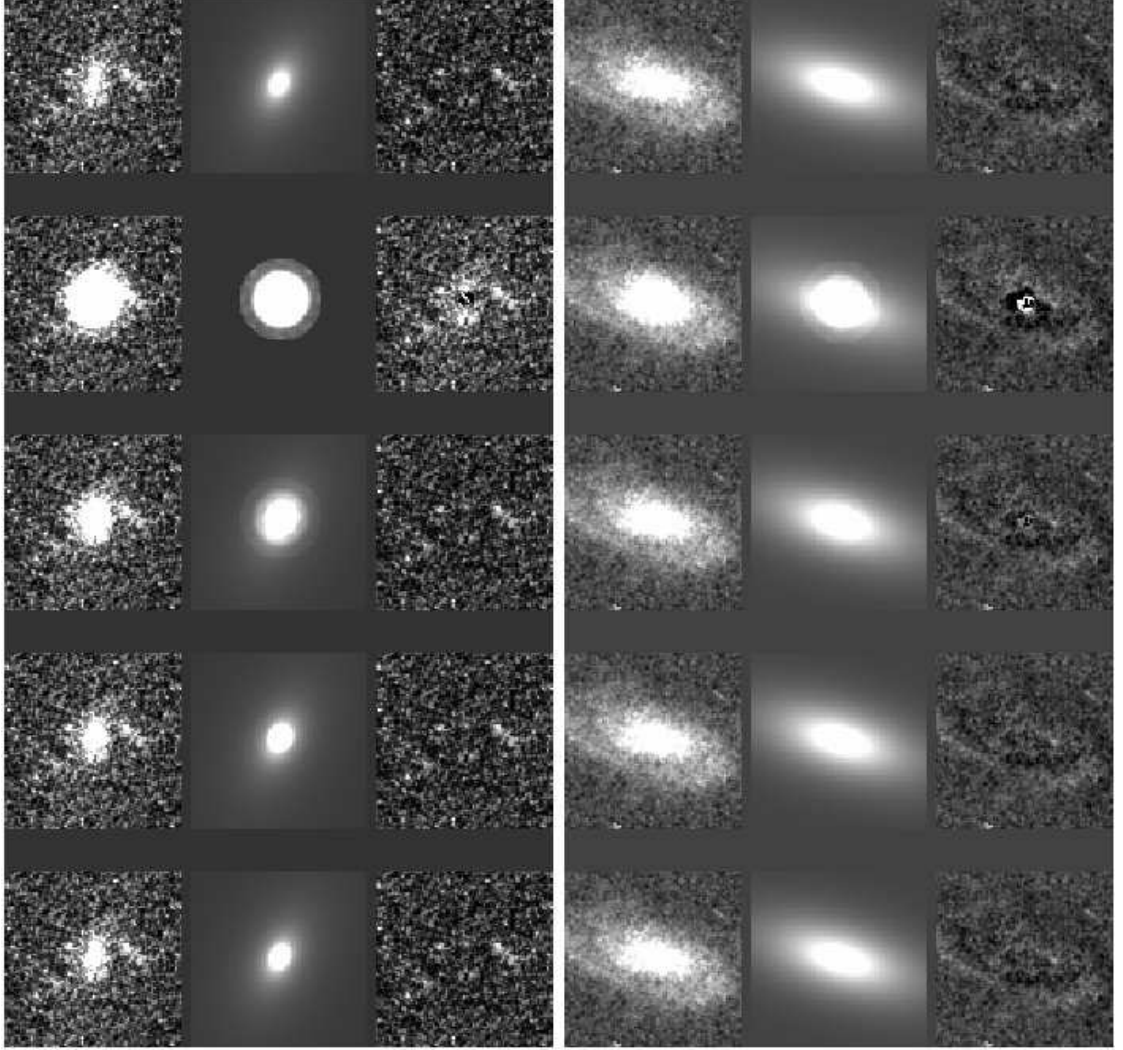
Fig. 2.2.— Example fit results for two AGN hosts simulated from real galaxies. For each galaxy, the top row shows the original GOODS galaxy (from left to right: galaxy, fit, residual). Each row below shows the host+fit+residual for added central point sources of magnitudes $I_{AB} = 22$, 24, 26, and 28, with the faintest point source in the bottom row. *Note:* These cutouts are zoomed-in to show the galaxies; the actual fitting regions are significantly larger.

source. We create simulated AGN host galaxies by adding point sources to these. We used five values between $16.5 \leq I_{AB} \leq 24$ for the central point source, resulting in 320 B-type and 320 D-type AGN host galaxies, with contrast ratios ranging from $-1.3 \leq \log\left(L_{\text{host}}/L_{\text{PS}}\right) \leq 2.8$. Lastly, in order to ensure enough galaxies for statistical analysis after binning the fitted single-component sample, we made four copies of each B and D inactive galaxy and two copies of each B and D AGN host galaxy. This resulted in a total of 256 B and 256 D inactive single-component galaxies, and 640 B and 640 D AGN host galaxies.

For the B+D type galaxies, the parameter space includes more magnitudes so as to provide 20 input bulge-to-total ratios with $0.028 \leq (\text{B/Tot}) \leq 0.97$ (plus the single-component B and D fits, which have $(\text{B/Tot}) = 1$ and 0, respectively). Additionally, the position angles of the individual components were allowed to vary such that some of the simulated B+D galaxies have components that are slightly ($\leq 15°$) off-axis with respect to each other. The axis ratios between bulges and disks were also allowed to vary with respect to each other. These changes significantly increase the total number of double-component galaxies created; thus the number of radius, b/a, and point-source magnitude parameters used was decreased in order to keep the total number of galaxies from being prohibitively large from a computational perspective. This resulted in the creation of 2700 inactive double-component (B+D) galaxies, and 8100 B+D AGN host galaxies. Table 2.1 gives the parameter values used to create the entire local suite of 12,592 simulated single- and double-component galaxies.

Since we are also interested in distinguishing the effects of redshifting galaxies from the effects of evolving galaxies, the initial sample was defined to lie at $z = 0.125$, and three additional samples were placed at $z = 0.413, 0.738$, and 1.075, corresponding to the redshifts at which the centers of each of our GOODS filters (F435W, F606W, F775W, and F850LP) are in the rest-frame B (F435W) band.

To redshift each galaxy, we used a concordance cosmology with $\Omega_{tot} = 1$, $\Omega_{\Lambda} = 0.73$, and $H_0 = 71$ km/s/Mpc (Spergel et al. 2003) to calculate the cosmological dimming and loss of resolution corresponding to each redshift. Because the size of the ACS PSF does not change with redshift, we assume that the size of AGN central point sources will also stay fixed with redshift, unlike the host galaxy. We therefore created the redshifted AGN by redshifting the model host galaxy (in flux and size) separately from the central point source (in flux only) and adding them together before convolving with the ACS PSF and adding noise to the image. The redshifting of each of the 12,592 galaxies produced another 12,592 galaxies at each final redshift, for a total of 50,368 fully simulated galaxies located at four different redshifts from $0.125 < z < 1.075$.

We fit each using our batch-fitting algorithm. Each galaxy was fit twice: once with a generalized Sérsic profile plus a point-source component, and once with a combination of deVaucouleur bulge, exponential disk, and point source. Inactive galaxies were also fit without point-source components. Examples of fit results for typical galaxies in our sample are shown in Figure 2.3.

2.4   Results And Discussion

2.4.1   Existing Galaxies with Added Point Sources

We are interested mainly in three properties of these models: how well they recover the input point-source magnitude, how well they recover the baseline host galaxy parameters, and how the accuracy of the host galaxy parameters relates to the point-source magnitude and/or the contrast ratio between central point source and host galaxy.
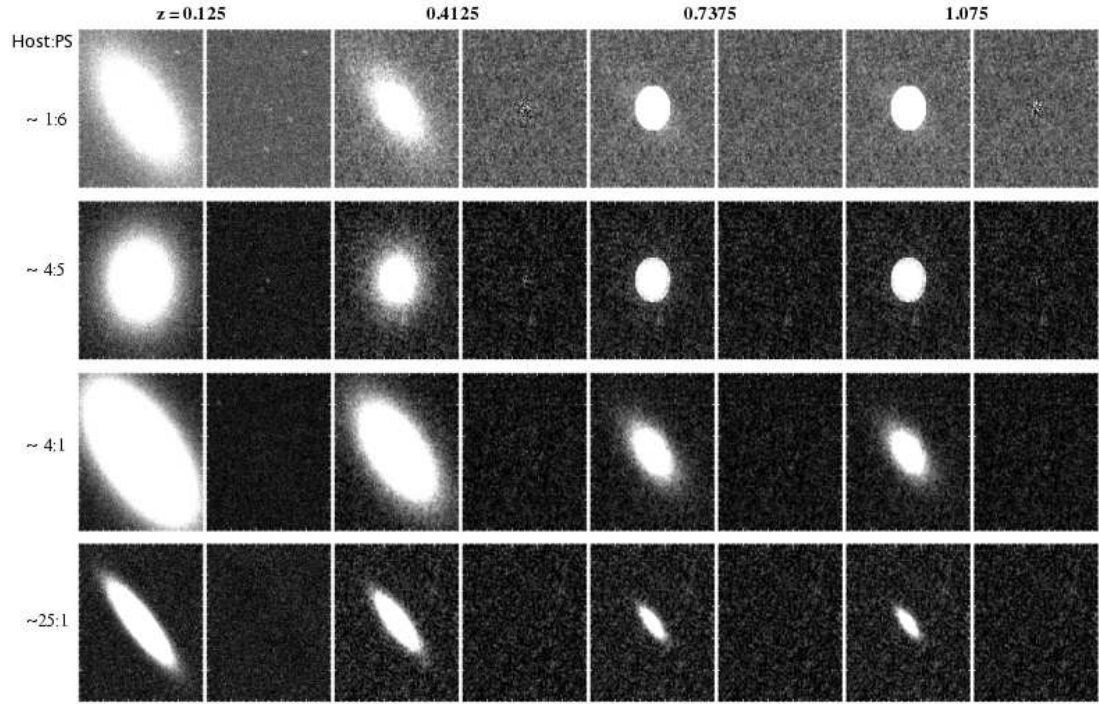
Fig. 2.3.— Example fit results for four fully simulated galaxies at four different redshifts. Each row shows one galaxy. The first two columns show the image of the galaxy at $z = 0.125$ and residual. Each successive pair of columns from left to right shows galaxy and residual for $z = 0.4125, 0.7375$, and 1.075, respectively. *Note:* These cutouts are zoomed-in to show the galaxies; the actual fitting regions are significantly larger.

AGN (Point Source) Recovery

Figure 2.4 shows the degree of recovery of the central point-source magnitude for input point sources. As expected, brighter point sources are more accurately recovered. At all values of input point-source magnitude, the fitted value of the point-source magnitude tends to either converge to the true input magnitude *or* remain at the input guess magnitude.

In all cases, we can easily separate these two groups with a simple reduced χ_ν^2 cut ($\chi_\nu^2 < 2.0$). After the cut, the number of remaining poor fits is very low, as is the number of good fits removed by the cut: both are less than 5 percent, even in the limiting cases of very high and very low input point-source magnitude. This level of contamination/excess removal of good fits is not strongly dependent on the value at which we choose to cut χ^2, nor is it strongly dependent on the input point-source magnitude.

The RMS uncertainties of the recovered point-source magnitudes for each input point-source value are shown in Table 2.2. These values reflect the systematic uncertainties in the fitted parameters, and should be added to the statistical error in fitted point-source magnitude returned by GALFIT.

Host Galaxy Parameter Recovery

Figure 2.5 shows the correlation between the fitted model's host galaxy magnitude and the actual host magnitude (as determined before the addition of the central point source). The percent completeness of the low-error sample compared to the full sample varies greatly across a range of contrast ratios between host galaxy and central point source. For very faint central point sources, the host galaxy magnitude is very well recovered, whereas for very bright point sources the fraction of host galaxies with well-recovered parameters is very low ($\sim 15\%$).
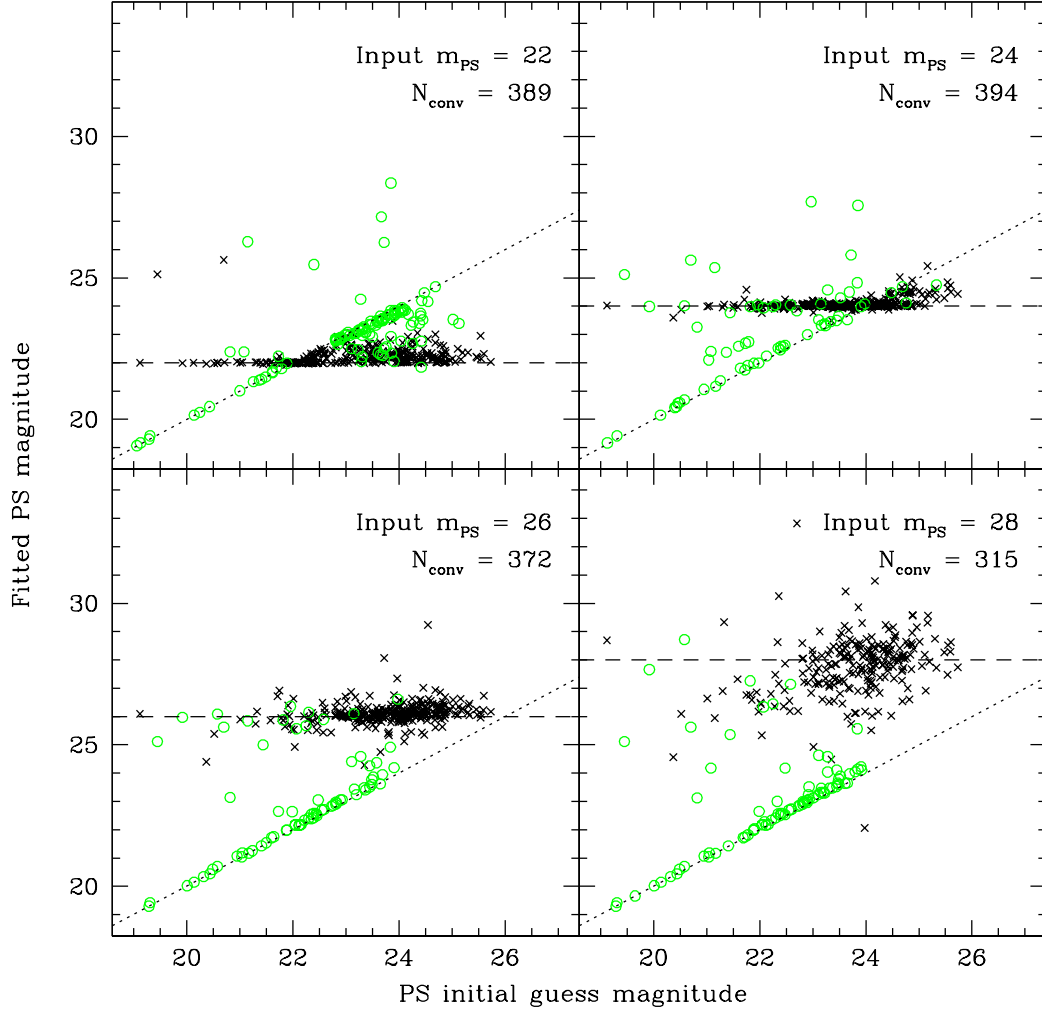
Fig. 2.4.— Recovery of magnitude of a point source added to real galaxy images, for: input point-source magnitudes of 22, 24, 26, and 28 mag. The fitting recovers the point-source magnitude nicely after making a simple $\chi^2_\nu < 2.0$ cut (black crosses), with a larger spread for fainter values of the input point source, as expected. Fits with a large value of χ^2_ν are shown as green open circles; N_{conv} indicates the number of fits (out of 450) that converged automatically for this input point-source magnitude. The dashed horizontal line shows $m_{out} = m_{in}$, so fits falling on this line perfectly recover the actual point-source magnitude. The dotted line shows $m_{out} = m_{guess}$: fits on this line converged to their initial guess point-source magnitude, and the final fitted magnitude is wrong; nearly all of these fits are removed by the χ^2_ν cut.
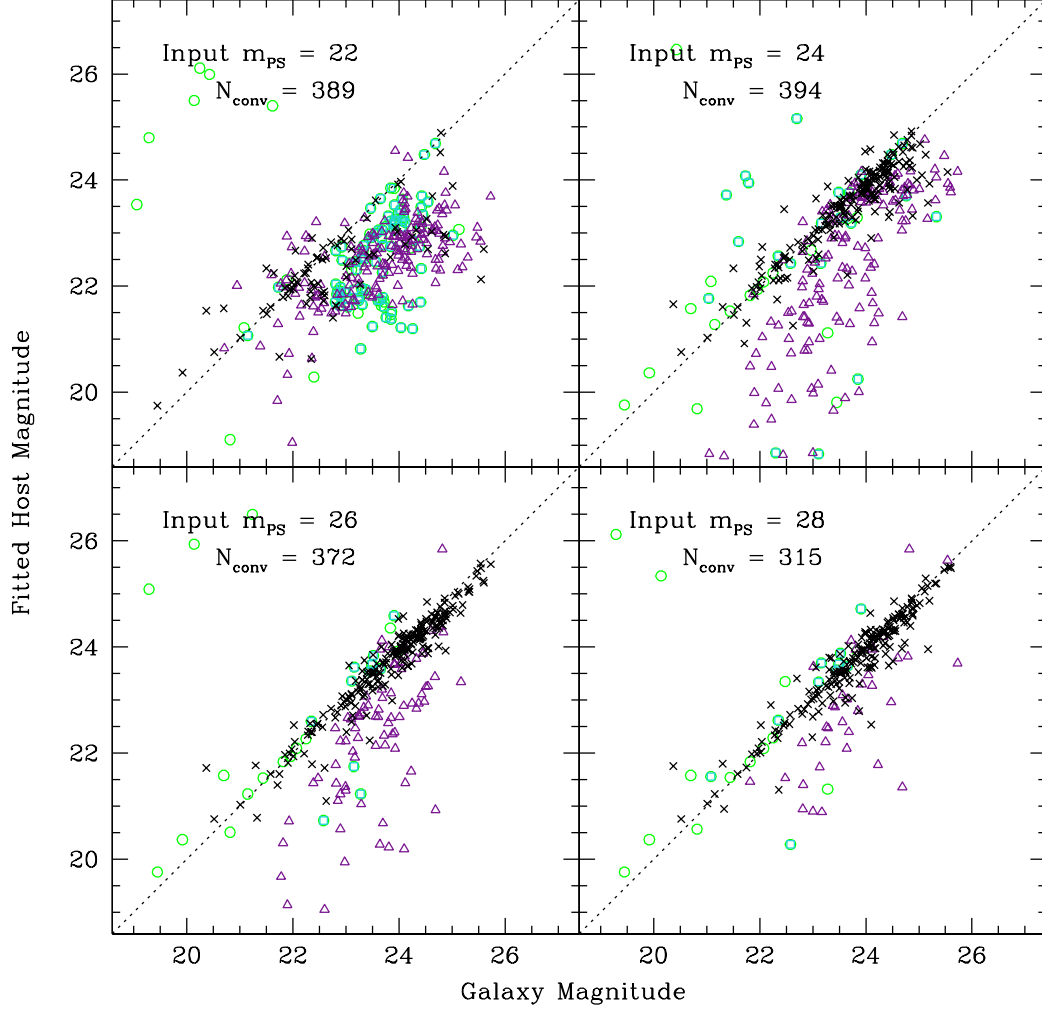
Fig. 2.5.— Fitted host galaxy magnitude versus actual galaxy magnitude for fits to actual galaxies with added point sources. Excluding high χ^2_ν values and effective radii with large fractional errors ensures a high fraction of good fits, with moderate uncertainties. Green open circles indicate fits with high χ^2_ν values. Cyan open squares indicate fits with excessive errors on the effective radius fit parameter ($\sigma_{r_e} \geq 0.8 \times r_e$). Purple open triangles represent fits with both high χ^2_ν and high σ_{r_e}. The dotted line represents equal input and recovered magnitudes (*i.e.*, perfect recovery). The error cut removes some of the fits that do lie on the 1:1 line, regardless of the precise value for the σ_{r_e} cut.

Our simulations show that the reduced χ^2_ν parameter is generally not sufficient to distinguish good from poor host galaxy fits. If we also limit the relative error of the effective radius parameter, however, the fraction of selected galaxies that recover the true magnitude of the host galaxy improves significantly. With the combination of χ^2_ν and σ_{r_e}/r_e parameters, we remove more than 85% of the fits with magnitude differences of 0.5 dex or more from the actual galaxy magnitudes. The number of well-fit galaxies that are also removed from the sample ranges from 5% to 20%, depending primarily on how conservatively we choose our relative σ_{r_e} cut. Figure 2.5 reflects a cutoff value of $(\sigma_{r_e}/r_e) = 0.8$, which removes 88% of poor fits and 12% of the good fits from the $I_{\mathbf{PS}} = 24$ sample.

Figure 2.6 shows how well we recover the Sérsic index, n. The same error cuts (χ^2_ν and σ_{r_e}/r_e) efficiently reject the inaccurate fits. The fraction of models whose fitted n values deviate by more than $\Delta n = 2$ compared to the n values of the unaltered galaxies increases significantly with increasing point-source flux. That is, a very bright central point source can easily be confused with a concentrated (high-n) Sérsic value. For all values of the added point-source magnitude, however, the same combination of χ^2_ν and relative r_e error is sufficient to remove 88% of the inaccurate fits from the data, while removing less than 15% of the well-fit models.

Dependence of Parameters on Host:AGN Contrast Ratio

Figure 2.7 shows the relation of fitted host galaxy parameters to the contrast ratio between the host galaxy and the added central point source, for the 1491 (of 4050) sources that are not eliminated by the combination of χ^2_ν and σ_{r_e}/r_e cuts. These include galaxies with all possible values of input point-source magnitude.

The left panel of Figure 2.7 shows the difference between the fitted host galaxy magnitude and original galaxy magnitude for the PS-added models. The recovered magni-
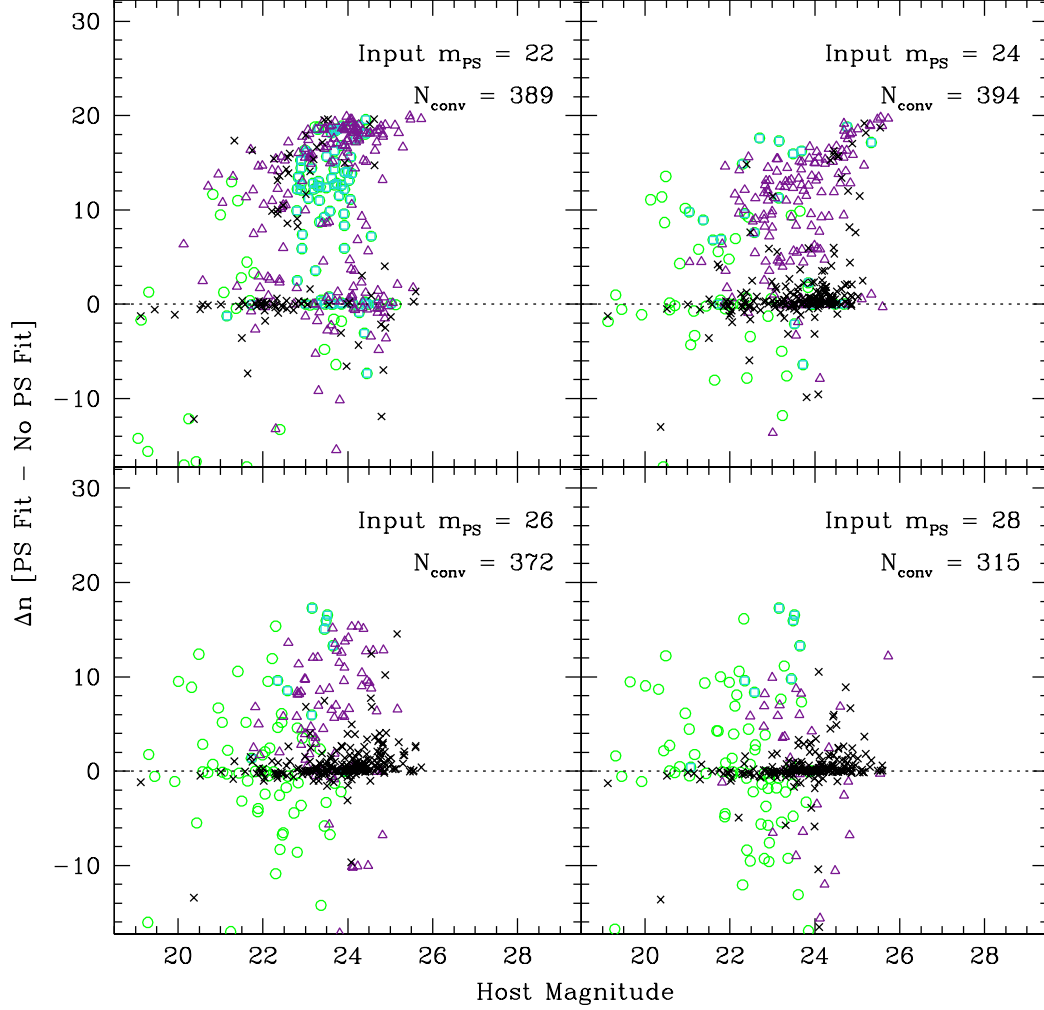
Fig. 2.6.— Change in Sérsic indices of host galaxies after adding point sources with original host magnitude. Excluding high χ^2_ν and σ_{r_e}/r_e yields the correct Sérsic index (a proxy for morphological type). The color-coding of the points is the same as in Figure 2.5: green open circles for high χ^2_ν, cyan open squares for high relative σ_{r_e}, and purple open triangles for both high χ^2_ν and relative σ_{r_e}. The dotted lines at $\Delta n = 0$ indicate perfect recovery of the Sérsic index. As expected, the bright-point-source fits return mostly unreliable host galaxy parameters, in contrast to the faint-point-source fits, which return mostly reliable host galaxy parameters.
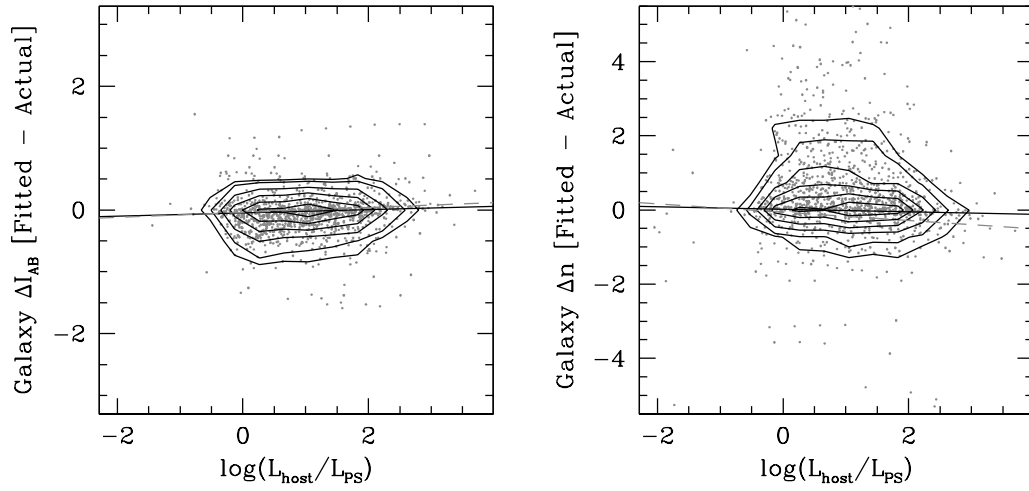
Fig. 2.7.— Accuracy of the host galaxy magnitude (left) and Sérsic index (right) as a function of the ratio of intrinsic galaxy luminosity to the added point-source luminosity. In both figures, contour plots are overlaid on the data points. Weighted least-squares fits to all data points (dashed lines) indicates that the recovery of galaxy magnitude and Sérsic index is very slightly correlated with host-to-PS contrast ratio. Excluding points with $\log(L_{\text{host}}/L_{\text{PS}}) < -0.6$, the weighted least-squares fit (solid lines) is consistent with zero slope (*i.e.*, no correlation between Host-to-PS contrast ratio) for both plots.

tudes are no different on average than the correct parameters. For galaxies with contrast ratios of at least $\log{(L_{\text{host}}/L_{\text{PS}})} < -0.6$, the host galaxy magnitude is well recovered, such that a weighted least-squares fit to those data with contrast ratios $(L_{\text{host}}/L_{\text{PS}})$ greater than 1:4 has a slope within 1% of zero, indicating no correlation between contrast ratio and recovered host galaxy magnitude. The scatter in the plot indicates that, while the sample as a whole is well-recovered, individual galaxies may have large differences in recovered parameters due to the presence of a point source. We see this result again in the right panel, which shows the difference between fitted and original Sérsic index as a function of host-to-PS contrast ratio. The inaccuracy in Sérsic index is larger when the added central point source is more than 4 times as bright as the host galaxy: the slope of the weighted least-squares fit is 6% for ΔI_{AB} and 11% for Δn. With proper error cuts, and for galaxies brighter than $1/4$ of the point-source magnitude, our host galaxy fits are not significantly contaminated by the central point source. However, the presence of a point source increases the uncertainty in fit parameters.

Figure 2.8 shows the median change in fitted parameters with input point-source magnitude. For very bright added point sources ($I_{AB} = 21$, $\langle\text{Host:PS}\rangle \approx 1 : 11$), all fit parameters deviate from their initially-determined values. The median Sérsic index is low by approximately $\Delta n = 1.75$, indicating that on average, galaxies with such bright point sources could be classified as disk-dominated even if they have more bulge-dominated intrinsic morphologies. The distribution is also very wide in the brightest-point-source bin: for such low host-to-PS contrast ratios, the Sérsic index is essentially completely uncertain. For fainter point-source magnitudes, recovery of the Sérsic index is far more reliable, although the uncertainty (indicated by the width of the distribution in each bin) is considerably larger than that reported by the fitting routine.

The ratio of host and point-source luminosities is also incorrect at the brightest point-source magnitudes: in these situations the typical fitted point-source magnitude is very

close to the input value, and the fitted host magnitude is too low (bright) by approximately 1.45 dex. Interestingly, the deviations in magnitude do not add to zero: because bright point-sources are also slightly too bright, the total magnitude is also underestimated (too bright) in the presence of a very bright central point source.

For point sources brighter than $I_{AB} = 24$, the distribution of recovered host galaxy magnitude is wide, such that the 68% confidence intervals span more than 1 dex in all bins. For those point sources with magnitudes fainter than 24 (which is approximately equal to the average magnitude of our initial galaxy sample), on the other hand, the model's host galaxy magnitude is well recovered.

Since the faintest point-source magnitudes ($I_{AB} = 28, 29$) are below the 10σ point-source detection limit of our band, the fitted point-source magnitude for these cases is often at least 1 magnitude brighter than the input point-source magnitude, with 68% confidence intervals larger than 1 magnitude.

The Sérsic indices for the host galaxies are within $\Delta n = 0.25$ on average for most values of the added point-source magnitude. Since disks are generally more extended than bulges, the Sérsic parameter is lower (on average) when the central point source is so bright that the central portion of the host galaxy is dwarfed by the light in the wings of the central point source. In all but the brightest cases, however, the median difference between the model Sérsic index and the no-point-source index is smaller than the size of the morphological bins discussed for a typical AGN sample (e.g., Sánchez et al. 2004; Ballo et al. 2007; Simmons et al. 2011), so it is unlikely that a significant fraction has been mis-classified as disk-like or bulge-like due to the presence of a central point source.

The RMS values of the recovered Sérsic indices and recovered host magnitudes for each input point-source magnitude are given in Table 2.2.
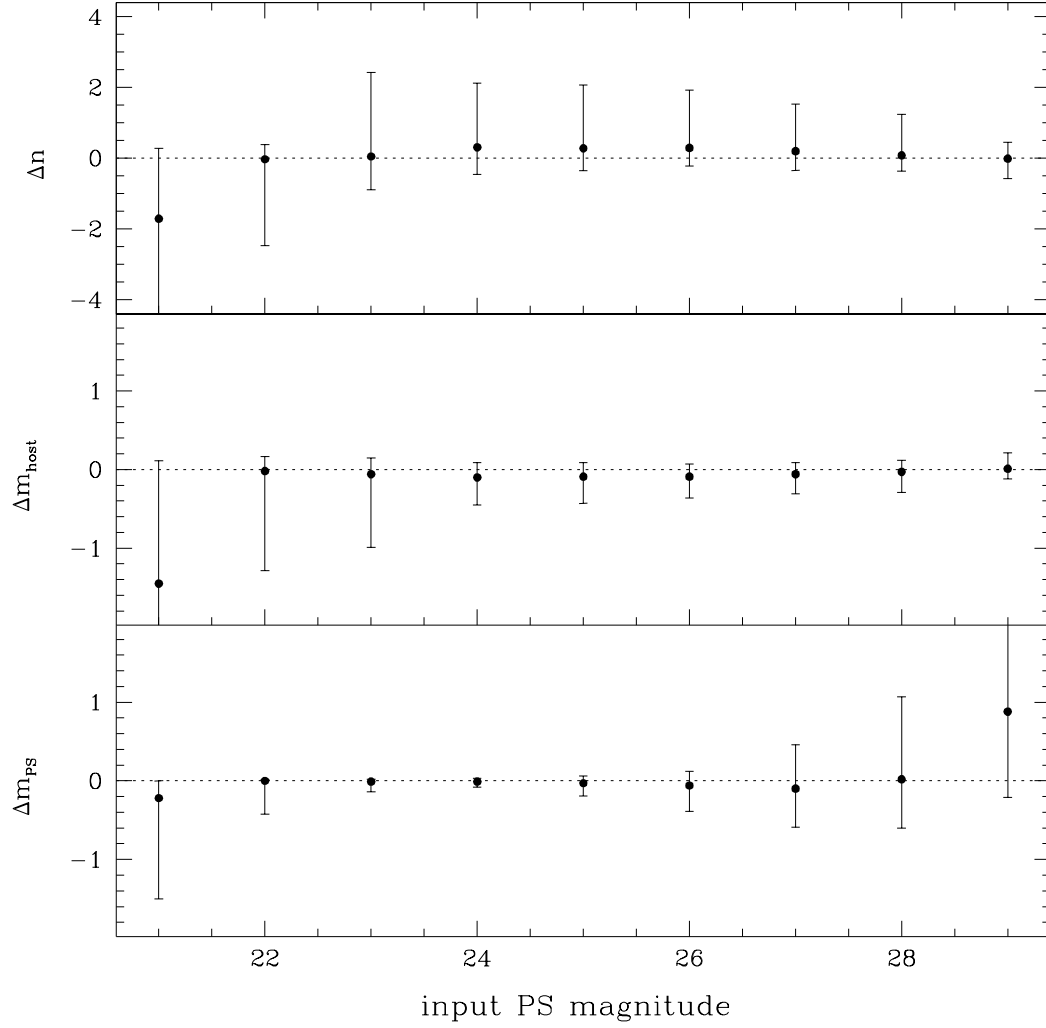
Fig. 2.8.— Median change in Sérsic index n (upper), host magnitude (middle), and point-source magnitude (lower) versus input point-source magnitude. Each point represents the median value of all the galaxies with the given input point-source magnitude whose fits pass the χ^2_ν and σ_{r_e}/r_e cut described in the text. The host Sérsic indices (top panel) are generally well-recovered for all but the brightest input point sources. The host magnitudes (middle panel) are also well-recovered in all but the brightest input point-source bin, with the error bars (representing the width of the distribution encompassing 68% of sources) increasing with increasing point-source strength. Point-source magnitudes (bottom panel) are recovered well until the input magnitude is fainter than the published 10σ point-source detection limit of the data.

2.4.2 Fully Simulated Galaxies

Input Parameter Recovery

For our 12,592 fully simulated GOODS galaxies, we apply the error cut determined above, using a combination of χ^2_ν and σ_{r_e}/r_e to distinguish good fits from poor fits. Within the single component galaxies, this error cut results in 706 of 896 B type galaxies with "good" fits and 708 of 896 D type galaxies with "good" fits.

The recovery of the Sérsic index for both of these types of galaxy models is shown for the $z = 0.125$ sample in Figure 2.9. If we classify galaxies as bulge-dominated when their fitted $n > 2.0$ and disk-dominated when their fitted $n < 2.0$, the level of misclassification based on these simulations is less than 15% for AGN host disk galaxies and less than 10% for AGN host bulge galaxies. Fewer than 10% of inactive disks are misclassified as bulges using the above cut; no inactive bulges are misclassified as disks. For any local sample of single-component galaxies (the simplest possible case), then, the Sérsic parameter is a very reliable indicator of morphological type.

The recovery of the $z = 0.125$ sample of two-component (B+D) galaxies is shown in Figure 2.10. The fitted bulge-to-total light ratio, $\text{B/Tot} = L_B / (L_B + L_D)$, is within $|\Delta(\text{B/Tot})| \leq 0.15$ for 50% of our AGN host sample and 66% of our inactive sample. A Gaussian fit to the data in Figure 2.10 gives an estimate of uncertainty in the bulge-to-total parameter of $\sigma_{\text{B/Tot}} = 0.04$. However, the contamination from very deviant fits (i.e., the wings of the histogram in Figure 2.10) is large. Approximately 14% and 13% of host and inactive galaxies remaining in the sample after our error cut have $\Delta(\text{B/Tot}) < -0.15$, and 36% of host galaxies and 21% of inactive galaxies have $\Delta(\text{B/Tot}) > 0.15$.

Figure 2.11 shows the ratio of fitted-to-input bulge-to-total flux ratio as a function of the intrinsic contrast ratio between the host galaxy and the central point source. The median and 1σ error bars (defined here as the values encompassing 68% of the points
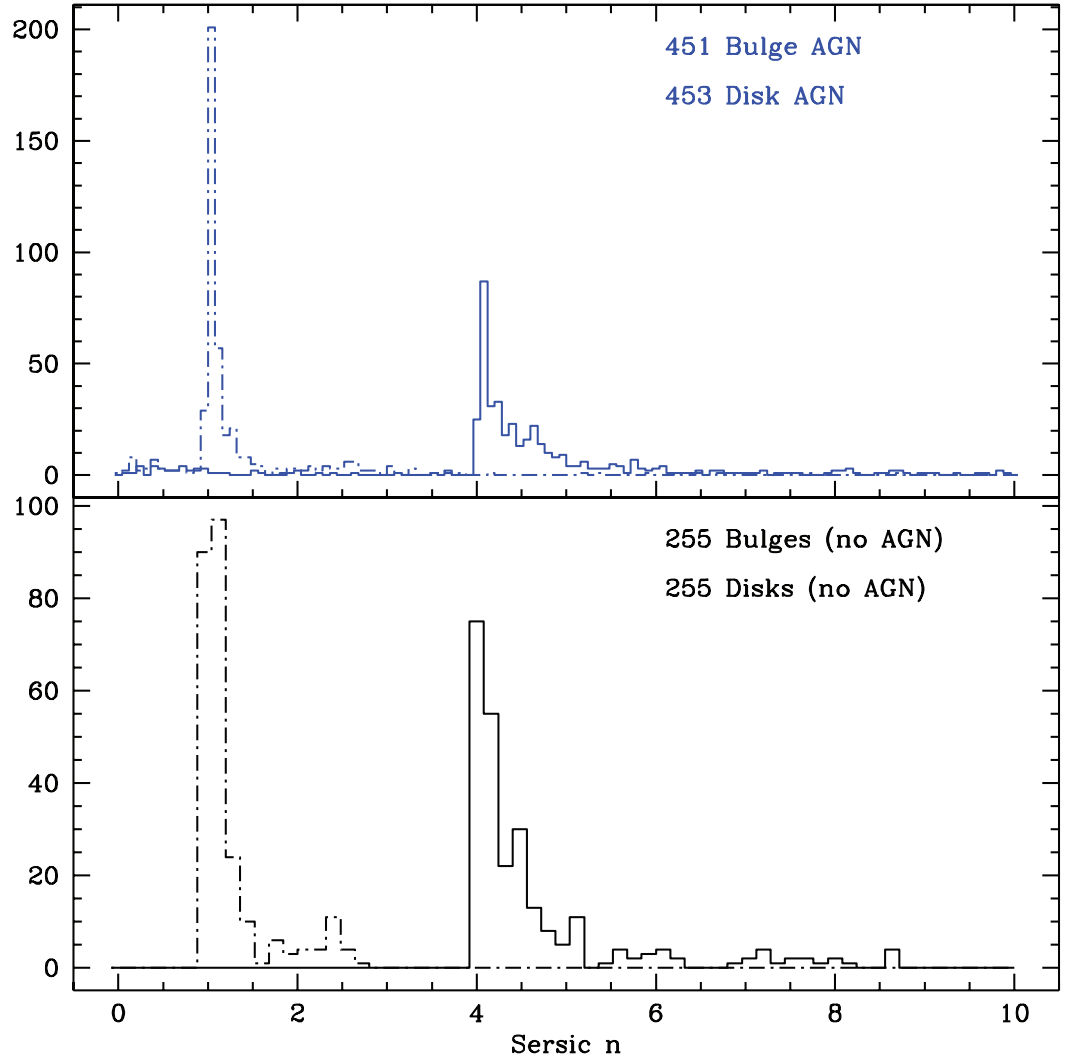
Fig. 2.9.— Recovery of Sérsic index n for the single-Sérsic fits to simulated single-component B and D AGN host galaxies (blue, top) and inactive galaxies (black, bottom). For the bulge-dominated B galaxies (solid histograms), the average fitted Sérsic index is slightly higher than the input $n = 4$ in both AGN and inactive galaxies; however, these are unambiguously classified as bulge-dominated galaxies, with fewer than 10% of bulge host galaxies mis-classified as disk-dominated galaxies and no bulge inactive galaxies mis-classified as disks. For the disk-dominated D galaxies (dot-dash histogram), the recovery of the input $n = 1$ is also excellent, with 13% of D host galaxies and 9% of D inactive galaxies having $n > 2.0$. The separation between the typical fitted n for B and D galaxies is robust and indicates that we can use the Sérsic index as a strong indicator of galaxy morphology for single-component local galaxies with and without central point sources.
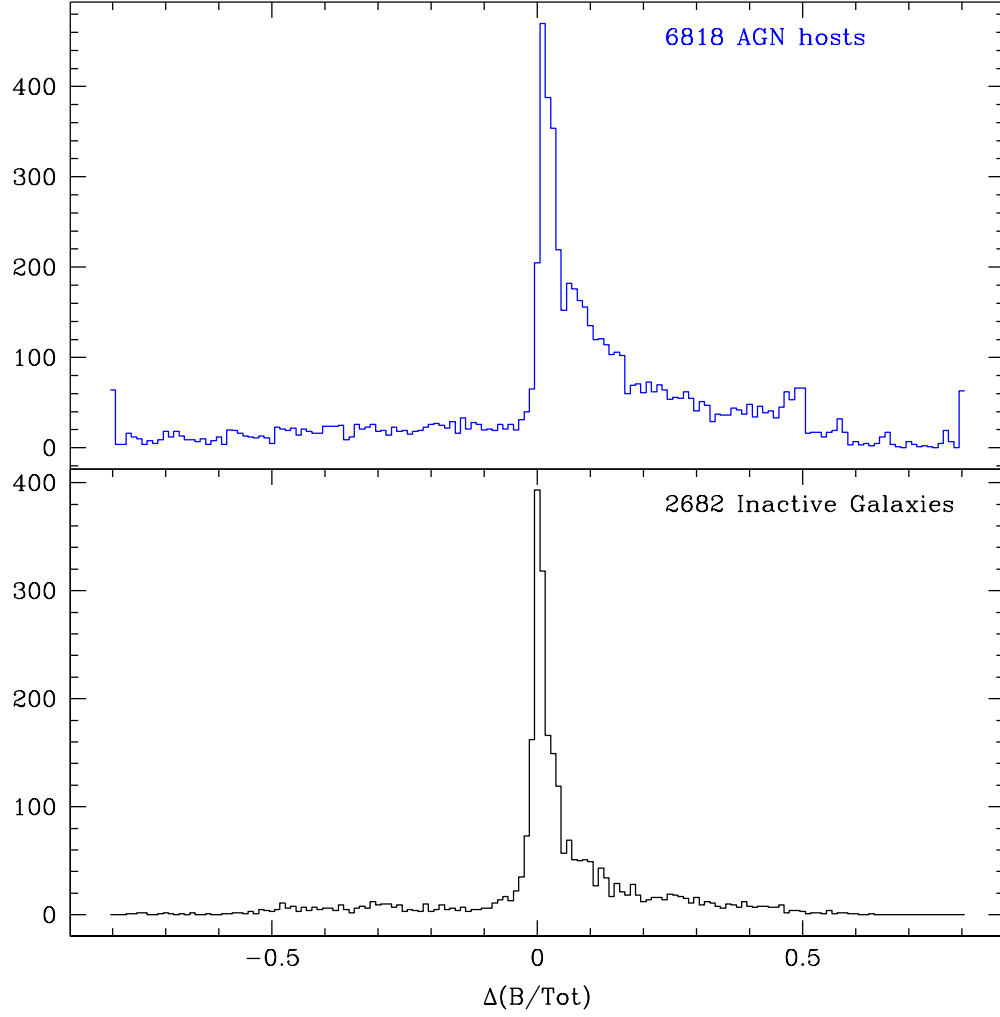
Fig. 2.10.— Recovery of input bulge-to-total ratio for the fully-simulated two-component galaxies. We define $\Delta\,(\mathrm{B/Tot}) > 0$ to mean the fit was more bulge-like than the input galaxy. A Gaussian fit to the Host galaxy distribution gives $\sigma_{BT} = 0.04$, but there is a large asymmetric tail on each distribution indicating that the samples are skewed toward more bulge-like fits than the intrinsic distribution. 36% of host galaxies and 21% of inactive galaxies have $\Delta\,(\mathrm{B/Tot}) > 0.15$.

in each bin) for the distribution of simulated galaxies without central point sources is plotted for comparison at a value of $L_{host}/L_{PS} = 3$. In general, the presence of a central point source skews the fits to slightly high values of the bulge-to-total ratio. For galaxies where the central point source is very bright, the spread is higher, such that a galaxy may fit to a bulge-to-total ratio twice the intrinsic value and still be within 1σ of the median value. Based on this, one could attempt to correct the bulge-to-total ratio for the presence of a central point source, but a bulge-to-total ratio fitted to a host galaxy could be overestimated by as much as 100%.

This large tail of high fitted bulge-to-total values has several causes. The radius of the bulge may converge to an unphysically high value; this causes the luminosity bulge-to-total ratio to skew high. This appears to be slightly more common when the intrinsic luminosity of the galaxy is disk-dominated, *i.e.*, with $(B/Tot) \leq 0.3$. Additionally, if the total source magnitude is not well-conserved during the fit, the bulge-to-total ratio typically deviates from the input value by at least 10% (high or low). This is more likely to occur when the bulge and disk components have approximately equal luminosity, or the bulge is slightly brighter $(0.45 \leq (B/Tot) \leq 0.7)$.

About 18% of the two-component AGN Host fits result in either a bulge or disk half-light radius which is unphysically low given the input sizes of both in our sample. These fits span the entire range of $\Delta (B/Tot)$ values, and are far more common when the central point source is intrinsically bright. For the locally-defined sample, 79% of B+D Bulge components and 63% of B+D Disk components with fitted $r_e < 5.0$ pixels are those with the brightest central point source; this comprises 26% of all two-component sources with the brightest central point source. It is worth noting that these fits typically show residuals which clearly indicate a poor fit, and they can therefore be removed from the well-fit sample upon visual inspection, or followed up with individual fitting to improve the fit.
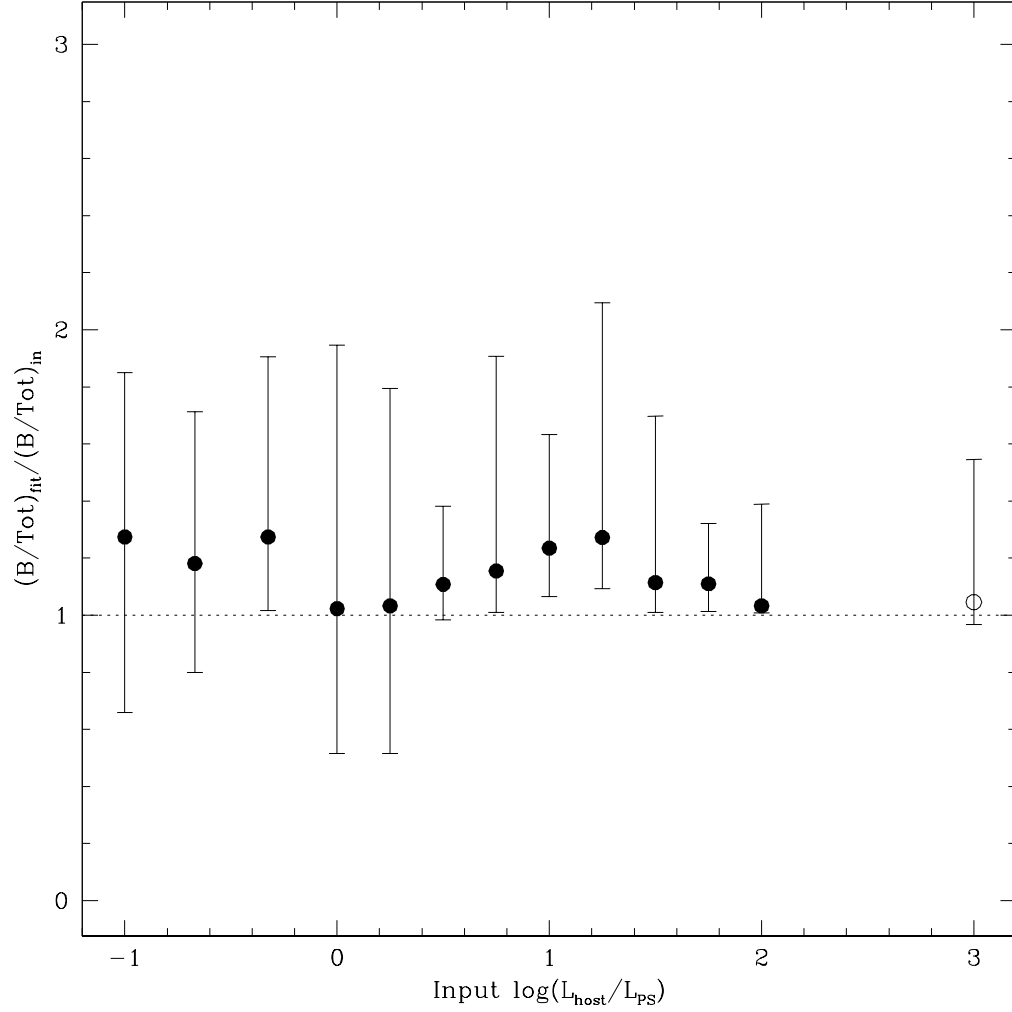
Fig. 2.11.— Ratio of fitted-to-input bulge-to-total vs. input host-to-PS contrast ratio. Points plotted are the median values in each bin, with error bars marking the range of values containing the central 68% of the points in each bin. The open circle shows simulated galaxies with no added point source; this bin recovers input bulge-to-total ratio closely, with a tail of high bulge-to-total values. For simulated host galaxies, the recovered bulge-to-total ratio is generally high by 10-20%, and the distribution of points in each bin is wider for galaxies where the central point source is at least as bright as the host galaxy.
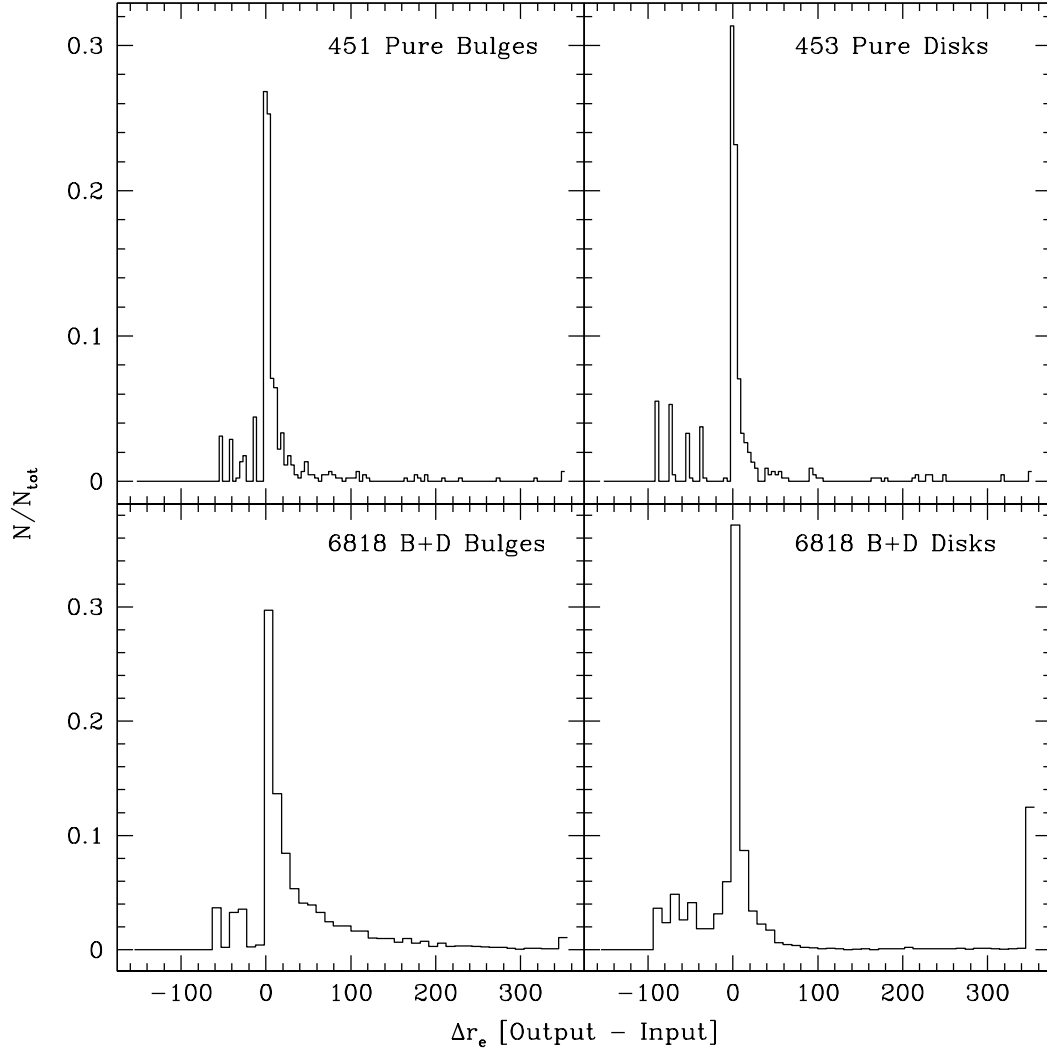
Fig. 2.12.— Histograms of the change in half-light radius for pure bulge (top left), pure disk (top right), B+D bulge (bottom left) and B+D disk (bottom right) fits to simulated AGN hosts. The majority of fits converge to a value that is equal to or greater than the input value of the half-light radius for that source or source component. The small discrete peaks at negative Δr_e values are comprised mostly of fits for which r_e converged to an unphysical value for our sample, $r_e < 5$ pixels. Single-Sérsic fits typically recover the sizes of pure bulges and pure disks with about the same level of success. However, the local sample of two-component galaxies indicates that bulge component radii are more likely to converge to a value that is at least 50 pixels too high, or at least twice the intrinsic radius. Local disk components are more likely to be underestimated, with a lower σ for the high-Δr_e distribution than for B+D bulges.

The recovery of bulge and disk sizes in our sample is shown in Figure 2.12. The distribution of Δr_e for single-component galaxies (pure bulges and disks) is sharply peaked at a value of $\Delta r \approx 0$ (in pixels). 66% of pure bulges and 65% of pure disks recover their input radii within $-1 \leq \Delta r_e \leq 12$ pixels. The discrete peaks at negative Δr_e represent those fits which converged to unphysically low values ($r_e < 5.0$ pixels for the local sample). Less than 5% of single-component fits converged to extremely large radii ($\Delta r_e > 150$ pixels).

The radius parameter converges to extremely high values far more frequently for the two-component fits, and with higher frequency for the bulge components of two-component galaxies (20%, B+D bulges) than for the disk components of two-component galaxies (13%, B+D disks). The high-Δr_e tail for B+D bulges is a result of confusion with the central point source of the simulated AGN host. Not only are bulges more compact than disks within our B+D galaxies (and typically within real galaxies as well), the slope of their light profile more closely resembles the light profile of the ACS PSF than does an exponential disk profile. This can lead to uncertain bulge radii and magnitudes, especially when the intrinsic luminosity of the bulge is similar to that of the central point source. Disk components of B+D galaxies are not as readily confused with the central point source: their fit typically fails when the surface brightness of the disk component is too low compared to the bulge and point source components.

Figure 2.13 demonstrates a possible method of separating good from poor two-component fits. After removing those fits where either the bulge or disk converged to $r_e < 5.0$ pixels, additionally requiring that the total source magnitude be conserved to within $|\Delta m_{tot}| < 0.5$ (determined by comparing the fitted total source magnitude with a measured, aperture-corrected magnitude), and/or that the flux-weighted effective radius of the fit be no more than 90 pixels larger than the measured half-light source
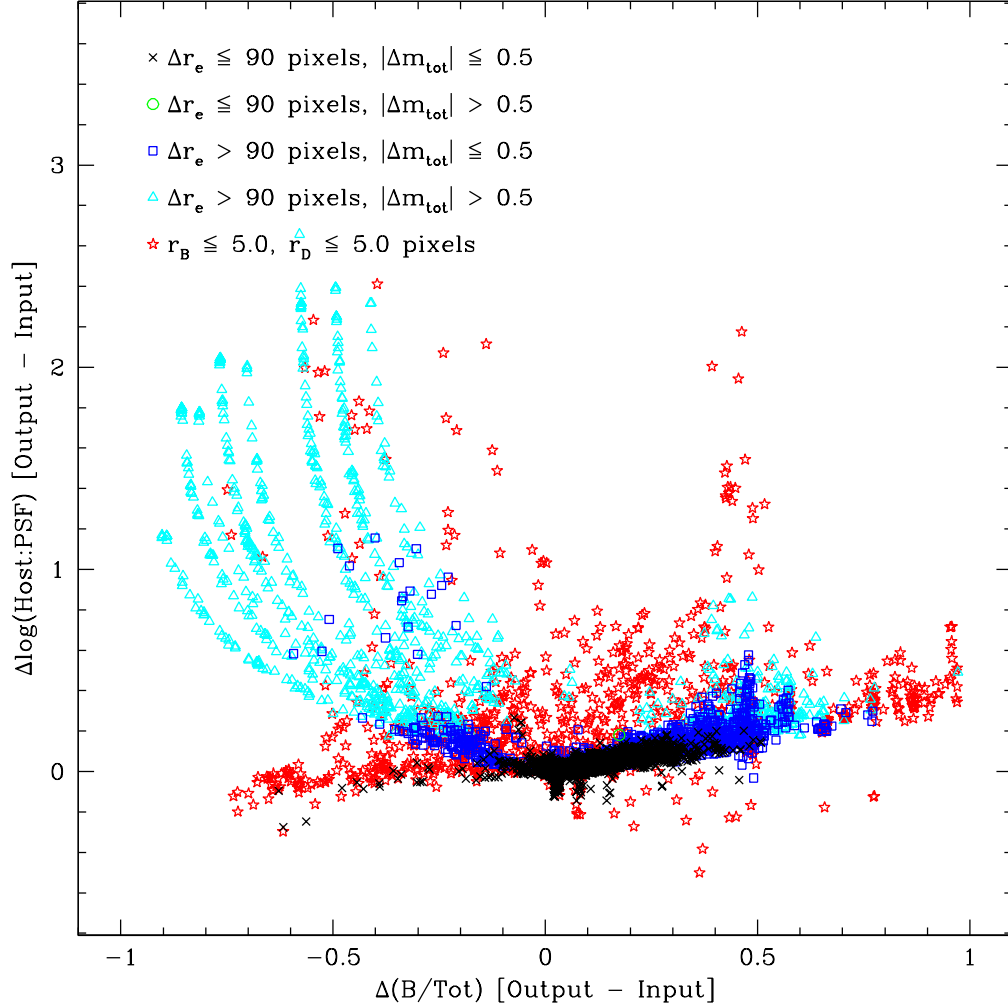
Fig. 2.13.— Deviation from input host-to-PS contrast ratio versus deviation in bulge-to-total ratio. Fits located at (0, 0) perfectly recovered the input bulge-to-total ratio and the Galaxy-AGN luminosity ratio ($L_{\mathrm{host}}/L_{\mathrm{PS}}$). Requiring that the difference between the half-light radii of the host be no more than 90 pixels larger than that observed for the entire source ($\Delta r_e \leq 90$), that the total source magnitude luminosity be conserved to better than $|\Delta m_{tot}| \leq 0.5$ mag, and that the radii of neither the bulge nor the disk component be less than 5 pixels (typically indicative of a poor fit) cuts 81% of sources with $|\Delta\,(\mathrm{B/Tot})| > 0.15$, and retains 83% of sources with $|\Delta\,(\mathrm{B/Tot})| \leq 0.15$.

radius[2] removes 81% of sources with $|\Delta\,(\mathrm{B/Tot})| > 0.15$ and retains 83% of sources within 0.15 of the input bulge-to-total ratio. This also constrains the fitted Host-to-PS contrast ratio to within 8% of the input value for 95% of the remaining "good" sample. However, this selection biases the remaining sample toward sources with faint central nuclei and preferentially retains bulge-dominated sources with intrinsic $(\mathrm{B/Tot}) > 0.7$. In general, the result of two-component fits should be used with caution, even for a local, well-understood sample.

Detection of Central Point Sources

We established in §2.4.1 that central point sources can be recovered on average for a sample of simulated host galaxies created from the addition of a central point source to a real GOODS inactive galaxy, though the fraction of recovered point sources varies depending on the luminosity of the added point source. Using the χ_ν^2 cut previously determined from this sample, we now examine the recovery of point sources with redshift and intrinsic morphological type. Figure 2.14 shows the fraction of fits in which the central point source was detected for our entire sample of fully simulated galaxies. In this case, our criteria for a "detected" point source is simple: the point source is considered undetected only if the magnitude parameter converged to a value considerably fainter than the detection limit of our simulated data ($m_{PS} = 27.1$ for our sample; Giavalisco et al. (2004)). Thus Figure 2.14 shows the fraction of fits for which any point-source magnitude was recovered, rather than those fits for which the magnitude is close to the intrinsic magnitude.

Figure 2.14 indicates that the point source is detected within the fit at least 90% of the time for all values of input $\log\,(L_{\mathrm{host}}/L_{\mathrm{PS}})$. The fraction is lowest when the point source and host galaxy have about equal luminosity. The detection fraction increases to

---

[2]This value was chosen because it is twice the observed radius of the largest source in our sample.

more than 95% at the highest values of input $\log{(L_\text{host}/L_\text{PS})}$, even for cases in which the point source is 100 times fainter than its host galaxy. This is due to the fact that the convergence fraction is lower for these bins; fits where the central point source may not have been detected are less likely to converge, driving the detection fraction higher for those fits which did converge.

While we are primarily interested in the recovery of host galaxy parameters and optical detection of central AGN, we also want to characterize the fraction of spurious optical point-source identifications. Thus Figure 2.15 shows the results of a Sérsic + PS fit to *inactive* galaxies with no intrinsic central point source. We find a significant difference in the number of false point-source detections between pure disk and pure bulge galaxies. Only $\sim 1\%$ of pure disk inactive galaxies detect[3] a central point source when none is present. However, we find a point source nearly one-quarter of the time when the simulated galaxy is a pure bulge. Because our total sample is composed of equal numbers of pure bulge and pure disk galaxies, this gives an overall false detection of a central point source in 12% of inactive galaxies. However, this effect is strongly dependent on morphology: fits to elliptical galaxies are far more likely to detect a faint point source when none is present than fits to disk galaxies. Host galaxy studies estimating the uncertainty in the fraction of hosts with detected optical point sources should therefore consider the morphological composition of their data sample: if the sample contains mostly elliptical galaxies, the number of false detections could be as high as 25%.

---

[3]We define "detected" as having been fit with a magnitude brighter than the published 10σ point-source detection limit of the GOODS survey (from which we take our noise properties).
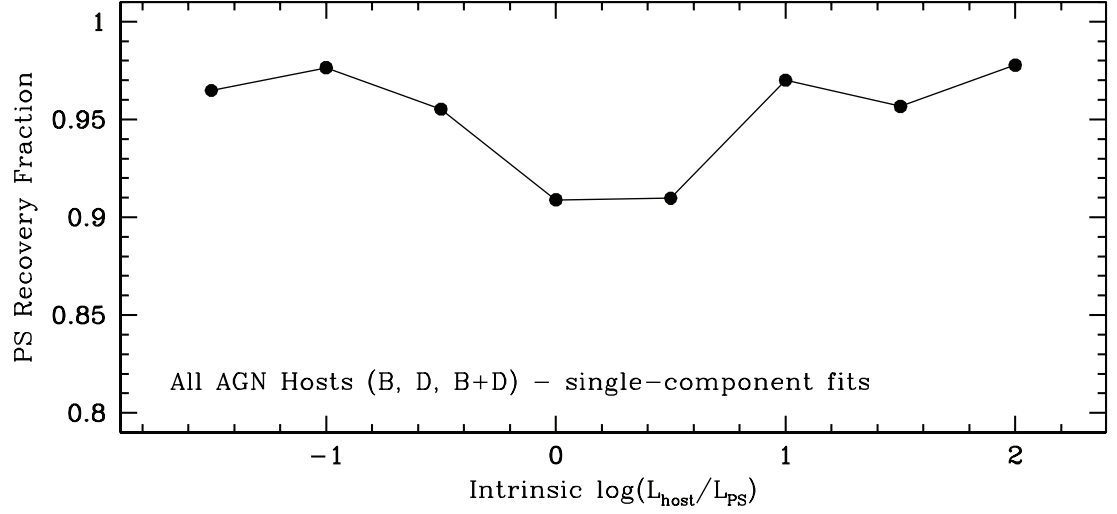
Fig. 2.14.— Fraction of point sources recovered for single-component fits to all simulated AGN host galaxies. The fraction of recovered point sources is slightly lower when the with input $\log\left(L_{\mathrm{host}}/L_{\mathrm{PS}}\right)$ is near zero ($L_{PS} \approx L_{host}$ or slightly fainter). However, even in these cases, the fits detect at least 90% of point sources.
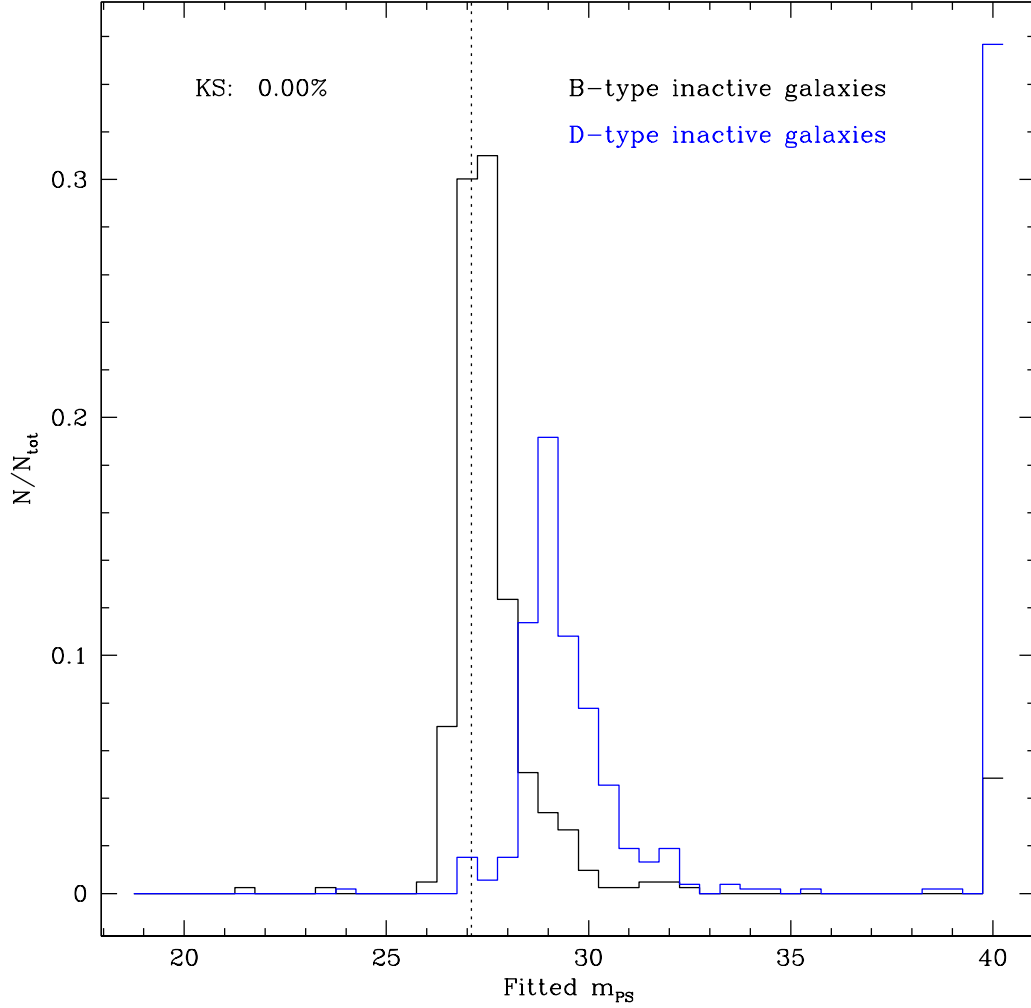
Fig. 2.15.— Distribution of fitted point-source magnitude for simulated *inactive* galaxies. Only 1% of pure disk inactive galaxies (blue histogram) recovers point-source magnitudes brighter than the 10σ detection limit (dotted line) for the GOODS survey (from which our noise properties are taken). When the galaxy is a pure bulge (black histogram), however, a point source is found above the 10σ threshold in approximately 25% of fits. The overall percentage of fits where a point-source is found when none exists is 12% (for both pure bulges and pure disks combined), but this number is strongly dependent on intrinsic morphology.

Redshift Effects on AGN Host Galaxies

At higher redshifts, surface-brightness dimming causes loss of extended components, and an unresolved central AGN corresponds to a larger fraction of a galaxy's central region at high redshift for fixed spatial resolution. Because our GOODS data sample, as well as those of others (Sánchez et al. 2004; Grogin et al. 2005; Ballo et al. 2007; Alonso-Herrero et al. 2008), extends to $z \approx 1$, we consider the quantitative effects of redshift on morphological classification.

After applying data cuts requiring $\Delta r_e \leq 90$ pixels and $|\Delta m_{tot}| \leq 0.5$ to our results at all redshifts, we assess the reliability of using the Sérsic index to classify single-component galaxies at different redshifts in Figure 2.16. We have "classified" a galaxy as bulge-dominated if it has $n > 2.0$ and disk-dominated if it has $n < 2.0$. Figure 2.16 then shows the fraction of correctly classified B and D type galaxies at each redshift. In general, the classification of pure bulges and pure disks is highly reliable for AGN host galaxies and point sources. At all redshifts, disks and bulges are correctly classified at least 90% of the time using these data cuts. Without these cuts, the misidentification rate increases to as much as 15%.

The average recovery of input half-light radius for all our simulated galaxies (pure bulges and disks as well as B+D bulges and disks) is shown in Figure 2.17. Each point represents the peak of the distribution of Δr_e values for a single galaxy type/component in each redshift bin. The error bars give the limits of the central 68% of data points; the peak of each distribution is generally not coincident with the numerical "center" of each bin. Single-component Sérsic fits to pure bulges and disks recover the radius reliably at all redshifts. Fitted radii to bulge and disk components in B+D hosts recover the intrinsic radius of the component to within 1 kpc on average; however, the errors are larger and these fits are more uncertain. For example, the width (containing 68% of sources) of the
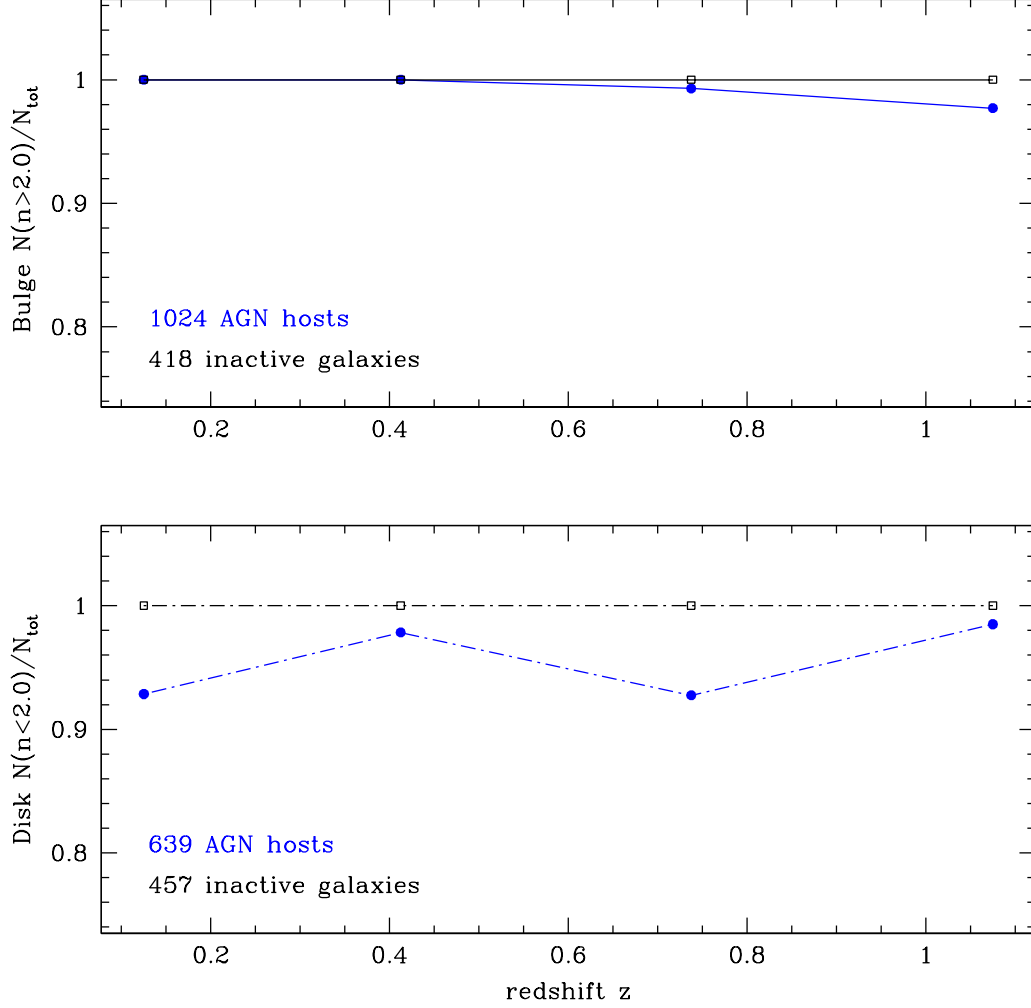
Fig. 2.16.— Dependence of galaxy classification on redshift for simulated bulge galaxies ($n_{in} = 4$; top, solid lines) and disk galaxies ($n_{in} = 1$; bottom, dot-dashed lines) with (blue) and without (black) central point sources. The y-axis is the fraction of galaxies correctly identified as bulges or disks given a threshold of $n > 2.0$ for bulge-dominated classification and $n < 2.0$ for a galaxy with a significant disk. Although we have here adopted a cutoff of $n = 2.0$, the results change by less than 5% when we change the cutoff to values between $1.5 < n < 3$.
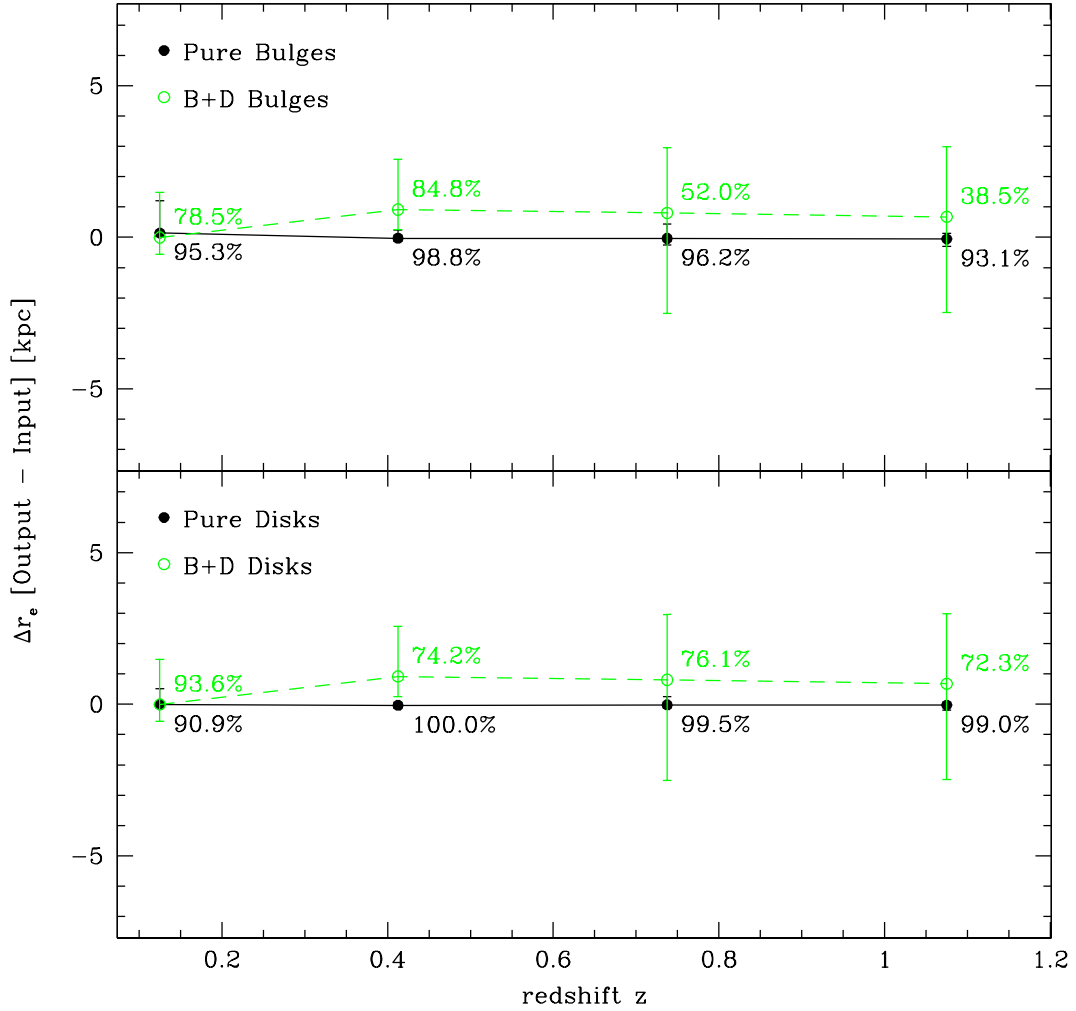
Fig. 2.17.— Recovery of input radii for pure and B+D bulges (top panel) and disks (bottom panel). Each point represents the peak of the distribution of single-component (black, solid lines) and two-component (green, dashed lines) Δr_e at each redshift. The numbers next to each point indicate the percentage of completed fits with $r_e > 5$ and $\Delta r_e \leq 90$ pixels, so that the fit converged to a physical value and would not be rejected by eye based on the fit residuals. While median fitted bulge and disk sizes are generally accurate to within 1 kpc at all redshifts, the presence of a central point source increases the spread in the distribution by up to a factor of 3. In addition, the majority of bulge fits within B+D galaxies at $z \approx 1$ are not able to converge to a sensible value for the bulge radius.

Δr_e distribution of $z \approx 1$ pure disks is less than 1 kpc, whereas the width of the $z \approx 1$ distribution of Δr_e for disk components in B+D hosts is approximately 3 kpc. Although the average recovery of bulge and disk component radii in B+D galaxies is accurate to within 1 kpc, individual radii are highly uncertain.

The percentage of sources remaining after removing fits with incorrect total magnitudes and unphysically low or high values of r_e, as previously discussed, is also shown for each bin in Figure 2.17. The number of fits for which the fitted $r_e < 5$ pixels remains relatively constant with redshift, but the number of fits for which the fitted r_e value diverges increases with redshift, more dramatically so for bulges than for disks. In the $z \approx 1$ sample, fewer than 40% of bulges within two-component fits have fitted radii within a reasonable physical range. This is likely due not just to the presence of the additional disk component, but also to the fact that the bulge is much smaller at higher redshift compared to the size of the central point source. In these cases, the bulge and the point source can be confused, often resulting in a divergent bulge fit. This happens less frequently for disks for two reasons: first, disks are generally more extended than bulges, and second, the radial profile of the ACS PSF more closely resembles that of a deVaucouleur bulge than an exponential disk.

Because different fractions of galaxies are removed from the sample at different redshifts (and for different bulge sizes), the morphological composition of a galaxy sample may be altered from its intrinsic composition simply by applying a reasonable cut on the morphological fit parameters, even if this cut is applied evenly (as it is in Figure 2.17).

Figure 2.18 thus shows the fitted morphological fraction of bulges with redshift of our simulated sample of pure bulges and disks for both AGN hosts and inactive galaxies. After applying the radius and magnitude cuts above (*i.e.*, removing only unphysical fit results from the sample), we calculate the fraction of galaxies in each redshift bin that would be classified as bulge-dominated according to a $n > 2$ cut. For a perfectly-
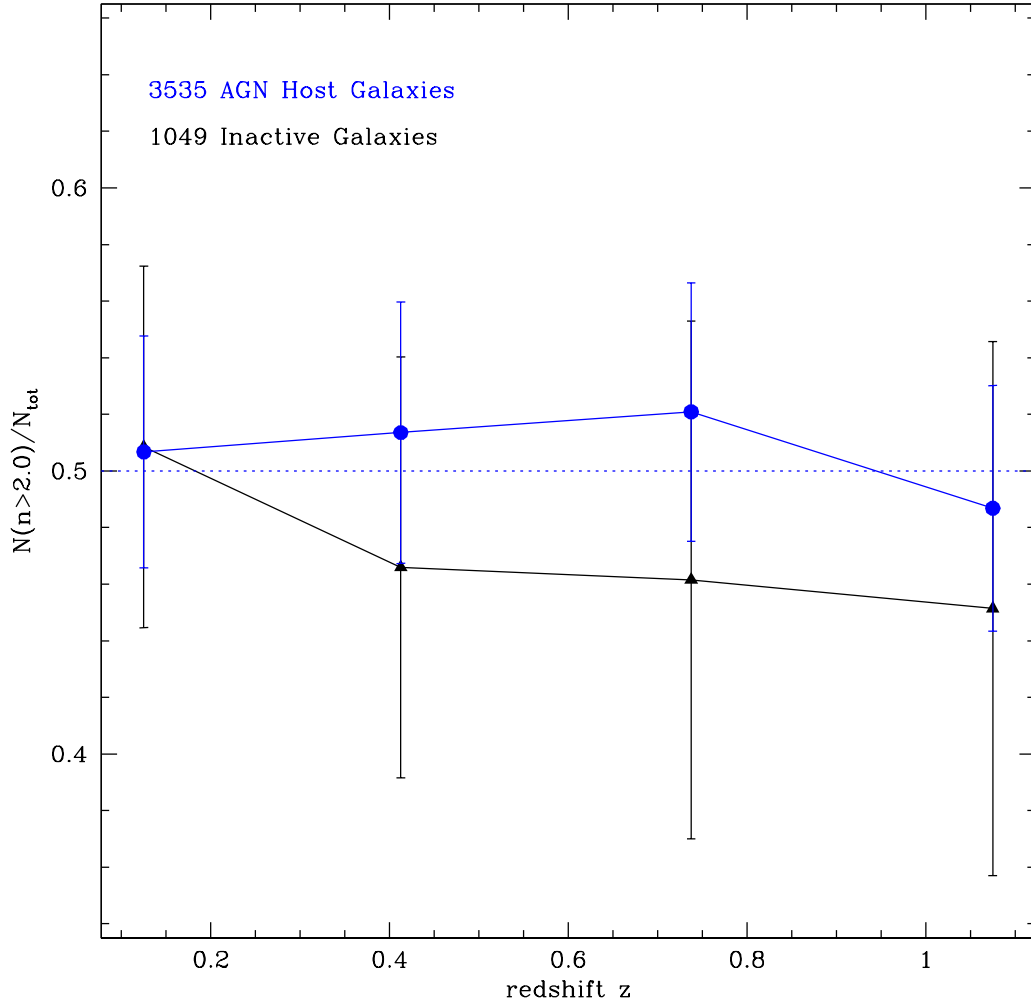
Fig. 2.18.— Fraction of galaxies classified as bulges with redshift. Blue circles represent simulated AGN hosts, and black triangles represent simulated inactive galaxies (error bars determined using Poisson statistics). Because the initial simulation contains equal numbers of pure bulges and disks, the actual bulge fraction is 0.5 for both samples. At the lowest redshift bin, these fractions are recovered to within 1% for both samples. The sample of simulated AGN host galaxies is mis-classified by up to 2% (0.02), and the inactive sample is mis-classified by up to 5%. Uncertainties are higher for inactive galaxies due to lower numbers of galaxies in the inactive sample, but in both cases the recovered fractions are consistent with the correct fraction within the uncertainties.

recovered sample, this fraction would be $N(n > 2.0)/N_{tot} = 0.5$ at all redshifts, because we simulated equal numbers of bulges and disks. However, the convergence rate for pure bulge and disk fits is slightly different at each redshift, and even our set of reasonable and conservative error cuts removes different fractions of bulge and disk galaxies at each redshift. While this does affect the morphological composition of the sample at each redshift, its effect is small: the morphological fraction of $n > 2$ galaxies for AGN hosts is typically within 2% of the intrinsic fraction at all redshifts. The inactive galaxy morphological fraction is within 5% of the intrinsic fraction at all redshifts; both samples are consistent within their uncertainties with the intrinsic fraction.

For the two-component B+D galaxies, the dependence of fitted Sérsic index on input bulge-to-total ratio is shown in Figure 2.19. We see a general dependence of fitted n on the intrinsic bulge-to-total ratio. The relation changes somewhat as the sample is redshifted, but at all redshifts the Sérsic index indicates that galaxies may be fitted with a Sérsic index indicative of a pure bulge ($n = 4$) even in cases where a disk is present and contributing up to 45% of the total galaxy light. However, a fitted Sérsic index consistent with an exponential disk ($n = 1$) typically indicates very little bulge contribution ($< 10\%$); galaxies fitted with $n < 1.5$ have $(L_B/L_{tot}) < 0.2$. Intermediate values of the Sérsic parameter, $1.5 < n < 3$, generally indicate a galaxy with both bulge and disk, but the bulge-to-total ratio may vary between $0.2 \leq (L_B/L_{tot}) \leq 0.65$, indicating that it is impossible to determine with a single-component fit whether a host galaxy with an intermediate Sérsic index is intrinsically bulge- or disk-dominated. Given that two-component B+D fits are also uncertain in the presence of a central point source, we conclude that determination of the bulge-to-total ratio is uncertain by at least 20% in AGN host galaxies, with a higher uncertainty for hosts with intermediate Sérsic indices and/or fitted (L_B/L_{tot}).

Figure 2.20 shows the recovery of detected input point sources, hosts, and host-to-
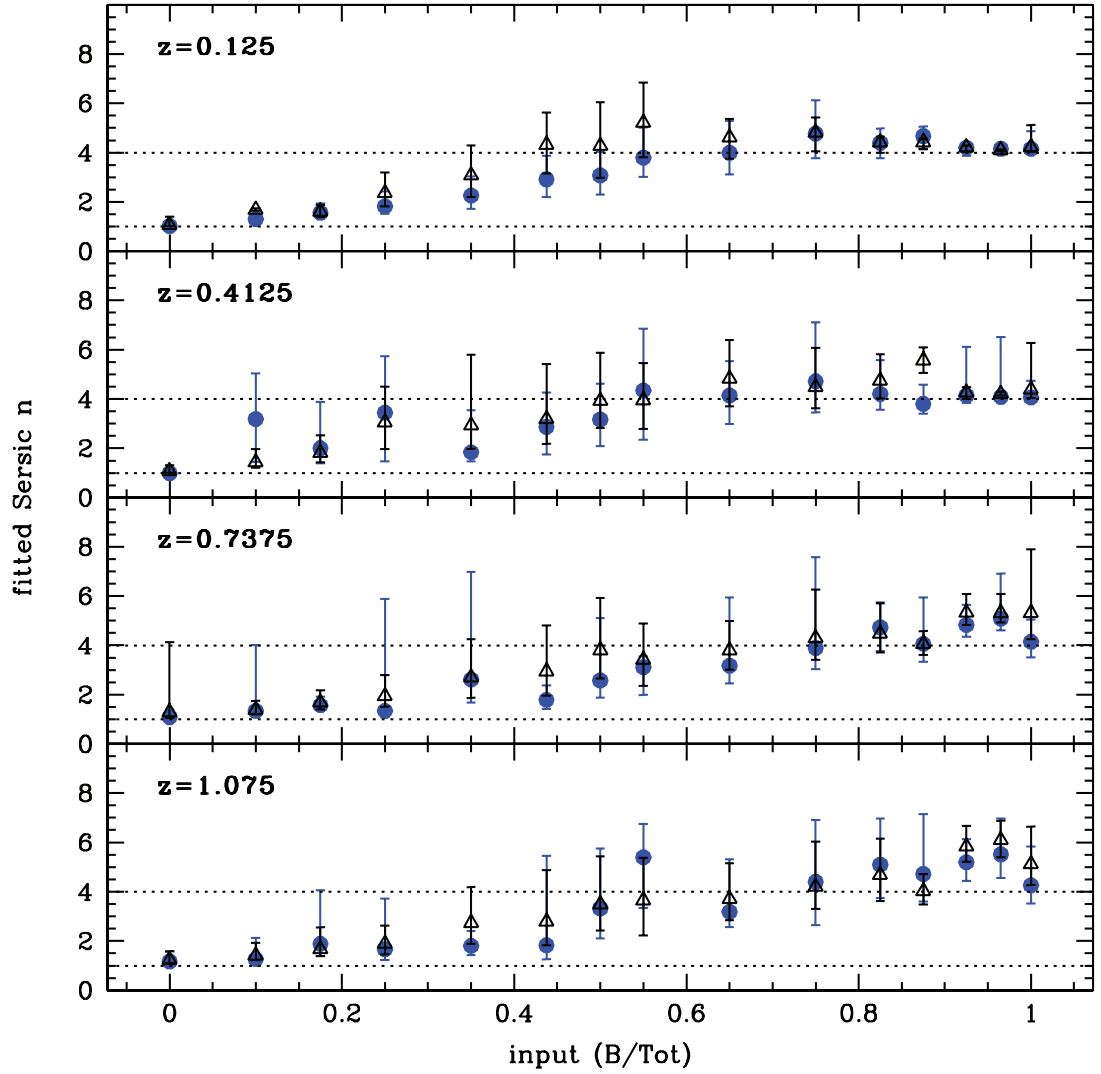
Fig. 2.19.— Fitted Sérsic index vs. input bulge-to-total ratio, for simulated normal galaxies (black triangles) and galaxies with added point sources (blue circles). At all redshifts (low to high, top to bottom) the fit correctly finds disks ($n = 1$) at $(L_B/L_{tot}) = 0$ and bulges ($n = 4$) at $(L_B/L_{tot}) = 1$. However, some galaxies fit to Sérsic values of $n \geq 4$ despite having up to 30% of their intrinsic light from a disk. Galaxies with intermediate values of n ($2 < n < 4$) likely have bulges which contribute between 20% and 70% of the total galaxy light. Points plotted are the median of each bin's distribution; error bars mark the widths of each distribution enclosing the central 68% of sources in the bin.

PS contrast ratios for our simulated galaxies (B, D, and B+D) at all redshifts. Again we see that for the local sample, the recovery is excellent: not only are point sources detected at least 95% of the time, the recovered magnitude is typically within at least 0.1 ± 0.12 dex of the intrinsic magnitude. In fact, point-source recovery is very good at all redshifts: the recovered magnitude is within 0.5 dex of the input magnitude for all redshifts and input point-source magnitudes.

The dispersion in recovered values for the host galaxy magnitude is higher than that of point-source magnitude values for all redshifts. While in the local redshift bin the median recovered host magnitude is within 0.1 dex of the input magnitude, the central 68% of values has a larger spread. At higher redshifts, the host galaxy is more likely to converge to magnitudes that are too bright compared to the input magnitude. This effect is more pronounced for sources with a brighter input point source, as expected. For sources with a bright point source compared to the host, the difference is $\Delta m_{host} = 0.6$ for $z > 0.7$. For $z \approx 1$, the distribution of Δm_{host} has an extended tail to negative (too-bright) values: a significant fraction of high-redshift sources overestimates the host brightness by up to 1.8 dex regardless of the host-to-PS contrast ratio. For $z < 1$, this tail also exists for all host-to-PS values. However, when the input point source is faint compared to the host, the host magnitude is fitted to within $-0.8 < \Delta m_{host} < 0.3$ (1σ) for these redshifts.

2.5   Summary and Conclusions

We simulated 54,418 GOODS ACS galaxy images of inactive and AGN host galaxies at redshifts $0.125 < z < 1.25$, the largest sample of simulated two-dimensional galaxy morphologies to date.

Using a robust initial guess routine followed by batch-fitting, we performed single-
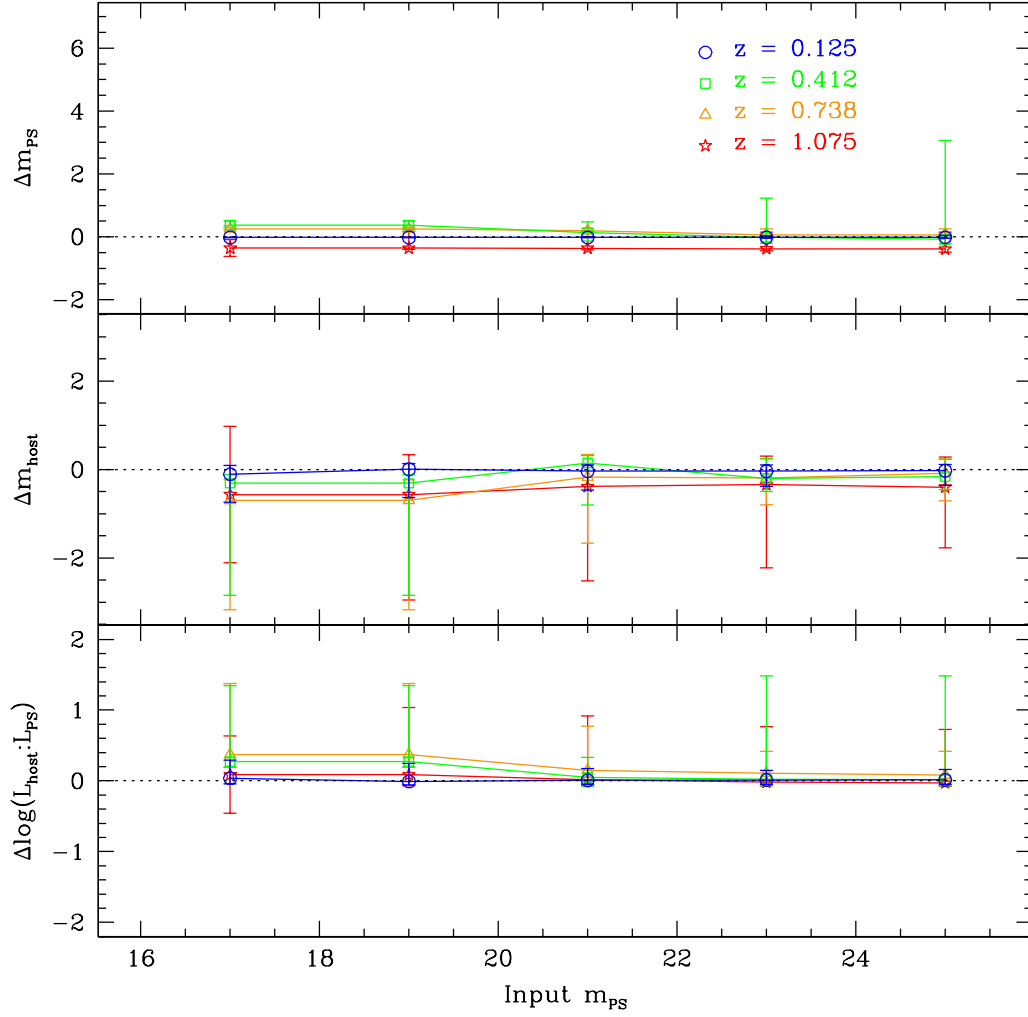
Fig. 2.20.— Effects of redshift on recovery of input point sources (top), input host magnitudes (middle), and host-to-PS contrast ratio, shown for all our simulated host galaxies. Each panel shows the fitted quantity versus the input point-source magnitude. Each line in a panel represents a different redshift bin: $z = 0.125$ (blue, circles), $z = 0.4125$ (green, squares), $z = 0.7375$ (orange, triangles), and $z = 1.075$ (red, stars).

component and Bulge-Disk host galaxy fits on these simulated galaxies, while also extracting the central point-source components of the AGN.

For batch-fit galaxies with central point-source components, typically 60-70% of the fits converge successfully and pass our error cuts. This percentage can be significantly increased by follow-up case-by-case fitting, starting from the results of the batch fitting routines.

We reliably extract central point-source magnitudes for the simulated AGN using a simple χ_ν^2 cut on the recovered fits. Using a combination $\chi_\nu^2 < 2$ and relative effective radius error cut of $(\sigma_{r_e}/r_e) = 0.8$ removes 88% of the poor host galaxy fits while excluding 12% good host galaxy fits. The accurate extraction of AGN and host galaxy parameters does not depend on the Host:AGN contrast ratio $(L_{\mathrm{host}}/L_{\mathrm{PS}})$, as long as it is greater than 1:4.

Galaxy size is recovered to within $\Delta r_e < 1$ kpc for single-component galaxies. For individual bulges and disks within two-component Bulge + Disk host galaxy fits, the distribution of recovered radii peaks within $\Delta r_e < 1$ kpc at all redshifts, but the large width of the distributions indicates that individual fits to bulges and disks within two-component galaxies are highly uncertain.

The average recovered morphological fraction of our sample is within 5% of the true fraction, even at $z \approx 1$. Of course, this number should be regarded as a lower limit since actual data samples of two-dimensional AGN host galaxy morphologies are likely to be significantly smaller than our simulations, and thus suffer from more uncertain statistics. We recover the correct morphology 99% of the time for inactive galaxies out to $z = 1.25$.

The average bulge-to-total ratios are within 10% of the true ratio at all redshifts, but with large scatter ($\sim 50\%$). This means that values for individual hosts are unreliable at the 50% level, but statistical population averages are more accurate. Thus, uncertainties

in individual black hole masses determined using $L_{bulge} - M_{BH}$ relations (McLure & Dunlop 2002; Marconi & Hunt 2003; Ferrarese & Ford 2005) are higher when using fitted bulge luminosities of AGN host galaxies than those of inactive galaxies, and may be systematically overestimated due to the presence of central point sources.

Galaxies with Sérsic $n < 1.5$ are generally disk-dominated, with at least 80% of their total light coming from a disky component. Galaxies with intermediate $1.5 < n < 3$ have larger bulge components (occupying from 20 - 65% of the total galaxy light). Galaxies that appear to be bulge-dominated, *i.e.*, with $n \geq 3$, may derive as little as 45% (depending on redshift) of their total light from a bulge component; for $n = 4$, typically $\sim 70\%$ of the galaxy light comes from the bulge.

In fully simulated AGN host galaxies, the central point source is correctly detected over 90% of the time, with only weak dependence on the intrinsic contrast ratio between the host galaxy and point source or the host morphology. This indicates that a sample of AGN host galaxy fits to ACS data with $z < 1.25$ is at least 90% complete in its detection of central point sources.

However, we also detect spurious point sources in simulated galaxies where no central point source is present, for as little as 1% or as high as 25% of the galaxies, depending on the morphological composition of the sample. Fits to bulge-dominated galaxies are far more likely to detect a point source when none is present than fits to disk-dominated galaxies.

We have used these simulations to evaluate the robustness of our results for AGN host galaxies observed with ACS. This is important for assessing the accuracy of recovered host morphologies, as well as the evolution of AGN host morphology with redshift. All of our results that can be quantitatively applied to a sample of real AGN host galaxies are also presented in tabular format (Tables 2.2, 2.3, and 2.4).

We have performed these simulations using the image depths and noise properties

of the GOODS survey, but they may also be used for other ACS surveys such as GEMS (Rix et al. 2004), COSMOS (Scoville et al. 2007), and AEGIS (Davis et al. 2007). The extent to which these simulations are directly applicable or provide limits on the accuracy of AGN host galaxy morphological fits for other ACS data depends on the relative depth of observations in each survey.

It is important to note that these results apply to redshifts where the ACS bands are observing rest-frame optical data, e.g. $z < 1.25$. As we move into the era of newer telescopes such as *JWST* and observing rest-frame optical wavelengths at very high resolution becomes possible for higher redshifts, an understanding of the effects of a central point source on high-redshift morphologies will become crucial. Simulations to probe these effects have begun on small scales (Dasyra et al. 2008), but more such work is needed.

| | Pure Bulges | Pure Disks | Bulge + Disk | |
			Bulge	*Disk*
m_{gal} (I_{AB}, L_*)	16.898, 5.0 18.645, 1.0 19.398, 0.5 20.393, 0.2	16.898, 5.0 18.645, 1.0 19.398, 0.5 20.393, 0.2	16.898, 5.0 18.645, 1.0 19.398, 0.5 20.393, 0.2 20.750, 0.14	16.898, 5.0 18.645, 1.0 19.398, 0.5 20.393, 0.2 20.750, 0.14
r_e (pixels, kpc)	13.54, 1.5 27.09, 3.0 40.63, 4.5 54.18, 6.0	36.12, 4.0 54.18, 6.0 72.23, 8.0 90.09, 10.0	27.09, 3.0 40.63, 4.5 54.18, 6.0	54.18, 6.0 72.23, 8.0 90.29, 10.0
b/a	0.25 0.50 0.75 1.0	0.25 0.50 0.75 1.0	0.65 1.0	0.30 0.65 1.0
PA (degrees)	45.0	45.0	45.0 60.0	45.0
m_{PS} (I_{AB})	none 16.500 18.375 20.250 22.125 24.000	none 16.500 18.375 20.250 22.125 24.000	none 16.500 20.250 22.125	

Table 2.1: Grid values for simulated galaxies at $z = 0.125$. The effective radius r_e values differ between the bulge and disk galaxies due to the different physical sizes of these two classes of galaxies. The parameter space varies slightly between single-component galaxies and double-component galaxies in order to increase the number of mesh points in the bulge-to-total ratio without increasing the simulated double-component galaxies to a computationally prohibitive number. Conversion from magnitude to luminosity and between pixels and physical size uses a concordance cosmology ($\Omega_{tot} = 1$, $\Omega_\Lambda = 0.73$, and $H_0 = 71$ km/s/Mpc) and a redshift $z = 0.125$.

Source m_{PS}	N_{conv}	$\sigma_{m_{PS}}$	N_1	$\sigma_{m_{host}}$	σ_n	σ_{r_e}	N_2
(AB)						(pixels)	
21	374	0.33	210	1.09	2.10	15.6	45
22	389	0.48	273	0.12	0.97	21.8	85
23	397	0.27	359	0.15	0.67	11.0	138
24	394	0.15	328	0.20	0.54	26.7	184
25	382	0.17	328	0.14	0.40	15.9	223
26	372	0.27	295	0.17	0.44	8.2	215
27	355	0.47	271	0.12	0.27	7.9	215
28	315	0.87	228	0.10	0.22	6.3	192
29	286	1.20	193	0.09	0.27	1.6	161

Table 2.2: RMS values for fit parameters vary with central point-source magnitude. N_{conv} is the number of fits which converged (out of 450) for each input point-source magnitude value. N_1 is the number remaining after applying a $\chi^2_\nu < 2.0$ cut; N_2 is the number remaining after further requiring $\sigma_{r_e}/r_e < 0.8$. The RMS value for the point-source magnitude is calculated from N_1 galaxies, and the values for $\sigma_{m_{host}}$, σ_n, and σ_r are calculated from N_2 objects. *Note:* Results for these magnitudes are based on a survey with the GOODS depths (Giavalisco et al. 2004).

Source $\log(L_{host}/L_{PS})$	$\sigma_{m_{PS}}$	$\sigma_{m_{host}}$	σ_n	σ_{r_e}
				(pixels)
-1.5	0.26	0.78	0.70	7.2
-1.0	0.31	0.29	0.38	6.2
-0.5	0.31	0.31	0.31	7.1
0.0	0.36	0.35	0.27	5.4
0.5	1.69	0.32	0.24	4.4
1.2	1.92	0.23	0.33	4.6
1.9	0.69	0.07	0.20	3.4

Table 2.3: Determined RMS values for fit parameters to sources with different $\log(L_{host}/L_{PS})$.

Fitted Sérsic index	Intrinsic bulge-to-total ratio
$n \leq 1.5$	$(\mathrm{B}/\mathrm{Tot}) < 0.2$
$1.5 < n < 3$	$0.2 < (\mathrm{B}/\mathrm{Tot}) < 0.65$
$n \geq 3$	$(\mathrm{B}/\mathrm{Tot}) > 0.45$
$n \geq 4$	$(\mathrm{B}/\mathrm{Tot}) > 0.55$

Table 2.4: Relationship of a host galaxy's fitted Sérsic index to its intrinsic bulge-to-total light ratio. Hosts with intermediate Sérsic index may have a wide range of bulge-to-total ratios; hosts with fitted $n = 4$, typically classified as pure deVaucouleur bulges, may in fact have bulge-to-total ratios as low as 55%.

Chapter 3

Obscured GOODS AGN and Their Host Galaxies at $z < 1.25$: The Slow Black Hole Growth Phase

Abstract

We compute black hole masses and bolometric luminosities for 87 obscured AGN in the redshift range $0.25 \leq z \leq 1.25$, selected from the GOODS deep multi-wavelength survey fields via their X-ray emission. We fit the optical images and obtain morphological parameters for the host galaxy, separating the galaxy from its central point source, thereby obtaining a four-band optical SED for each active nucleus. We calculate bolometric luminosities for these AGN by reddening a normalized mean SED of GOODS broad-line AGN to match the observed central point-source SED of each obscured AGN. This estimate of L_{bol} has a smaller spread than simple bolometric corrections to the X-ray luminosity or direct integration of the observed multi-wavelength SED, suggesting it

---

is a better measure. We estimate central black hole masses from the bulge luminosities. The black hole masses span a wide range, $7 \times 10^6 M_\odot$ to $6 \times 10^9 M_\odot$; the median black hole mass is $5 \times 10^8 M_\odot$. The majority of these AGN have $L/L_{Edd} \leq 0.01$, and we detect no significant evolution of the mean Eddington ratio to $z = 1.25$. This implies that the bulk of black hole growth in these obscured AGN must have occurred at $z \gtrsim 1$ and that we are observing these AGN in a slow- or no-growth state.

3.1   Introduction

Accurately estimating the mass and growth of supermassive black holes (SMBHs) in the centers of massive galaxies is critical to the field of galaxy formation and evolution. Calculations of black hole masses from direct observables have been limited to only a few methods: stellar kinematics from within the black hole sphere of influence (Genzel et al. 1997; Ghez et al. 2005); H_2O maser kinematics (Miyoshi et al. 1995; Herrnstein et al. 1999; Greenhill et al. 2003); kinematics of central gaseous disks (Ford et al. 1994; Ferrarese & Ford 1999); and reverberation mapping (Peterson 1993; Peterson & Wandel 2000). These methods, while powerful and tested, are mostly restricted to bright galaxies and luminous active galactic nuclei (AGN) in the local universe.

Far more common are obscured AGN, which by definition have a reddened (fainter) central point source and often resemble a normal galaxy at optical and near-infrared wavelengths. These comprise a large fraction of all AGN and contribute much of the X-ray background (Ueda et al. 2003; Treister & Urry 2005, 2006; Treister et al. 2004, 2006, 2008, 2009). The high luminosity ratio between host galaxy and obscured point source makes indirect black hole mass ($M_\bullet$) estimates, such as the $M_\bullet - L$ (where L is the galaxy or bulge luminosity) relation (Marconi & Hunt 2003), much more promising than in quasar hosts, as well as one of the only methods available given that nuclear

emission, including broad lines, is usually obscured in these sources.

Combining black hole masses with bolometric luminosities gives an important intrinsic property of AGN, the Eddington ratio, $\lambda \equiv L/L_{Edd}$, as well as the associated dimensionless accretion rate, $\dot{m}_{acc} \equiv \dot{M}c^2/L_{Edd}$. These quantities indicate how fast a black hole is growing: only accretion approaching (or exceeding) the Eddington limit leads to an appreciable increase in black hole mass. From well-studied spectral energy distributions (SEDs) of unobscured Type 1 quasars (Sanders et al. 1988; Elvis et al. 1994; Richards et al. 2006), one can derive bolometric corrections for AGN with less complete SEDs (Elvis et al. 1994; Fabian & Iwasawa 1999; Elvis et al. 2002; Marconi et al. 2004; Hopkins et al. 2007). However, these bright quasars are rare among the larger AGN population (AGN found in deep *Chandra* exposures are generally $10 - 100$ times less luminous) and bolometric corrections for the more common, lower-luminosity AGN are much less certain.

Detailed study of large samples of AGN and host galaxies has recently become possible via large multi-wavelength surveys (e.g., GOODS, COSMOS, ECDFS) that include X-ray and infrared data as well as high-resolution, deep optical imaging with the Hubble Space Telescope (*HST*). The unparalleled resolution of the Advanced Camera for Surveys (ACS) resolves typical AGN host galaxies and point sources out to $z \sim 1$ (Sánchez et al. 2004; Ballo et al. 2007; Pierce et al. 2007; Alonso-Herrero et al. 2008; Gabor et al. 2009, but also see, *e.g.,* Grogin et al. 2003 and Schawinski et al. 2011 for other *HST* instruments), and simulations have confirmed the reliability of host and point-source separation for obscured AGN out to these redshifts (Simmons & Urry 2008). Here, we utilize the Great Observatories Origins Deep Survey (GOODS, Giavalisco et al. 2004) X-ray through 24 μm data to characterize separately the active nuclei and the host galaxies of a large sample of moderate luminosity, obscured AGN.

The separation of the host galaxy from the AGN point source allows us to determine

simultaneously the SED of the AGN alone and the $M_\bullet$ (from the host galaxy, using the $M_\bullet$-L_B relation, where L_B is the rest-frame B-band bulge luminosity). We can then extrapolate the AGN luminosity to the far-infrared based on the level of reddening in the optical point source, and thus estimate the bolometric luminosity. Coupled with black hole mass, this allows us to determine Eddington luminosities and ratios for obscured AGN over the redshift range of $0.25 < z < 1.25$. We discuss the data and sample selection in Section 3.2. Section 3.3 describes the black hole mass estimation, including treatment of time variability of the black hole-bulge luminosity relation, and Section 3.4 details how we calculate bolometric luminosities and discusses the reliability of our methods. In Section 3.5 we discuss the derived Eddington luminosities and ratios for our sample.

Throughout this paper, we adopt $H_0 = 71$ km/s/Mpc, $\Omega_M = 0.27, \Lambda_0 = 0.73$, consistent with the *WMAP* cosmology (Spergel et al. 2003).

3.2 Data

3.2.1 Sample Selection

In order to reliably extract AGN light from the combined light of an AGN plus its host galaxy, we require deep observations using an instrument with a point-spread function (PSF) that is small compared to the size of the galaxy. The excellent depth and resolution of the of the GOODS *HST* observations provide an excellent opportunity for studying moderate-luminosity AGN ($L_X = 10^{42} - 10^{44}$erg s^{-1}) out to high redshifts ($z \geq 2$). The GOODS data include the space-based Chandra Deep Fields in the X-ray (0.5-8 keV; Giacconi et al. 2002; Alexander et al. 2003), four *HST*/ACS filters in the optical (F435W, B; F606W, V; F775W, i; F850LP, z_{850}; Giavalisco et al. 2004), all four

Spitzer/IRAC bands in the infrared (3.6, 4.5, 5.8, 8.4 μm), *Spitzer*/MIPS 24 μm (Treister et al. 2006, Dickinson et al., in preparation, Chary et al., in preparation) and the ground-based FLAMINGOS J and K bands and SOFI/ISAAC JHK bands for GOODS-North and South, respectively.

We define our AGN sample by the following criteria:

1. *Chandra* X-ray point source matched to an optically-detected source using a maximum-likelihood method to more than 99% confidence (Bauer et al. 2004).

2. Spectroscopic redshifts (Cowie et al. 2003; Wirth et al. 2004; Szokoly et al. 2004) at $z \leq 1.25$, so that the data cover the rest-frame B-band.

3. Total absorption-corrected hard X-ray luminosity, L_X (2-8 keV) $\geq 3 \times 10^{42}$erg s^{-1} to minimize contamination from pure starburst galaxies with no AGN (Persic et al. 2004).

This results in an initial sample of 121 AGN, with 68 from GOODS-North and 53 from GOODS-South. We apply further criteria to select a sub-sample of sources with high enough *HST* data quality for two-dimensional host galaxy fitting.

To separate a source's central (optical) AGN light from its host galaxy light using two-dimensional parametric fitting techniques requires high-resolution data and relatively high signal-to-noise for each source (> 5 per pixel). To ensure the highest quality fits, we include only sources with host $z_{850} \leq 24$ mag (AB), and with a stellarity parameter (estimated by the SExtractor parameter, CLASS_STAR; Bertin & Arnouts 1996) less than 0.85, where CLASS_STAR $= 1$ is a pure point source. Following this cut, we retain 90 AGN (51 from GOODS-N, 39 from GOODS-S), of which 9 are broad-line objects. Figure 3.1 shows the distributions of L_X, M_{850lp}, and z for X-ray sources with $z < 1.25$ in the GOODS fields. We further exclude three sources for which we were unable to isolate the bulge flux. Two have extremely irregular and disrupted optical morphology,
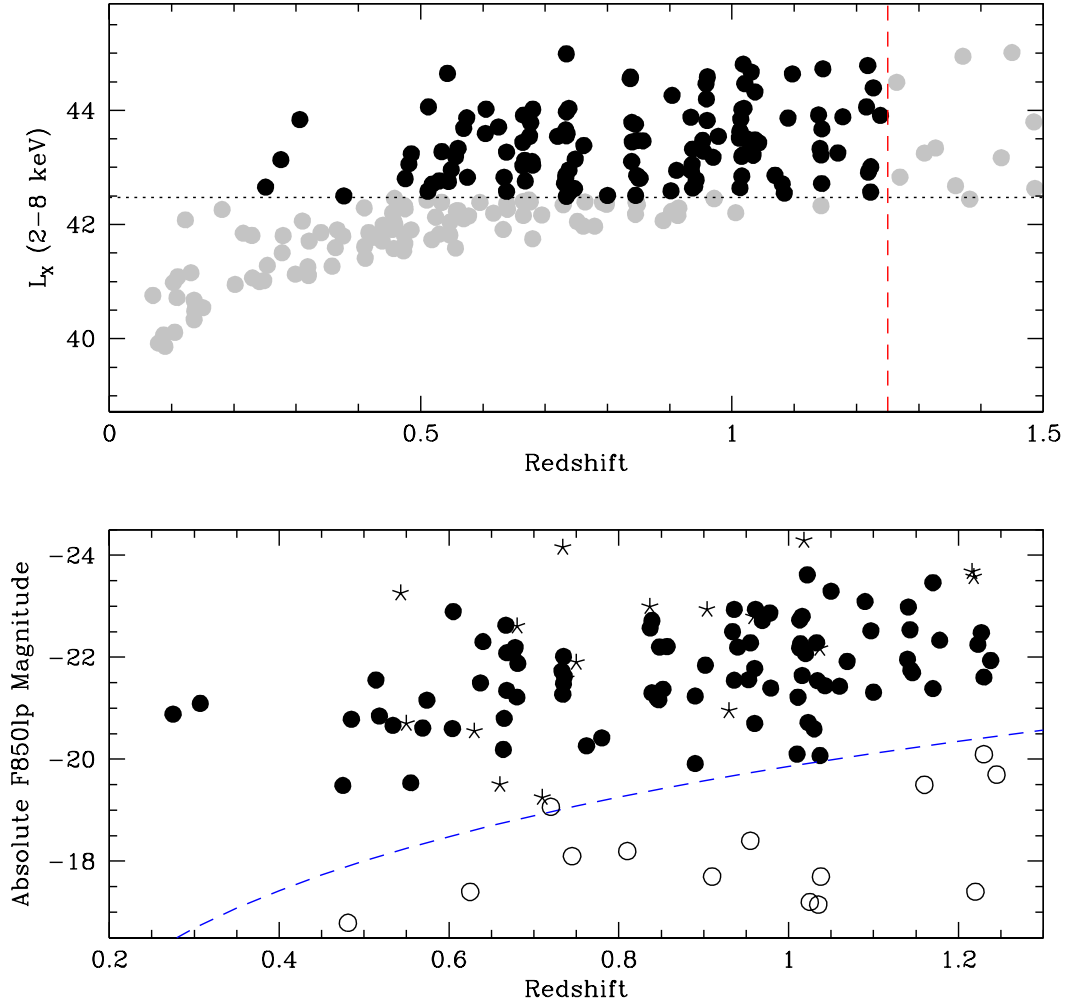
Fig. 3.1.— *Top:* Hard X-ray luminosity vs. redshift for GOODS X-ray-selected, optical z_{850}-detected galaxies with spectroscopic redshifts. The AGN sample defined by our X-ray and redshift selection criteria (dashed lines; $L_X > 3 \times 10^{42}$ erg s^{-1}, $z < 1.25$) are black; excluded sources are gray. *Bottom:* Absolute z_{850} host magnitude vs. redshift for the sample AGN in the top panel. For accurate morphological fitting, we also require sources with host $z_{850} < 24$ mag (blue dashed line) and a stellarity index indicative of an extended source (< 0.85). All 87 sources meeting those criteria are shown as black filled circles. Faint sources with host $z_{850} > 24$ are shown as open circles; point-like sources with host $z_{850} < 24$ are shown as stars.

making morphological descriptions in terms of bulges and disks meaningless, and one has a marginal CLASS_STAR $= 0.845$; all three are among the lowest optical luminosity, with a mean $M_B = -19.05$, nearly an order of magnitude below the next lowest AGN host ($M_B = -20.2$; see Figure 3.1). The remaining 87 AGN+hosts constitute our final sample.

3.2.2   Point Source-Host Galaxy Decomposition

We perform morphological decomposition of the GOODS AGN+host galaxies using the 2-D fitting routine GALFIT (Peng et al. 2002). This routine allows for simultaneous fitting of one or more host galaxy components along with a central point source. We used the GOODS ACS images that were processed using the STScI Multidrizzle algorithm (Koekemoer et al. 2002), improving the native resolution to 0.03 arcsec/pixel.

We fit each source independently in each ACS band (B, V, I, and z_{850}) with a three-component fit: a deVaucouleur bulge + an exponential disk + a nuclear point source, the latter of which is modeled by a noiseless, analytical PSF based on analysis of dozens of real stars in the GOODS fields, created independently for each band using the IRAF package daophot. This PSF creation method minimizes the effects of potential eccentricities of any one star on the field (such as color or excess noise), while still accounting for any possible deviations within our drizzled data from a purely analytical PSF created from a package such as TINY TIM (Krist 1993).

Each galaxy was initially fit using an automated program (described in further detail in Simmons & Urry 2008, hereafter S08) that uses SExtractor catalog values as initial parameter guesses. The primary goal of the initial fit is to fix the central positions of the host and point source and to calculate initial estimates of the fit parameters. Each galaxy was then fit with GALFIT by hand to achieve the best possible fit, assessed using the χ^2 goodness-of-fit parameter and examination of fit residuals. We then calculate the

rest-frame B-band bulge-to-total ratios and point-source and host galaxy luminosities, using the InterRest interpolation code from Taylor et al. (2009); see Table 1 for total, point source, and host galaxy magnitudes and associated errors. Separated hosts and point sources for six objects in our sample are shown in Figure 3.2.

Reliable calculations of AGN black hole mass and bolometric luminosity require accurate measurements of each source's host galaxy-to-point source luminosity and bulge-to-total ratios, which are determined by our morphological fitting. S08 simulated over 50,000 AGN host galaxies in order to assess the limits of the morphological fitting. The simulations show that the determination of L_{host}/L_{PS} is generally reliable to the flux and redshift limits of our sample. Brighter point sources introduce greater uncertainty into the recovered parameters, especially the host galaxy magnitude and bulge-to-disk ratio (S08). We add these uncertainties in quadrature with the fit errors, which in turn affects the uncertainties in our black hole masses and Eddington ratios.

For samples like ours, automated fitting of AGN and hosts recovers at least 90% of central point sources (S08); our recovery fraction should be higher due to the fact that we fit each source individually. S08 also find a spurious point-source detection rate of approximately 12% in a single-band sample with equal numbers of bulge- and disk-dominated sources. However, this is an upper limit for our sample, since the chance of spurious detections or unrecovered point sources in multiple bands for a single source is extremely small. Statistically, the probability of a missed point source in 2 (3, 4) bands is 1% (0.1%, 0.01%) for one source. The probability of a spurious detection in 2 (3, 4) bands for a source with equal contributions from a bulge and disk is 1.4% (0.2%, 0.02%), though this calculation varies with the morphology of each source. Based on the number of point sources detected in our sample and each source's individual morphology (following S08), we expect that we miss $\lesssim 3$ point source detections within the sample and have spurious detections for ~ 2 sources.

Rest-frame B-band properties of each host galaxy and central point source are given in Table 1.

3.3 Black Hole Mass Estimation

Direct kinematic measurements of black hole mass are not possible for the majority of our sample because most of the AGN are obscured. Instead we use black hole-bulge relations to estimate the black hole masses. We use the point-source-subtracted bulge luminosity to calculate $M_\bullet$ from rest-frame B-band absolute magnitudes of the host galaxy bulge using the $M_\bullet - L_B$ relation from Eq. 19 of Ferrarese & Ford (2005) as converted from Marconi & Hunt (2003):

$$\log(\mathrm{M}_\bullet) = (8.37 \pm 0.11) - (0.419 \pm 0.085)(\mathrm{B_B} + 20.0), \tag{3.1}$$

where B_B is the rest-frame B-band absolute magnitude of the galaxy bulge. Rest-frame B bulge-only absolute magnitudes range from $-16.32 > B_B > -23.27$, with an average error of $\sigma_B = 0.13$ (determined from GALFIT uncertainties added in quadrature to systematic uncertainties from S08). Within our sample, we find bulge fractions ranging from $< 5\%$ to 100%, with a median bulge-to-total ratio of 0.54. For the four cases where a bulge is undetected in the rest-frame B, we follow S08 in assuming a maximum of 5% bulge contribution, and consider those black hole masses upper limits.

The mass-luminosity relation of Eq. 3.1 is based on measurements in the local universe. Treu et al. (2004) have shown an evolution in the relation out to redshift $z = 0.3$: the rest-frame B-band mass-to-light ratio of the bulge decreases with redshift due to the fact that a higher-redshift bulge typically has a younger stellar population than a bulge at $z = 0$. Subsequent work on different samples and using different methods (Borys

et al. 2005; Alexander et al. 2008; Bluck et al. 2011) finds that black hole masses seem to lag behind bulges at even higher redshift, implying that black hole masses calculated from bulge properties are overestimated by approximately a factor of 3 at $z \sim 1$.

However, several other studies (Woo et al. 2005; Peng et al. 2006; Woo et al. 2008; Jahnke et al. 2009; Decarli et al. 2010; Merloni et al. 2010) report a decrease in the intrinsic bulge stellar mass-black hole mass relation with redshift, in the sense that bulge mass appears to evolve faster than black hole mass within our redshift range, leading to an evolution in the bulge-black hole mass relation in the opposite direction. Some of the conflicting results may be explained by differences resulting from comparing black hole masses to different quantities (stellar mass versus bulge luminosity, for example), but the picture is not yet clear. Black hole masses calculated at $z \sim 1$ may change by a factor of approximately 3 in either direction and still be consistent with previous studies.

Going forward, we quote the unevolved masses, calculated via a Monte Carlo method in order to account for uncertainties in host luminosity and bulge-to-total ratio (both determined from S08) as well as the intrinsic scatter noted in Equation 3.1 and an additional uncertainty of ± 0.47 dex to encompass the uncertainty in the evolution of Eq. 3.1 to the redshifts relevant to our sample. We generate 10^5 data points for each of our 87 sources, with uncertainties folded into each step to calculate black hole masses; the reported $M_\bullet$ values and errors represent the peak and σ values of the Monte Carlo distribution for each object. This method typically results in SMBH mass uncertainties of approximately ± 0.5 dex in log-$M_\bullet$. Using the same Monte Carlo method, we propagate these errors through to our calculation of Eddington ratios (discussed in Section 3.5).

The resulting black hole masses are shown in Figure 3.3 and presented in Table 1. The majority (94%) are between $5.0 \times 10^7 < M_\bullet < 5.5 \times 10^9$ M$_\odot$, and the rest have masses (or upper limits) down to $M_\bullet = 6.7 \times 10^6$ M$_\odot$. The median mass, $M_\bullet =$

$5.1 \pm 4.7 \times 10^8$ M$_\odot$, is indicated on Figure 3.3 as a dashed line.

3.4 Bolometric Luminosity Calculations

In order to study the properties of AGN, we need to know the total power they emit. Bolometric luminosities of AGN are thus important quantities, but they are also difficult to calculate directly for many populations of AGN. Owing to our selection criteria, the SEDs of our 87 sources are typically dominated by galaxy light at optical and near-IR wavelengths, so we do not expect that naively summing the luminosities of our sources at all wavelengths will provide a reliable estimate of total AGN power.

We therefore consider two alternative approaches: (1) an average bolometric correction to the X-ray luminosity based on unobscured broad-line AGN (§ 3.4.1), and (2) individual corrections based on fitted reddening of our main AGN sample (§ 3.4.2).

3.4.1 X-ray Bolometric Correction

Bolometric luminosities are commonly estimated using an X-ray bolometric correction, K_X, where $L_{bol,X} = K_X L_X$. Values of K_X have been derived from well-defined SEDs of optically selected, powerful quasars and range from $K_X \sim 10$ (Elvis et al. 1994) to $K_X \approx 33$ (Fabian & Iwasawa 1999) or $K_X > 50$ (Elvis et al. 2002). The K factor is luminosity- and wavelength-dependent (Marconi et al. 2004; La Franca et al. 2005; Treister & Urry 2005).

The bulk of our sample lies more than an order of magnitude below the average L_X of mean quasar SEDs such as those computed from the Sloan Digital Sky Survey (Richards et al. 2006). This suggests the K_X values from the literature may not accurately represent our sample. Since the GOODS data cover nearly 5 decades of wavelength, we calculate our own K_X value and compare to previously derived K_X.

First, we develop an SED for unobscured, broad-line AGN by averaging the 58 GOODS sources with clear broad lines and hence low reddening (Barger et al. 2003; Szokoly et al. 2004; Cowie et al. 2004), as well as $N_H < 10^{21}$ cm^{-2} (Bauer et al. 2004). We also impose the criterion $L_X > 10^{43}$ erg s^{-1} to minimize host galaxy contamination in the optical and near-IR. (Three of these sources are in our sample of 87 AGN.) Even under these conditions, 12 of the selected broad-line AGN show some signs of a K-giant stellar population in their SEDs (Barger et al. 2003; Mainieri et al. 2005), particularly at lower L_X. We then split the unobscured sample into two groups, less than and greater than $L_X = 10^{44}$ erg s^{-1}, to investigate the dependency of K_X on L_X. The median, absorption-corrected, 2-8 keV X-ray luminosity for each group is 2.4×10^{43} and 1.4×10^{44} erg s^{-1}, respectively, consisting of 32 and 26 AGN, respectively.

Figure 3.4 shows the rest-frame, error-weighted geometric mean of our intermediate-luminosity AGN in frequency bins 0.15 dex in width. Given the wide redshift range, not all wavelength bins include the same number of photometric bands for each unique object. In addition to weighting by photometric error in each bin, we also weight by the fraction of AGN in each band with respect to the total sample number (shown in the bottom panel of Figure 3.4).

For comparison, we also plot in Figure 3.4 the mean SDSS quasar SED from Richards et al. (2006). The "big blue bump" in both GOODS AGN samples (at $\sim 2500\text{\AA}$) is considerably weaker than in SDSS quasars, relative to the mean luminosity at 1 μm. This suggests that using an SDSS-derived K_X estimate would overestimate the bolometric luminosity in our AGN sample.

The integrated luminosities of the averaged broad-line AGN source SEDs are calculated by summing the 2-30 keV rest-frame L_X, the 1250 Å-8 μm broad-band luminosities and the integrated UV-to-soft X-ray assuming $L_\nu \propto \nu^{1.41}$. This results in integrated luminosities and bolometric corrections of $L_{bol,BL}(8~\mu\text{m} - 30\text{keV}) =$

4.1×10^{44} erg s^{-1} and $K_X = 14.4^{+18.6}_{-7.7}$ for the lower-luminosity broad-line AGN, and $L_{bol,BL}(8 \ \mu m - 30 \text{keV}) = 2.6 \times 10^{45}$ erg s^{-1} and $K_X = 15.2^{+16.5}_{-7.4}$ for the higher-luminosity broad-line AGN. The K_X value in the lower-luminosity broad-line AGN may be slightly high due to host contamination of the optical and near-infrared SED (we estimate this contamination increases K_X in the lower luminosity sample by $\approx 20\%$).

3.4.2 Point-Source Reddening / Dust Luminosity Method

We can derive the observed point-source SED in the four ACS bands using the results from morphological fitting. In some sources, typically in the ACS B (and possibly V) bands of higher-redshift sources, no point source is detected at all; in these cases, we calculate an upper limit for these bands based on the residual background flux. Figure 3.5 shows six examples of total broad-band SEDs (diamonds) from 24 μm to U-band, plus X-ray, and the point-source optical SEDs as red squares.

We redden an unobscured AGN template to fit the extracted point source luminosities. We use the two averaged AGN SEDs calculated in the previous section, choosing which template to use for each source based on the source's X-ray luminosity. First, we normalize the template to the absorption-corrected, hard X-ray luminosity of each source. After this normalization, the mean SED exceeds the observed rest-frame broad-band MIR luminosity by more than the uncertainty of the mean SED for only eight of our 87 sources. This indicates that the choice of template SEDs is appropriate for our sample.[2] In the rare case where the SED exceeds the observed MIR luminosity after normalizing to the hard X-ray luminosity, the mean SED is re-normalized to be consistent with the observed MIR luminosity.

We then fit the normalized spectrum to the optical point-source SED, applying

---

[2]If we were to instead use the Richards et al. (2006) SDSS quasar template, the template would exceed the MIR flux in 68% of sources.

the reddening curve of Cardelli et al. (1989) for a Milky Way ISM ($R_V = 3.1$) over the wavelength range of $0.1 < \lambda < 3.5$ μm and using a χ^2-minimization algorithm to calculate the reddening value of the nuclear emission. For sources with point source detections in three or four filters ($N_{pt} \geq 3$), the reddening average is $\langle E(B-V) \rangle = 0.47 \pm 0.37$. This increases to $\langle E(B-V) \rangle = 0.78 \pm 0.54$ for AGN with solid detections in only two bands. We note that point source SEDs with significantly different colors from the host galaxy SED are frequent enough in our sample that attempting to determine the reddening value from the combined AGN+host SED would be considerably less reliable. This is consistent with previous simulations and observations (*e.g.*, Pierce et al. 2010a,b).

The independent determination of $E(B-V)$ from reddening and N_H from X-ray absorption allows us to estimate the dust-to-gas ratio along the line of sight (Section 3.4.4). We can then estimate the total re-radiated IR luminosity of the material that is absorbing optical and UV photons from the point source, using the dust emissivity models of Draine & Li (2007) and the dust-to-gas ratios to convert the emissivity profiles to luminosity, L_{dust}.

This calculation requires two assumptions: (1) the ambient radiation field strength, U, near the dust, and (2) the physical line-of-sight path length, l, through the AGN and host galaxy. We select the Draine & Li (2007) model that has a range of $U = (1 - 1 \times 10^5)U_0$, where $U = \int_{0.09}^{8\,\mu\mathrm{m}} 4\pi J_\lambda = 4.34 \times 10^{-2}$ erg cm^{-2} s^{-1} (Mathis et al. 1983), to roughly reproduce the combination of AGN radiation field strength and the ambient galaxy radiation field. We estimate the path length to be $l = R\cos i + H\sin i$, where R is half of the physical galaxy semi-major axis (determined from the angular size and distance scale), and i is the estimated inclination. For galaxies with no detected disk to indicate orientation, we assume $i = 0$.

We find that the calculated L_{dust} does not exceed the observed 24 μm luminosity in

the majority (83%) of cases. Of the 15 sources with excess calculated L_{dust} compared to the observed SED, only one is inconsistent with AGN variability observed for a similar sample on year-long timescales (Sarajedini et al. 2006). That source, S160, has an uncharacteristically low 24 μm luminosity compared to the rest of our sample. We conclude that the selected parameters of U and l do not greatly over- or underestimate the reprocessed AGN dust emission of our sample. However, the assumption that reddening of the optical point source is due entirely to dust from an AGN torus means that the calculated L_{dust} should be considered an upper limit.

3.4.3 Comparison of Bolometric Luminosity Methods

Figure 3.6 shows a comparison between the bolometric luminosities calculated four ways: (1) by integrating the complete AGN SED we constructed for each object as described in Section 3.4.2, L_{bol}; (2) by estimating an X-ray correction using the mean broad-line AGN SEDs calculated in Section 3.4.1, $L_{bol,X}$; (3) by summing the source luminosity in all observed bands, $L_{\mathrm{tot,obs}}$; and (4) by using model-derived, luminosity-dependent bolometric corrections to the X-ray luminosity ($L_{bol,\mathrm{T09}}$; Treister et al. 2009).

For the relatively small number of objects (6) in our sample with $L_X > 10^{44}$ erg s^{-1}, using our point-source fitting method to calculate L_{bol} has close to the same result as simply adding up the total luminosity in the source SED. However, the rest of our sources are dominated by the host galaxy in the optical and infrared wavelengths, leading to a significant overestimation of AGN-only luminosity with a simple summation method. For our entire sample, the mean value of $L_{\mathrm{tot,obs}}$ is too large by approximately 80% compared to the mean L_{bol} computed using our point-source fitting method.

In contrast, the simple bolometric correction computed in Section 3.4.1 is too low by 66% on average. This is unsurprising, because our correction is derived from an observed SED that lacks FIR data at longer wavelengths than 24 μm (observed), which

can contribute significantly to the observed total luminosity. This is exacerbated when applying a correction to objects like those in our main sample, whose X-ray luminosity has been subject to circumnuclear absorption. Using the Draine (2003) dust models to estimate this FIR component in the broad-line AGN increases the value of the correction from Section 3.4.1 to a value consistent with Elvis et al. (2002), which increases the corrected luminosities, $L_{bol,X}$, to a mean value more consistent with the mean L_{bol}, but with a larger scatter (σ for $\log L_{bol,X} = 0.46$ compared to 0.33 for $\log L_{bol}$).

Both $L_{bol,X}$ and $L_{\text{tot,obs}}$ are calculated using observed properties. We assess the accuracy of our L_{bol} calculation, which combines observations with model-dependent parameters, by comparing to an independent theoretical model. Specifically, we use the luminosity-dependent bolometric corrections calculated in Treister et al. (2009) for model AGN SEDs with a range of X-ray luminosities, column densities, and orientations (Treister et al. 2006). Using the absorption-corrected X-ray luminosity of each object in our main sample to predict a bolometric correction yields a bolometric luminosity for each object, $L_{bol,\text{T09}}$.

Encouragingly, the mean values of $L_{bol,\text{T09}}$ and L_{bol} are in good agreement ($\log \langle L_{bol,\text{T09}} \rangle = 44.75 \pm 0.55$ and $\log \langle L_{bol} \rangle = 44.74 \pm 0.33$), with the distribution of $L_{bol,\text{T09}}/L_{bol}$ having a peak and width (σ) of 1.0 ± 0.8. This indicates that the prediction of the Treister et al. (2009) model generally agrees well with calculations of L_{bol} for individual objects. Such strong agreement for two completely independent ways of calculating bolometric luminosities implies that the observed reddening of the central point source is dominated by absorption processes occurring within the circumnuclear region.

Individual-source bolometric luminosities for each of the four methods are presented in Table 2. Note that, compared to L_{bol} (method 1), $L_{bol,X}$ (method 2) underestimates the bolometric luminosity and $L_{\text{tot,obs}}$ (method 3) overestimates it. Both $L_{bol,X}$ and

$L_{bol,\text{T09}}$ (method 4) distributions have more scatter, which suggests the point-source fitting method (method 1) may be superior. We use this value, L_{bol}, in the subsequent analysis.

Figure 3.7 shows the distribution of L_{bol} with redshift, as well as the ratio of L_{bol} to the observed L_X. We detect no trend in L_{bol} with redshift, but the objects with lower L_X appear to have a higher scatter in L_{bol} compared to objects with higher L_X. Interestingly, values of L_{bol} calculated using point-source luminosities in only 1 or 2 optical bands, while individually more uncertain than values calculated with 3 or 4 bands of optical point-source data, are not outliers in the overall distribution of L_{bol}. This suggests that a sample of AGN with L_{bol} calculated as in section 3.4.2, but with only one optical band used to determine $E(B-V)$, may be reliable as a sample even if the individual values have high uncertainty.

3.4.4 Dust-to-Gas Ratios

Our point-source fitting method produces estimates of $E(B-V)$ from optical point-source dust reddening. We also have gas column density (N_H) measurements from X-ray spectral slope fitting. These two quantities allow for an independent measurement of the intrinsic dust-to-gas ratio in AGN. Figure 3.8 shows the measures of dust vs. gas in the form of $E(B-V)$ vs. N_H. Binning the data in Figure 3.8 over four N_H ranges shows no strong trend; however, a Kolmogorov-Smirov (K-S) test indicates only a 0.4% chance that the subsample of $E(B-V)$ values for objects with $N_H < 10^{22}$ cm^{-2} is drawn from the same parent sample as the subsample of $E(B-V)$ values for objects with $N_H > 10^{22}$ cm^{-2}. This indicates that dust and gas obscuration may be weakly correlated, so that sources with higher N_H tend toward higher $E(B-V)$ values, but with large scatter. The dust-to-gas ratios span a relatively wide range, including dust-to-gas ratios similar to the Galactic value, $E(B-V)/N_H = 1.7 \times 10^{-22}$ cm^2/H

(see Draine 2003; Shull & van Steenberg 1985), and those closer to that in the SMC, $E\left(B-V\right)/N_H = 2.2 \times 10^{-23}$ cm^2/H (Martin et al. 1989).

The SMC-like dust ratios are consistent with observations of local Seyferts, based on their star formation histories and intrinsic metallicities (Maiolino et al. 2001; Willott et al. 2004; Hopkins et al. 2004). However, as discussed in Willott et al. (2004), the similarity of these dust-to-gas ratios is likely a coincidence, due to the drastically different physical conditions between AGN and the SMC. Maiolino et al. (2001, 1997) discuss at least three causes for the much higher gas-to-dust ratio relative to the Milky Way: (1) a difference in dust grain composition and size such that UV absorption is less effective; (2) the ratio of dust to gas is simply lower than in our galaxy; and (3) an effect of the majority of X-ray absorption occurring very close to the ionizing radiation and within the dust sublimation radius (defined at roughly 1500 K, and on the order of $R_{sub} = 0.1 - 1$ pc). The work of Elitzur & Shlosman (2006) supports this last explanation.

The majority (90%) of our sample lack detected broad emission lines, which within the AGN unification paradigm is commonly interpreted as the result of an optically thick line-of-sight to the broad-line region (also within the dust sublimation radius; Hönig et al. 2006). This, combined with the high obscuration for much of our sample, suggests most of the gas and dust along the line of sight lies within the X-ray dissociation region.

3.5 Eddington Ratios

The use of hard X-ray luminosity to select a complete sample of AGN is vital to studies of AGN accretion properties. Approximately 90% of our sources would fail to be included in samples selected by optical spectroscopy. Additionally, the use of *HST* data allows for black hole mass estimates that are independent of AGN properties. Most AGN

host galaxies are unresolved in black hole surveys selected by broad $H\beta$ (Kollmeier et al. 2006; Vestergaard & Peterson 2006; Bentz et al. 2006), [O III] (Netzer et al. 2007a) or CIV emission lines (Vestergaard 2002; Kaspi et al. 2005). Conversely, most of the optical spectra in narrow-line AGN (Barger et al. 2003; Cowie et al. 2003; Szokoly et al. 2004) are good enough for redshifts, but lack the signal-to-noise for a measurement of $M_\bullet$ (*e.g.*, Heckman et al. 2004). Our X-ray selection criteria, combined with not being dependent on line widths for $M_\bullet$ estimates, allows us to examine AGN that are not individually contributing strongly to the accretion history of AGN, but that are a significant fraction of the X-ray luminosity function (and hence total black hole accretion) at intermediate redshifts.

Figure 3.9 shows the comparison between the black hole mass (Section 3.3) and bolometric luminosity (Section 3.4.2). The mean and median Eddington ratios for our sample are $\langle L_{bol}/L_{Edd} \rangle = 0.009$ and 0.006, respectively (where $L_{Edd} \equiv 1.3 \times 10^{38}(M_\bullet/M_\odot)$ erg s^{-1}), meaning the majority of the sample consists of AGN with highly sub-Eddington accretion rates. Only one-third of the sample has $L_{bol}/L_{Edd} > 0.01$. This result – a typically low Eddington ratio within a sample that spans a wide range of values – is similar to results for local Seyfert galaxies (*e.g.*, Cardamone et al. 2007; Mushotzky et al. 2008).

The scarcity of AGN with high accretion rates is at least partly to be expected from our selection criteria. By excluding AGN with low host-to-point source luminosity ratios, we preferentially exclude high-Eddington-ratio black holes for all but the smallest SMBH. Our selection process (§3.2.1) rejects 34 AGN+hosts in total, of which 16 are too faint to accurately recover bulge luminosities. Given their low fluxes, those 16 objects are unlikely to be bright, near-Eddington accreting AGN. The other 18 rejected objects are point-like in the optical images, which could possibly be due to bright (near-Eddington-accreting) nuclei. However, even if those objects were included, they would

constitute a minority of the total sample, indicating that our sample of sub-Eddington AGN represents the dominant AGN population within the GOODS fields at $z < 1.25$.

The result that more than 90% of our sample is accreting at less than 10% of the Eddington limit is robust to possible sources of error in our analysis. If we were to assume that our sources are accreting at the Eddington limit and use that assumption to calculate SMBH masses, our masses would decrease by more than two orders of magnitude, on average. Such a large deviation is inconsistent both with independent observations of black hole masses and bulges from $0 \lesssim z \lesssim 3$ (*e.g.*, Woo et al. 2008; Jahnke et al. 2009; Merloni et al. 2010) and with constraints on the maximum evolution of the black hole-bulge relation from studies that *do* assume Eddington-limited accretion (Borys et al. 2005; Bluck et al. 2011). Our results are also inconsistent with scenarios in which most SMBHs cycle between a fully quiescent state and a near-Eddington accretion state (*e.g.*, King 2010). Even assuming the largest possible deviation in black hole masses based on the maximum evolution of the bulge-black hole relation, our AGN are still in a phase of very slow growth.

The Eddington ratios are presented in Figure 3.10 in relation to $M_\bullet$ and redshift. To determine whether we see any significant evolution of Eddington ratios (as others have; *e.g.,* Netzer & Trakhtenbrot 2007; Greene & Ho 2007), we consider the relevant selection biases. In Figure 3.10, we plot the hard X-ray luminosity limit ($L_X > 3 \times 10^{42}$ erg s^{-1}, dashed line) of our sample, which excludes low Eddington ratio, low mass AGN. At the same time, high-luminosity AGN are sufficiently rare that they do not appear in pencil-beam surveys such as GOODS; we show this by plotting in Figure 3.10 the luminosity at which we expect to detect only 1 AGN within the GOODS volume (which is a function of redshift) from the quasar luminosity function (Croom et al. 2004). After accounting for these selection effects, we detect no correlation between Eddington ratio and either black hole mass or redshift. This lack of real trend is consistent with Woo

& Urry (2002), who found that selection effects can create the appearance of correlations where none intrinsically exist.

Our values of L_{bol}/L_{Edd} are somewhat lower than those reported by others (Kollmeier et al. 2006; Greene & Ho 2007; Netzer et al. 2007b). Direct comparison between different studies is complicated, however, due to the varying selection criteria, redshifts and flux limits of each study. For example, restricting a comparison to the objects in their paper with redshifts similar to ours, Kollmeier et al. (2006) find that the broad-line AGN from the AGES survey (Kochanek et al. 2004) radiate at near-Eddington rates, $0.1 < \lambda < 1.0$. But their study has considerably brighter flux limits than our own, with AGES being 50% complete at $R = 21.5$, whereas our sample is nearly complete down to $z_{850} = 24.0$ under the constraints outlined in Sections 3.2.1 and 3.2.2. Direct comparison to the large, optically-selected SDSS quasar sample (Schneider et al. 2007) is also difficult owing to that sample being highly incomplete at low Eddington ratios (Kelly et al. 2010). Samples with similar selection criteria and flux limits (Bundy et al. 2008), and those with overlapping samples from the same survey (Ballo et al. 2007), report Eddington ratios more similar to ours.

Interestingly, many of the aforementioned black hole samples at different redshifts and with different selection criteria do not appear to have radically different accretion rates. Greene & Ho (2007) show that a sample of broad-line AGN selected from the SDSS have a peak black hole mass of $10^7 M_\odot$ at $z < 0.3$, with a typical Eddington rate of 10%, or a typical accretion rate of $2 \times 10^{-3}/\epsilon \ M_\odot \ \mathrm{yr}^{-1}$, where ϵ is the efficiency of converting mass to light. Most AGN in our sample have similar accretion rates (to within 40%), despite having higher masses and lower Eddington rates. Our accretion rates are consistent with those of Ballo et al. (2007) sample, which overlaps ours somewhat, even though they calculate $M_\bullet$ and L_{bol} differently. Type 1 AGN from the zCOSMOS sample (Merloni et al. 2010), which probes higher redshifts and luminosities than our GOODS

sample, are accreting at rate higher than ours by only a factor of ~ 4. And Hickox et al. (2009), who probe a slightly lower-mass part of the black-hole mass function at similar redshifts, find that black holes in AGN are accreting at a rate within a factor of 2 of ours. These different samples of AGN span a wide range of redshifts, luminosities, and black hole masses, yet they have similar estimates of accretion rates in $M_\odot$ yr^{-1}, assuming the same radiative efficiency. This suggests that the accretion rates of AGN may be more directly related to the supply of material from the circumnuclear region than the properties of the central black hole.

If we follow Elvis et al. (2002) and assume a minimum radiative efficiency of $\epsilon = 0.15$, our median black hole with an Eddington ratio of 0.006 and mass of $5.1 \times 10^8 M_\odot$ is accreting at $\dot{M} \sim 0.05\ M_\odot$ yr^{-1}. This accretion rate is too low to have been the typical rate for the duration of the AGN activity cycle: given our median redshift, it would take a seed black hole a minimum of $\sim 150\%$ of the age of the universe to that point to have grown to its present size, assuming growth from the largest initial mass of direct-collapse black holes (Volonteri et al. 2008), $\sim 10^6\ M_\odot$. Given that the seed mass is likely to have been lower, and that this accretion rate is super-Eddington for $M_\bullet \lesssim 3 \times 10^6\ M_\odot$, the actual time would likely be far higher. For any reasonable assumptions, therefore, the accretion rate of a typical black hole in our sample must have been significantly higher at some point in the past in order for it to grow to its present size within a Hubble time. Assuming a larger radiative efficiency, which Elvis et al. suggest is possible, only strengthens this conclusion.

This is unsurprising given that black hole growth scenarios involving a period of rapid (Eddington-limited) growth followed by a power-law-decay growth rate (*e.g.*, Hopkins et al. 2006a; Yu & Lu 2008) are more consistent with observations of Eddington ratio distributions in a complete sample than constant-growth or "light bulb" scenarios (Hopkins & Hernquist 2009). Under the specific timescales for a self-regulating feed-

back model described in Hopkins & Hernquist (2009), we calculate that a black hole with our median observed redshift ($z = 0.94$) and Eddington ratio has an accretion rate that peaks at $z \approx 1.1$, assuming a single episode of growth. Such an object would easily be detected above our flux limits. The progenitor to our median AGN should therefore be detected within our sample at its peak growth stage (*i.e.*, accreting at a high Eddington ratio). Extending these calculations to each individual object in our sample, we should detect ≈ 60 progenitor AGN accreting at the Eddington limit (within our limiting redshift, $z < 1.25$).

In fact, we detect only 7 possible candidates: 3 sources consistent with $L_{bol}/L_{Edd} = 1$ within our 1σ uncertainties and 4 sources for which the detected L_{bol}/L_{Edd} is a lower limit. The number of Eddington-limited AGN in our sample is too low by at least an order of magnitude to be consistent with the predictions of the Hopkins & Hernquist model. We also considered the possibility that the progenitors of the slow-growing AGN within our limiting redshift ($z < 1.25$) were removed from our sample due to their bright nuclei rendering them point-like in the optical images (§3.2.1). However, not only are there not enough of those objects (18) to account for the predictions of the model, but the redshift distribution of the excluded point-like AGN is actually *lower* than that of the objects within our sample (median $z = 0.84$ vs. 0.94 in the included sample). If these objects were progenitors to our slow-growing AGN, their redshifts would necessarily be higher. Comparing the redshift distribution of expected progenitors from our Monte Carlo simulations to the sample of excluded AGN, we find the same result. We therefore argue that the timescales of the single-episode model in Hopkins & Hernquist (2009) do not describe the accretion history of our AGN. A significant fraction of our observed slow-growing black holes must have had a peak growth epoch beyond our maximum redshift.

Overall, most of the X-ray selected AGN constituting our sample are best described

as being AGN with high black hole masses and with low accretion rates, in a slow-growth phase. In order to grow to the sizes we observe, the typical source in our sample must have had a significantly higher accretion rate at some point well before $z \sim 1$. Although a preponderance of slowly growing AGN is qualitatively consistent with self-regulating feedback models in which AGN spend most of their time at low accretion rates, our result is inconsistent with quantitative timescales predicted by common parameterizations of this model. The growth history of black holes is clearly more complex than that described by a single simple model, a conclusion echoed by other studies examining AGN at a variety of different redshifts and luminosities (Kauffmann & Heckman 2009; Merloni et al. 2010; Cardamone et al. 2010; Steinhardt & Elvis 2011).

3.6 Conclusions

We studied 87 AGN with $z < 1.25$ from the GOODS survey to understand the fundamental properties of moderate-luminosity obscured AGN that make up most of the X-ray background and thus a large fraction of black hole growth. Most of these AGN would not be selected via broad emission line surveys or blue color excesses, *i.e.*, the highest-L and L/L_{edd} objects are excluded. However, this sample represents the bulk of AGN emission at $z \lesssim 1.25$.

After morphological fits to separate AGN/host galaxy light and determine bulge-to-total ratios, we estimated black hole masses for each AGN using the $M_\bullet - L_B$ relation of Marconi & Hunt (2003) as reformulated by Ferrarese & Ford (2005). We do not assume this relation evolves with redshift, but use a Monte Carlo error analysis to account for uncertainty in the time evolution of Equation 3.1 as well as other parameter uncertainties. The resulting uncertainties in our black hole masses are typically on the order of 0.5 dex.

Using an unobscured AGN template calculated from broad-line AGN in the GOODS fields, we calculated bolometric luminosities individually for each object by reddening the normalized template SED to match nuclear point-source colors and using the fitted $E(B-V)$ to calculate the energy re-radiated in the far-infrared by dust surrounding the AGN. This method is consistent with single-prescription empirical bolometric correction methods and with independent theoretical models, but has less scatter.

The SED fitting of the nuclear point sources gives the added benefit of an estimate of dust absorption upon the AGN template. Assuming a standard Galactic reddening curve, we find that 70% of the AGN have dust-to-gas ratios similar to local Seyferts (Maiolino et al. 2001). The host galaxy contribution to the nuclear line-of-sight obscuration in the GOODS AGN is minimal for most of our sources.

Our survey reveals a considerable fraction of low-Eddington-accreting, high-black-hole-mass AGN in normal host galaxies. The mean Eddington ratio for our sample is $L/L_{Edd} \sim 0.009^{+0.046}_{-0.005}$, considerably lower than in broad-line AGN surveys such as SDSS (Netzer et al. 2007a; Greene & Ho 2007). Many of these AGN have properties consistent with local Seyfert AGN (Mushotzky et al. 2008). Even considering the small uncertainties in the Eddington ratio, which reflect the current uncertainty in the time evolution of the bulge-black hole mass relation, our typical source is still accreting at well below the Eddington limit.

The observed Eddington ratios of our sources are low, but their black hole masses are high, meaning they must have been accreting at significantly higher rates at some point during their growth history in order for them to have reached their observed masses within a Hubble time. According to self-regulating feedback accretion models for black hole growth, our black holes could be the slow-growth phase of their AGN lifetimes; comparison with accretion timescales from simple models of self-regulated feedback indicate that our AGN sample may have a complex accretion history. A significant

fraction of our sample must have been accreting at near-Eddington rates before $z \sim 1$. Such a complex growth history is consistent with the downsizing scenario (Barger et al. 2005; Hasinger et al. 2005).

The use of the point-source luminosity as leverage to extract the multi-wavelength AGN SED from a combined AGN plus host galaxy source is a promising technique. In particular, the high-resolution infrared data promised by *JWST* could be used to significantly increase the accuracy of the central reddening determination, which would decrease uncertainty about the re-radiated dust luminosity in the FIR range. This technique may also benefit from the separation of AGN and host galaxies at IR wavelengths using WFC3 (Schawinski et al. 2011). Although the efficacy of host-point-source separation has not yet been studied in as much depth using WFC3 data as it has for ACS, the addition of several data points to the low-resolution point-source SED would be very valuable.

physical Observatory for and on behalf of NASA under contract NAS8-03060.
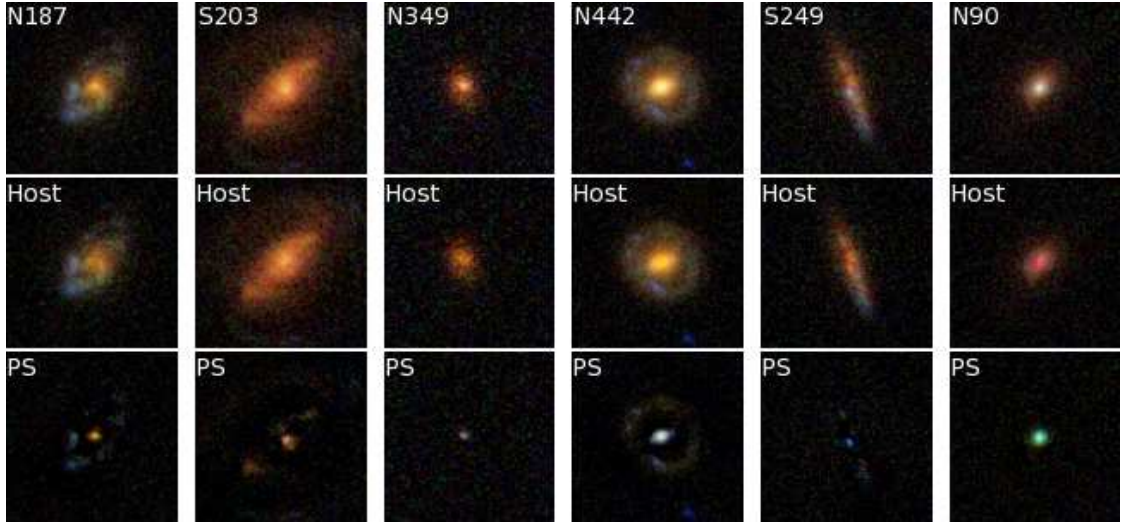
Fig. 3.2.— $BVIz$ composite images of six of the sources in our sample. Each source, marked with its ID from Alexander et al. (2003), is fit in each band with a host galaxy composed of a bulge and disk, and a central point-source. For each source, the image marked "Host" shows the point-source-subtracted galaxy. The image marked "PS" shows the residuals when the smooth host galaxy fit is subtracted, leaving behind the central nucleus and extended detailed features of the host galaxy. Hosts and point sources vary in color and luminosity. (SEDs of these sources are shown in Figure 3.5.)
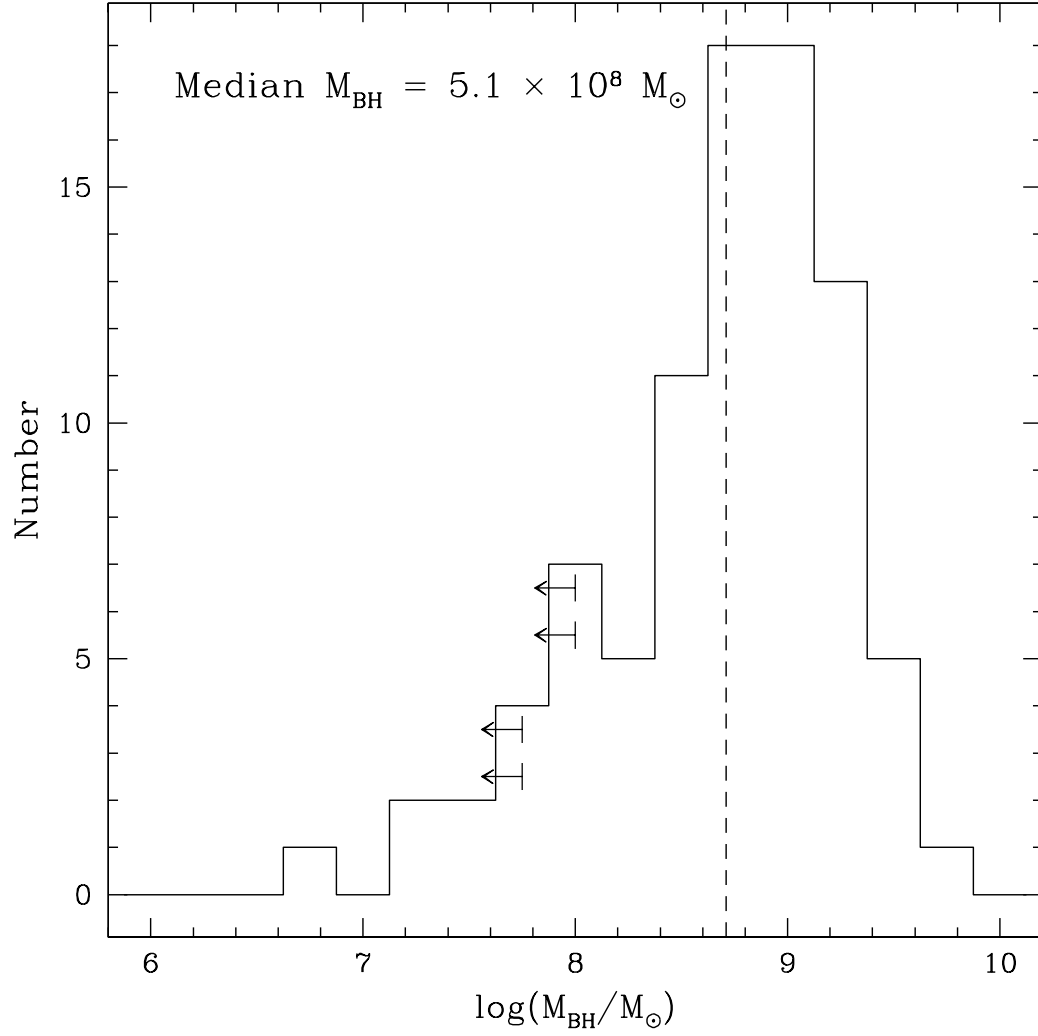
Fig. 3.3.— Histogram of estimated black hole masses, using bulge luminosities from morphological fitting and Equation 3.1, adapted from Marconi & Hunt (2003). The dashed line shows the median value of $M_\bullet = 5.1 \times 10^8 M_\odot$. Arrows indicate the four sources with upper limits to the black hole mass.
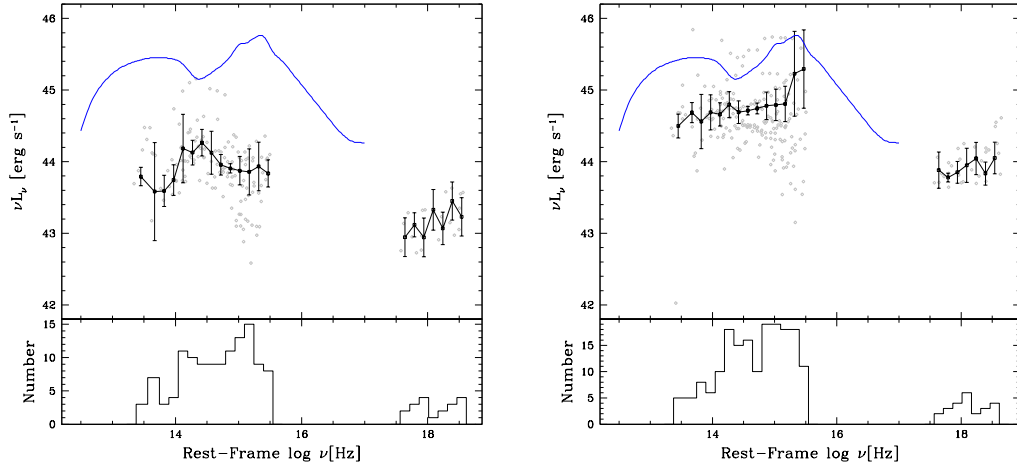
Fig. 3.4.— Weighted average SEDs of broad-line AGN in the GOODS fields (filled circles). The left panel shows 32 low-luminosity ($43.0 < \log L_X < 44.0$) AGN, and the right panel shows 26 moderate-luminosity ($44.0 < \log L_X < 44.9$) AGN. The bottom histogram in each panel shows the number of AGN contributing to the median, as a function of frequency. For comparison, the average spectrum of more luminous SDSS quasars ($L_X > 10^{45}$ erg s^{-1}; Richards et al. 2006) is shown as a blue line. Our SEDs are very roughly consistent with the Richards et al. spectrum when normalized at ~ 1 keV, but the "big blue bump" feature at $\sim 2500 \overset{\circ}{A}$ is significantly weaker in lower luminosity AGN. Note that some lower-luminosity objects used to make the composite SED in the left panel show signs of a K-giant stellar population in their SEDs.
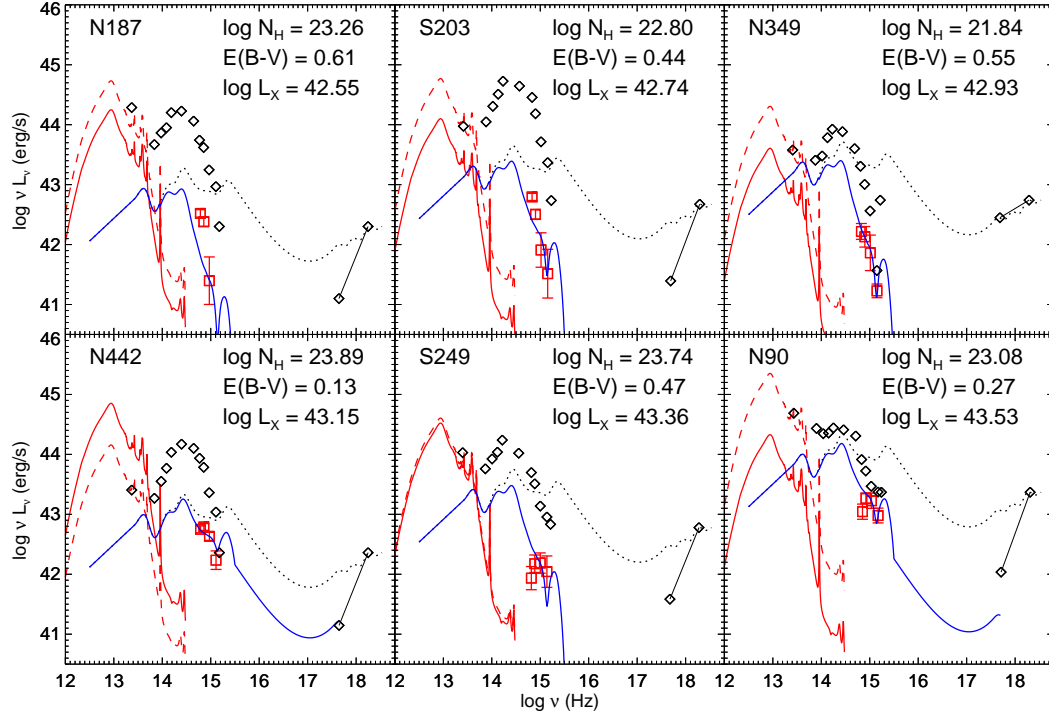
Fig. 3.5.— Broad-band SEDs of AGN plus host galaxy (*open diamonds*) and point source alone (*red squares*). The mean AGN SED, calculated from broad-line AGN within the GOODS fields, is shown as a *dotted line*, normalized to the AGN hard X-ray luminosity. This template was reddened and fit through the extracted point source values, resulting in the *blue solid curve*. The far-IR dust curve (*solid red line*) is calculated from the derived $E(B - V)$ according to Draine & Li (2007). Shown for comparison is the same emissivity normalized to the maximum L_{MIR} from broad-band flux (*dashed red line*). In most cases, the calculated (solid) curve lies under the maximum (dashed) curve, *i.e.,* the calculated infrared luminosities do not exceed the observed luminosities. In the rare event that the solid line exceeds the observed infrared flux (N442), it is usually by a small factor ($\times 2$), commensurate with AGN variability on year-long timescales (Sarajedini et al. 2006). (Images of these sources are shown in Figure 3.2.)
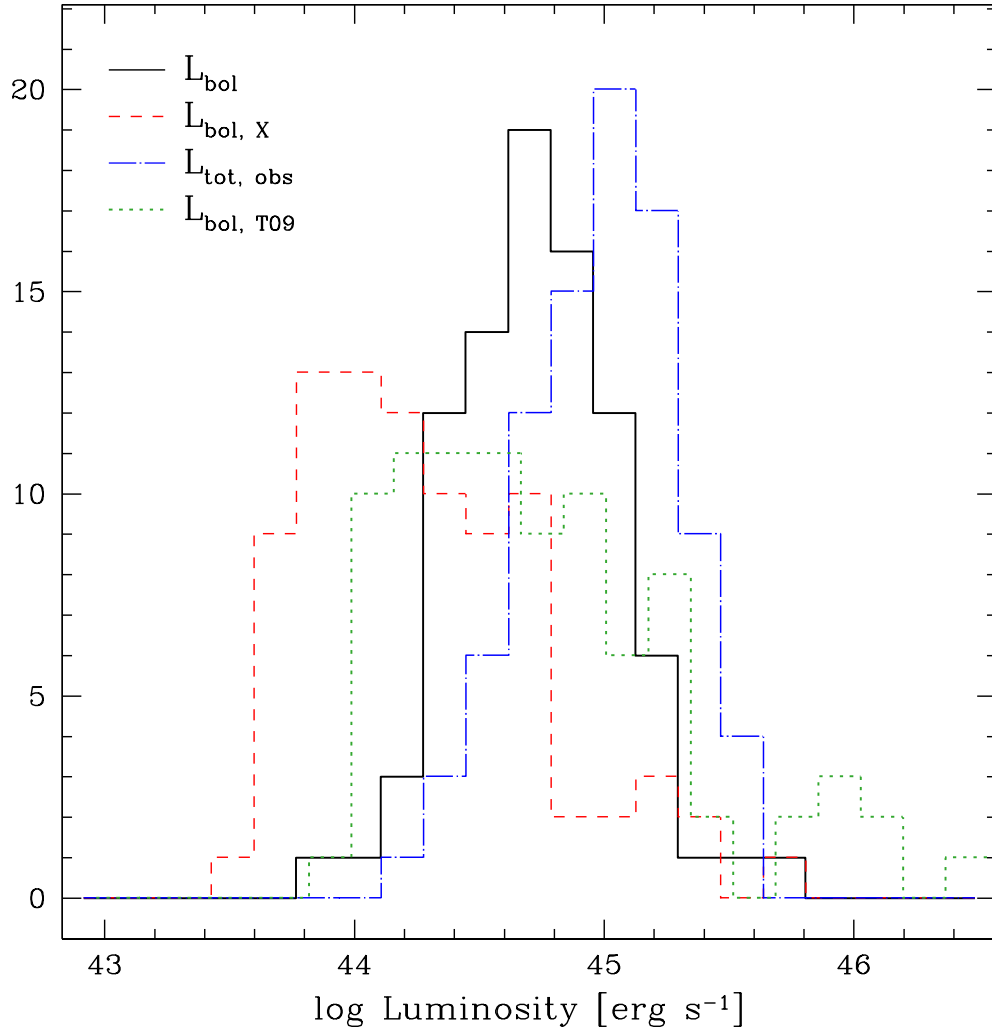
Fig. 3.6.— Histograms of bolometric luminosities calculated four ways: (1) using our SED-reddening fit method from Section 3.4.2, L_{bol} (black solid line); (2) using our empirical bolometric correction to the X-ray luminosity, $L_{bol,X}$ (red, dashed line); (3) using a simple sum of all the observed light for each source, $L_{tot,obs}$ (blue, dot-dashed line); and (4) using the model-based, luminosity-dependent correction of Treister et al. (2009), $L_{bol,T09}$ (green, dotted line). The first method has the smallest scatter and agrees well with the successful population synthesis model of Treister et al.; the second method underestimates the luminosity, probably because a significant fraction of the X-rays are absorbed; and the third method overestimates L_{bol} because of a significant contribution from the host galaxy. A Kolmogorov-Smirnov (K-S) test indicates a 6.3% chance that the distributions of L_{bol} and $L_{bol,T09}$ are from the same parent distribution, whereas there is less than a 0.001% chance that the L_{bol} distribution is consistent with either the $L_{bol,X}$ or $L_{tot,obs}$ distributions.
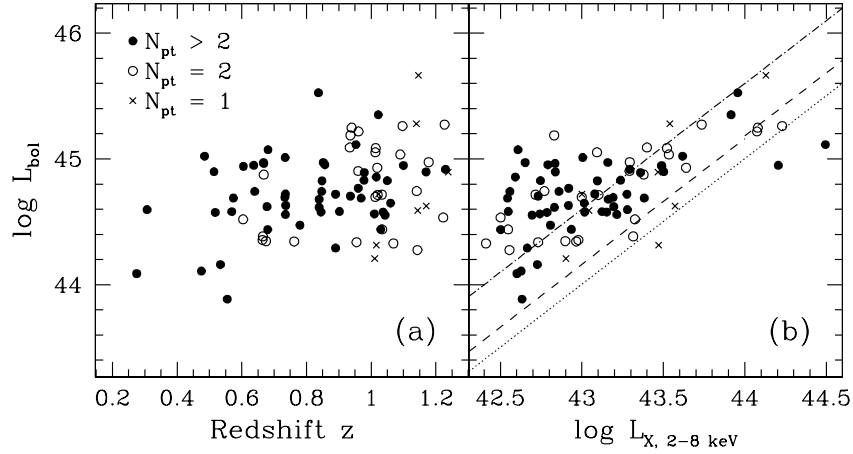
Fig. 3.7.— Calculated bolometric luminosities and comparison of methods. Panels show: (a) Bolometric luminosity (L_{bol}), as described in Section 3.4.2 (method 1 in Figure 3.6), versus redshift. Solid points indicate objects with nuclear point source detections in at least 3 optical bands ($N_{pt} > 2$); open circles show sources with $N_{pt} = 2$; crosses show sources with $N_{pt} = 1$, which have highly uncertain values of $E(B - V)$ and thus L_{bol}. We detect no trend in L_{bol} with redshift. (b) Bolometric luminosity versus absorption-corrected hard X-ray luminosity. Fixed bolometric corrections of $L_{bol} = 10 \times L_X$ (dotted line; Elvis et al. 1994) or $L_{bol} \approx 15 \times L_X$ (dashed line; Section 3.4.1) underestimate L_{bol}. The peak of the L_{bol}/L_X distribution ($(L_{bol}/L_X)_{\mathrm{peak}} = 39.5$) is shown as a dot-dashed line and is likely higher than corrections based on unobscured AGN because of significant X-ray absorption in this sample.
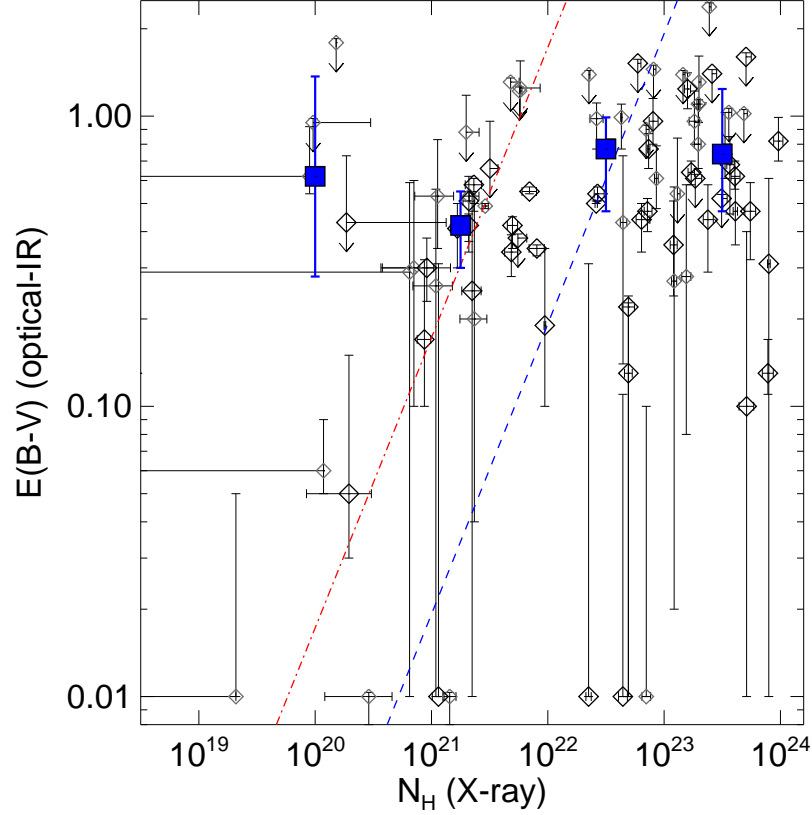
Fig. 3.8.— $E(B-V)$ derived from dust reddened model SED fits vs. X-ray-determined gas column density. Larger diamonds indicate $E(B-V)$ calculated using at least 3 ACS filters; smaller points indicate that the $E(B-V)$ calculation used only one or 2 filters. Average values for four N_H bins (*blue squares*) show no strong trend: intrinsically obscured AGN ($N_H > 10^{22}$ cm^{-2}) tend towards larger reddening coefficients, but not universally. The ratios span a wide range, from approximately that of the SMC (*red dot-dash*, $E(B-V)/N_H = 2.2 \times 10^{-23}$ cm^2/H) to ratios in excess of Galactic (*blue dashed*, $E(B-V)/N_H = 1.7 \times 10^{-22}$ cm^2/H).
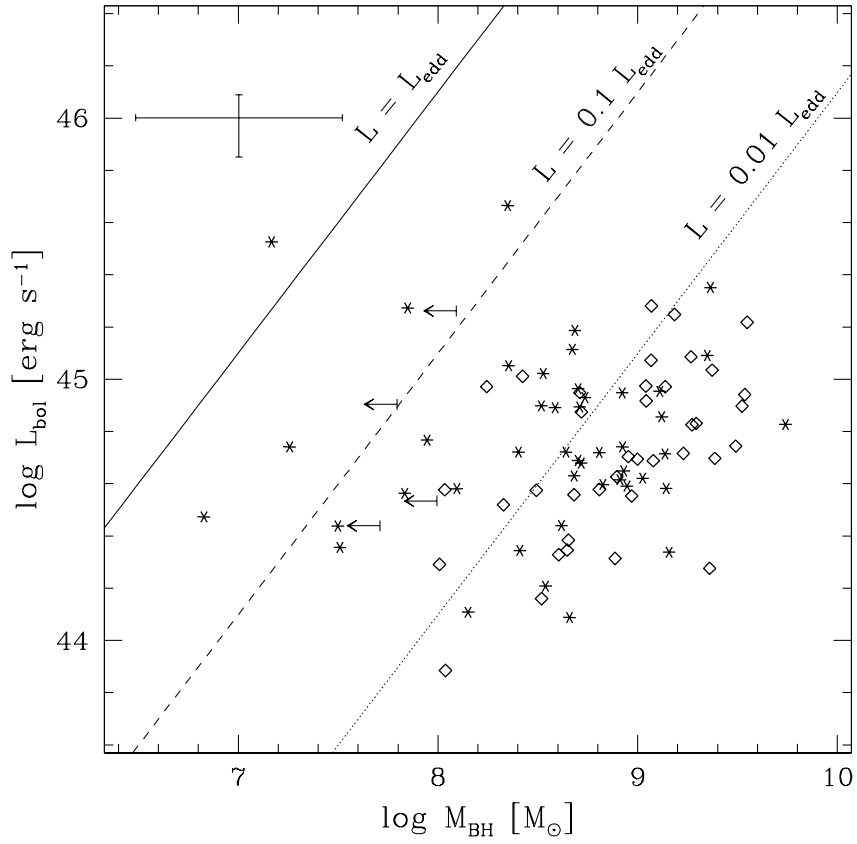
Fig. 3.9.— Bolometric AGN luminosity vs. black hole mass. Bulge-dominated (*diamonds*) and disk-dominated systems (*stars*) have overlapping distributions, although most of the lowest-mass black holes are in disk-dominated systems. Typical errors are indicated at the upper left. Lines show 100%, 10%, and 1% of the Eddington ratio; the mean and median Eddington ratios for our sample are $L = 0.009 \times L_{Edd}$ and $L = 0.006 \times L_{Edd}$, respectively.
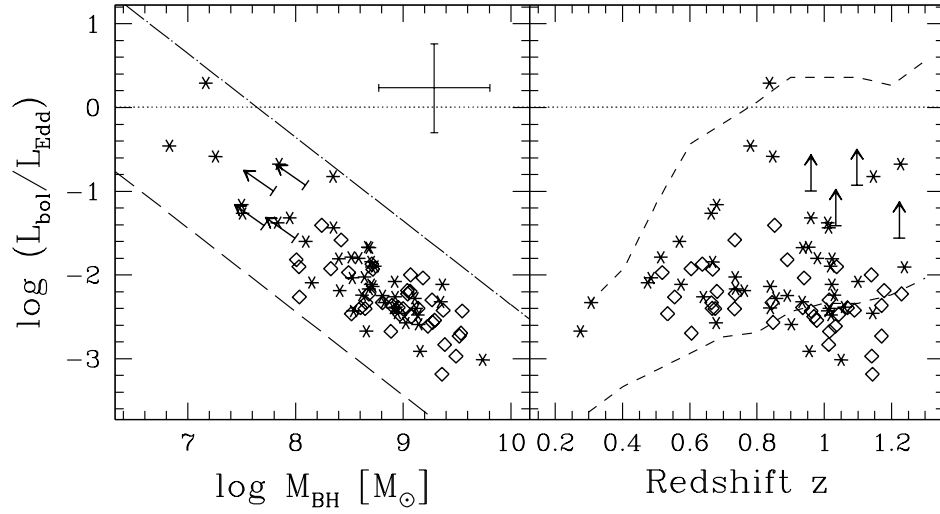
Fig. 3.10.— Eddington ratio vs. black hole mass (*left*) and redshift (*right*). Symbols indicate bulge-like (*diamonds*) and disk-like (*stars*) host galaxy morphologies. The dashed line in the left panel indicates the lower L_X selection criteria of 3×10^{42} erg s^{-1}, and the dot-dashed line indicates the upper luminosity limit for a single-source detection based on the Croom et al. (2004) quasar luminosity function calculated for the GOODS area. The dashed lines on the right indicate the maximum and minimum luminosities of X-ray sources detected in the GOODS parent sample at each redshift, assuming $\log M_{\bullet} = 7.0 M_{\odot}$. In both panels, the observations more or less fill the allowed area.

Table 3.1:: GOODS AGN sample with point source and host

galaxy deconvolution for objects between $0.2 < z < 1.25$.

	Optical Position			Rest-frame B (AB mag)				
ID[a]	RA	DEC	z	Total	Pt src	Host	B/Tot	$\log M_{BH}$ (M$_\odot$)
N 48	188.983765	62.205441	0.940	21.741±0.012	$\cdots$	21.74±0.01	$0.79^{+0.17}_{-0.30}$	$9.18^{+0.52}_{-0.51}$
N 72	189.023956	62.167603	0.936	22.020±0.007	23.40±0.19	22.38±0.23	$0.48^{+0.28}_{-0.26}$	$8.69^{+0.51}_{-0.50}$
N 76	189.027634	62.164326	0.637	21.389±0.010	26.79±0.39	21.40±0.21	$0.53^{+0.27}_{-0.27}$	$8.71^{+0.50}_{-0.50}$
N 82	189.033875	62.176731	0.681	20.990±0.004	22.90±0.24	21.19±0.24	$0.82^{+0.15}_{-0.30}$	$9.07^{+0.52}_{-0.52}$
N 90	189.046814	62.150940	1.140	22.340±0.013	24.48±0.14	22.50±0.20	$0.77^{+0.18}_{-0.29}$	$9.07^{+0.52}_{-0.52}$
N 93	189.050156	62.194221	0.275	19.784±0.001	23.08±0.21	19.84±0.23	$0.83^{+0.14}_{-0.30}$	$8.66^{+0.50}_{-0.50}$
N103	189.060364	62.121876	0.969	21.194±0.012	24.86±0.15	21.30±0.18	$0.39^{+0.29}_{-0.23}$	$9.08^{+0.52}_{-0.52}$
N110	189.070221	62.104027	1.141	21.479±0.008	26.23±0.26	21.48±0.19	$0.76^{+0.19}_{-0.29}$	$9.49^{+0.55}_{-0.55}$
N113	189.071228	62.169903	0.845	22.451±0.011	25.24±0.17	22.45±0.17	$0.87^{+0.12}_{-0.30}$	$8.81^{+0.50}_{-0.51}$
N116[b]	189.077530	62.187622	1.022	20.554±0.006	22.53±0.29	20.55±0.26	$0.32^{+0.33}_{-0.21}$	$9.36^{+0.54}_{-0.54}$

Table 3.1 – Continued

ID[a]	RA	DEC	z	Total	Pt src	Host	B/Tot	$\log M_{BH}$ (M$_\odot$)
N127	189.088516	62.185921	1.014	21.881±0.011	26.22±0.26	21.88±0.19	$0.89^{+0.10}_{-0.30}$	$9.27^{+0.53}_{-0.53}$
N139	189.098541	62.310368	1.013	21.411±0.014	24.67±0.14	21.41±0.19	$0.75^{+0.19}_{-0.30}$	$9.39^{+0.54}_{-0.54}$
N150	189.114609	62.174030	0.762	23.115±0.023	26.69±0.38	23.11±0.19	$0.86^{+0.12}_{-0.30}$	$8.41^{+0.50}_{-0.49}$
N158	189.121506	62.179565	1.013	21.957±0.018	27.88±0.76	21.96±0.17	$0.13^{+0.30}_{-0.07}$	$8.35^{+0.49}_{-0.50}$
N160	189.122055	62.270576	0.848	21.464±0.005	24.00±0.14	21.46±0.22	$0.95^{+0.05}_{-0.30}$	$9.27^{+0.53}_{-0.53}$
N163	189.124893	62.095203	0.485	21.389±0.005	23.81±0.16	21.39±0.22	$0.69^{+0.22}_{-0.29}$	$8.53^{+0.50}_{-0.50}$
N164	189.125244	62.156734	0.953	22.425±0.009	25.23±0.16	22.42±0.17	$0.46^{+0.28}_{-0.26}$	$8.67^{+0.50}_{-0.50}$
N170	189.132751	62.295914	0.680	21.829±0.008	26.15±0.24	21.85±0.19	$0.05^{+0.22}_{-0.03}$	$7.50^{+0.52}_{-0.53}$
N174	189.138474	62.143036	0.934	21.084±0.005	22.52±0.30	21.42±0.26	$0.86^{+0.12}_{-0.30}$	$9.35^{+0.54}_{-0.54}$
N177	189.140244	62.168388	1.016	21.336±0.008	26.40±0.30	21.35±0.19	$0.39^{+0.29}_{-0.24}$	$9.12^{+0.52}_{-0.52}$
N187	189.145264	62.274620	0.847	22.444±0.015	25.77±0.19	22.50±0.18	$0.03^{+0.34}_{-0.03}$	$7.26^{+0.54}_{-0.54}$
N194	189.153198	62.199001	0.555	22.969±0.008	27.24±0.52	22.99±0.19	$0.73^{+0.20}_{-0.29}$	$8.04^{+0.50}_{-0.50}$
N201	189.160385	62.227596	1.020	22.059±0.015	25.84±0.19	22.09±0.18	$0.81^{+0.16}_{-0.30}$	$9.14^{+0.52}_{-0.52}$

Table 3.1 – Continued

ID[a]	RA	DEC	z	Total	Pt src	Host	B/Tot	$\log M_{BH}$ (M$_\odot$)
N205	189.162918	62.162346	1.230	22.998±0.017	26.16±0.27	23.06±0.19	$1.00^{+0.00}_{-0.30}$	$9.04^{+0.51}_{-0.51}$
N217	189.173203	62.163483	0.518	21.497±0.005	28.74±1.08	21.50±0.17	$0.60^{+0.30}_{-0.35}$	$8.49^{+0.50}_{-0.50}$
N222	189.175827	62.262722	0.857	21.380±0.008	24.00±0.14	21.48±0.22	$0.66^{+0.24}_{-0.32}$	$9.11^{+0.52}_{-0.52}$
N240	189.193115	62.234734	0.961	20.867±0.005	22.85±0.24	21.06±0.24	$0.89^{+0.10}_{-0.30}$	$9.55^{+0.56}_{-0.55}$
N242	189.194107	62.149166	0.890	23.861±0.041	28.37±0.93	23.88±0.16	$0.49^{+0.30}_{-0.28}$	$8.01^{+0.50}_{-0.50}$
N261	189.209030	62.204823	0.902	21.971±0.010	26.91±0.43	21.98±0.20	$1.00^{+0.00}_{-0.30}$	$9.14^{+0.52}_{-0.52}$
N262	189.209595	62.334686	1.011	22.566±0.010	23.97±0.14	22.92±0.22	$0.47^{+0.28}_{-0.26}$	$8.54^{+0.50}_{-0.50}$
N266	189.213638	62.181107	1.100	22.975±0.017	25.89±0.19	23.05±0.18	$1.00^{+0.00}_{-0.30}$	$8.92^{+0.51}_{-0.51}$
N278	189.222992	62.338577	1.023	23.166±0.013	24.76±0.15	23.45±0.19	$0.56^{+0.27}_{-0.28}$	$8.40^{+0.49}_{-0.50}$
N286	189.231064	62.219883	0.955	21.626±0.008	24.52±0.14	21.70±0.19	$0.69^{+0.22}_{-0.29}$	$9.16^{+0.52}_{-0.52}$
N304	189.245163	62.243118	0.678	20.765±0.005	23.38±0.19	20.87±0.23	$0.56^{+0.26}_{-0.28}$	$9.02^{+0.52}_{-0.51}$
N309	189.249268	62.326241	1.144	22.582±0.017	24.92±0.14	22.72±0.18	$0.71^{+0.21}_{-0.30}$	$8.95^{+0.51}_{-0.51}$
N323[b]	189.261353	62.262199	0.514	20.393±0.002	21.72±0.41	20.77±0.54	$0.33^{+0.31}_{-0.21}$	$8.52^{+0.54}_{-0.54}$

Table 3.1 – Continued

ID[a]	RA	DEC	z	Total	Pt src	Host	B/Tot	$\log M_{BH}$ (M$_\odot$)
N349	189.281601	62.332314	1.030	23.522±0.027	26.52±0.33	23.59±0.19	$1.00^{+0.00}_{-0.30}$	$8.62^{+0.50}_{-0.50}$
N352	189.282730	62.268341	0.936	20.980±0.006	26.69±0.37	20.99±0.20	$0.24^{+0.30}_{-0.16}$	$8.95^{+0.51}_{-0.51}$
N370	189.300629	62.298428	1.060	22.683±0.014	24.89±0.14	22.84±0.18	$0.92^{+0.08}_{-0.30}$	$8.93^{+0.51}_{-0.51}$
N373	189.307480	62.240242	0.475	22.628±0.006	28.17±0.85	22.63±0.16	$0.99^{+0.00}_{-0.30}$	$8.15^{+0.50}_{-0.50}$
N384	189.316345	62.203796	1.019	21.985±0.018	26.52±0.33	22.00±0.21	$0.31^{+0.30}_{-0.20}$	$8.74^{+0.50}_{-0.50}$
N390	189.319489	62.292667	1.146	22.123±0.008	22.98±0.22	22.78±0.23	$0.20^{+0.32}_{-0.13}$	$8.35^{+0.50}_{-0.50}$
N402	189.334732	62.231556	0.780	23.014±0.232	29.79±0.85	23.02±0.05	$0.02^{+0.20}_{-0.02}$	$6.83^{+0.58}_{-0.58}$
N405	189.340988	62.176670	0.978	21.181±0.006	25.00±0.14	21.18±0.17	$0.55^{+0.26}_{-0.27}$	$9.29^{+0.53}_{-0.53}$
N437	189.393890	62.232430	0.839	20.890±0.006	25.23±0.15	20.91±0.17	$0.27^{+0.30}_{-0.17}$	$8.91^{+0.51}_{-0.51}$
N442	189.402100	62.225620	0.852	22.193±0.009	24.76±0.14	22.30±0.18	$0.21^{+0.30}_{-0.14}$	$8.24^{+0.50}_{-0.50}$
N448	189.408051	62.219257	1.238	22.709±0.016	26.36±0.29	22.75±0.20	$0.36^{+0.29}_{-0.22}$	$8.71^{+0.50}_{-0.50}$
N451[b]	189.413559	62.349976	0.837	20.528±0.006	21.58±0.42	21.05±0.64	$0.01^{+0.19}_{-0.01}$	$7.17^{+0.60}_{-0.63}$
N471	189.462021	62.266979	1.170	21.007±0.006	24.12±0.14	21.07±0.21	$0.52^{+0.27}_{-0.27}$	$9.52^{+0.55}_{-0.55}$

Continued on Next Page...

Table 3.1 – Continued

ID[a]	RA	DEC	z	Total	Pt src	Host	B/Tot	$\log M_{BH}$ ($M_\odot$)
N473[b]	189.469681	62.274593	0.307	19.467±0.001	20.67±0.47	19.90±1.12	$0.99^{+0.01}_{-0.30}$	$8.83^{+0.71}_{-0.68}$
S 44	53.015217	-27.767685	0.574	21.434±0.004	25.56±0.17	21.46±0.18	$0.71^{+0.21}_{-0.29}$	$8.70^{+0.50}_{-0.50}$
S 84	53.050934	-27.772406	1.033	21.866±0.010	25.50±0.17	21.91±0.18	$0.80^{+0.16}_{-0.30}$	$9.23^{+0.53}_{-0.52}$
S 88	53.055191	-27.711349	0.605	19.825±0.002	23.45±0.18	19.86±0.23	$0.90^{+0.09}_{-0.30}$	$9.54^{+0.56}_{-0.55}$
S 91	53.057728	-27.713583	0.735	21.240±0.006	25.68±0.18	21.26±0.18	$0.28^{+0.30}_{-0.18}$	$8.64^{+0.50}_{-0.50}$
S103[b]	53.062420	-27.857510	0.675	20.936±0.005	25.52±0.17	20.95±0.18	$0.27^{+0.30}_{-0.17}$	$8.65^{+0.50}_{-0.50}$
S117	53.071434	-27.717588	0.569	21.742±0.003	23.51±0.18	21.98±0.22	$0.31^{+0.29}_{-0.20}$	$8.09^{+0.50}_{-0.50}$
S118	53.071533	-27.872456	1.097	21.774±0.010	24.89±0.14	21.84±0.18	< 0.054	< 8.09
S134	53.085327	-27.792313	0.604	22.118±0.010	26.08±0.22	22.15±0.18	$0.53^{+0.27}_{-0.27}$	$8.33^{+0.49}_{-0.50}$
S137	53.089264	-27.708660	0.736	21.587±0.007	24.64±0.14	21.65±0.19	$0.44^{+0.28}_{-0.25}$	$8.68^{+0.50}_{-0.50}$
S139	53.091618	-27.782206	0.668	20.893±0.006	24.49±0.14	20.93±0.20	$0.30^{+0.30}_{-0.19}$	$8.70^{+0.50}_{-0.50}$
S151	53.096489	-27.765188	1.223	22.328±0.016	25.25±0.16	22.40±0.17	< 0.055	< 8.00
S155	53.101063	-27.690676	0.534	21.707±0.006	24.98±0.14	21.76±0.17	$0.76^{+0.19}_{-0.30}$	$8.52^{+0.50}_{-0.50}$

Continued on Next Page...

Table 3.1 – Continued

ID[a]	RA	DEC	z	Total	Pt src	Host	B/Tot	$\log M_{BH}$ ($M_\odot$)
S156	53.102264	-27.669563	0.890	22.545±0.011	27.73±0.70	22.55±0.17	$0.84^{+0.13}_{-0.30}$	$8.81^{+0.50}_{-0.50}$
S159	53.103516	-27.933329	1.170	23.112±0.027	26.83±0.40	23.15±0.22	$0.89^{+0.10}_{-0.30}$	$8.90^{+0.51}_{-0.51}$
S160	53.103989	-27.835567	1.037	23.945±0.033	25.94±0.20	24.13±0.28	$0.45^{+0.32}_{-0.27}$	$8.03^{+0.51}_{-0.51}$
S161	53.104088	-27.683752	0.733	21.446±0.005	24.19±0.14	21.54±0.21	$0.81^{+0.16}_{-0.30}$	$9.00^{+0.52}_{-0.51}$
S162	53.104607	-27.845348	1.043	22.646±0.013	24.97±0.14	22.78±0.31	$0.99^{+0.01}_{-0.30}$	$8.97^{+0.52}_{-0.52}$
S164	53.104836	-27.913925	1.090	21.209±0.005	24.88±0.14	21.25±0.18	$0.52^{+0.27}_{-0.27}$	$9.37^{+0.53}_{-0.54}$
S171	53.107746	-27.918444	1.034	22.623±0.019	26.37±0.29	22.66±0.20	< 0.056	< 7.71
S176	53.111511	-27.695988	0.734	21.887±0.009	24.39±0.14	22.00±0.20	$0.35^{+0.29}_{-0.22}$	$8.42^{+0.49}_{-0.49}$
S179[b]	53.115097	-27.695805	0.668	21.614±0.005	24.83±0.14	21.67±0.18	$0.62^{+0.25}_{-0.28}$	$8.72^{+0.50}_{-0.50}$
S184	53.120827	-27.958441	0.640	20.284±0.004	21.78±0.40	20.60±0.48	$0.40^{+0.29}_{-0.24}$	$8.92^{+0.55}_{-0.54}$
S193[b]	53.125252	-27.756536	0.960	21.793±0.009	23.02±0.22	22.22±0.23	< 0.055	< 7.79
S200	53.133675	-27.698660	0.960	23.000±0.028	24.56±0.14	23.30±0.19	$0.21^{+0.33}_{-0.14}$	$7.95^{+0.50}_{-0.51}$
S203	53.137436	-27.688057	1.050	20.922±0.007	25.13±0.15	20.94±0.17	$0.98^{+0.02}_{-0.30}$	$9.74^{+0.57}_{-0.57}$

Continued on Next Page. . .

Table 3.1 – Continued

ID[a]	RA	DEC	z	Total	Pt src	Host	B/Tot	$\log M_{BH}$ ($M_\odot$)
S214	53.145634	-27.919777	0.839	22.182±0.010	24.42±0.14	22.33±0.20	$0.65^{+0.24}_{-0.29}$	$8.72^{+0.51}_{-0.50}$
S220	53.149342	-27.683189	0.735	21.764±0.006	25.82±0.19	21.79±0.18	$0.50^{+0.27}_{-0.27}$	$8.68^{+0.50}_{-0.50}$
S227	53.152973	-27.735123	0.665	22.059±0.010	24.28±0.14	22.21±0.21	$0.89^{+0.09}_{-0.30}$	$8.65^{+0.51}_{-0.50}$
S229	53.156075	-27.666695	0.664	22.164±0.008	23.03±0.22	22.81±0.23	$0.13^{+0.30}_{-0.07}$	$7.51^{+0.52}_{-0.53}$
S249	53.173805	-27.724491	0.979	22.637±0.017	27.09±0.48	22.66±0.20	$0.45^{+0.30}_{-0.26}$	$8.59^{+0.50}_{-0.50}$
S263[b]	53.185226	-27.827835	1.016	22.308±0.008	24.25±0.14	22.51±0.21	$0.69^{+0.22}_{-0.29}$	$8.89^{+0.51}_{-0.51}$
S271	53.195938	-27.729589	1.178	22.146±0.022	25.17±0.15	22.22±0.18	$0.51^{+0.27}_{-0.27}$	$9.04^{+0.52}_{-0.51}$
S273	53.196571	-27.863205	1.069	22.252±0.009	24.70±0.14	22.37±0.19	$0.29^{+0.29}_{-0.18}$	$8.60^{+0.50}_{-0.50}$
S276	53.200741	-27.882389	0.667	20.303±0.004	23.04±0.22	20.39±0.23	$0.48^{+0.28}_{-0.26}$	$9.14^{+0.53}_{-0.52}$
S286[b]	53.220360	-27.855505	1.227	21.830±0.009	23.22±0.20	22.18±0.23	$0.03^{+0.21}_{-0.03}$	$7.85^{+0.51}_{-0.51}$
S293	53.237385	-27.835745	1.143	21.909±0.009	26.02±0.21	21.93±0.19	$0.86^{+0.12}_{-0.30}$	$9.36^{+0.54}_{-0.53}$
S300	53.245888	-27.861118	1.010	23.964±0.047	26.99±0.45	24.03±0.20	$0.28^{+0.36}_{-0.19}$	$7.83^{+0.51}_{-0.51}$

Table 3.2:: Bolometric luminosities derived from reddened SEDs[c], L_X correction[d], direct integration[e], and comparison model[f]

ID	$\log L_X$[g]	$\log N_H$[h]	$E(B-V)$	N_{pt}	$\log L_{bol}$[c,g]	$\log L_{bol,X}$[d,g]	$\log L_{\rm tot,obs}$[e,g]	$\log L_{bol,\rm T09}$[f,g]	$\log \lambda_{edd}$[i]
N 48	44.08	23.30	$1.10^{+0.04}_{-0.15}$	2	45.25	45.24	45.25	45.90	$-2.04^{+0.52}_{-0.52}$
N 72	42.83	22.85	$0.01^{+0.09}_{-0.00}$	2	45.19	43.99	45.02	44.40	$-1.68^{+0.54}_{-0.55}$
N 76	44.21	23.98	$0.82^{+0.17}_{-0.12}$	3	44.95	45.36	45.05	46.05	$-1.87^{+0.50}_{-0.50}$
N 82	42.61	22.69	$0.13^{+0.11}_{-0.12}$	3	45.07	43.77	45.25	44.14	$-2.20^{+0.54}_{-0.56}$
N 90	43.54	23.09	$0.27^{+0.30}_{-0.25}$	1	45.28	44.70	45.34	45.25	$-2.00^{+0.54}_{-0.56}$
N 93	42.60	21.32	$0.42^{+0.04}_{-0.05}$	4	44.09	43.76	44.72	44.13	$-2.67^{+0.50}_{-0.50}$
N103	42.54	20.27	$0.43^{+0.30}_{-0.42}$	3	44.69	43.70	45.26	44.06	$-2.50^{+0.52}_{-0.52}$
N110	42.77	20.81	$0.29^{+0.30}_{-0.28}$	2	44.74	43.93	45.32	44.33	$-2.97^{+0.57}_{-0.59}$
N113	43.15	21.32	$0.51^{+0.11}_{-0.17}$	3	44.58	44.31	45.02	44.79	$-2.33^{+0.51}_{-0.50}$

Continued on Next Page. . .

[a]X-ray IDs from Alexander et al. (2003)
[b]Broad-Line AGN (Cowie et al. 2003; Wirth et al. 2004; Szokoly et al. 2004).

Table 3.2 – Continued

ID	$\log L_X{}^{\mathrm{g}}$	$\log N_H{}^{\mathrm{h}}$	$E(B-V)$	N_{pt}	$\log L_{bol}{}^{\mathrm{c,g}}$	$\log L_{bol,X}{}^{\mathrm{d,g}}$	$\log L_{\mathrm{tot,obs}}{}^{\mathrm{e,g}}$	$\log L_{bol,\mathrm{T09}}{}^{\mathrm{f,g}}$	$\log \lambda_{edd}{}^{\mathrm{i}}$
N116[j]	43.92	20.29	$0.05^{+0.10}_{-0.02}$	4	45.35	45.07	45.60	45.70	$-2.11^{+0.55}_{-0.55}$
N127	43.52	23.52	$0.74^{+0.29}_{-0.13}$	2	45.09	44.68	45.24	45.23	$-2.30^{+0.53}_{-0.53}$
N139	43.00	21.04	$0.26^{+0.30}_{-0.25}$	2	44.70	44.16	45.25	44.60	$-2.83^{+0.54}_{-0.54}$
N150	42.97	22.93	$0.61^{+0.18}_{-0.13}$	2	44.34	44.12	44.40	44.56	$-2.19^{+0.50}_{-0.50}$
N158	43.09	22.91	$1.45^{+0.05}_{-1.17}$	2	45.05	44.25	45.37	44.72	$-1.43^{+0.50}_{-0.50}$
N160	43.10	23.08	$0.36^{+0.15}_{-0.12}$	4	44.83	44.25	45.25	44.72	$-2.57^{+0.53}_{-0.54}$
N163	43.62	23.90	$0.31^{+0.30}_{-0.30}$	3	45.02	44.78	45.00	45.34	$-2.03^{+0.64}_{-1.09}$
N164	44.49	23.61	$0.47^{+0.14}_{-0.11}$	4	45.11	45.65	44.99	46.39	$-1.67^{+0.50}_{-0.50}$
N170	42.50	22.43	$0.54^{+0.03}_{-0.03}$	3	44.44	43.66	44.76	44.01	$-1.16^{+0.53}_{-0.52}$
N174	43.40	19.32	$0.01^{+0.04}_{-0.00}$	2	45.09	44.56	45.43	45.08	$-2.32^{+0.54}_{-0.55}$
N177	42.59	21.74	$0.38^{+0.01}_{-0.37}$	3	44.86	43.75	45.31	44.12	$-2.40^{+0.52}_{-0.53}$
N187	42.56	23.27	$0.61^{+0.02}_{-0.60}$	4	44.74	43.72	44.99	44.08	$-0.58^{+0.55}_{-0.54}$

Continued on Next Page. . .

Table 3.2 – Continued

ID	$\log L_X$[g]	$\log N_H$[h]	$E(B-V)$	N_{pt}	$\log L_{bol}$[c,g]	$\log L_{bol,X}$[d,g]	$\log L_{\mathrm{tot,obs}}$[e,g]	$\log L_{bol,\mathrm{T09}}$[f,g]	$\log \lambda_{edd}$[i]
N194	42.63	19.95	$0.62^{+0.30}_{-0.08}$	4	43.89	43.79	44.37	44.17	$-2.26^{+0.50}_{-0.50}$
N201	43.10	23.69	$1.02^{+0.03}_{-1.01}$	2	44.71	44.26	44.79	44.73	$-2.48^{+0.52}_{-0.53}$
N205	43.29	21.69	$0.34^{+0.05}_{-0.06}$	4	44.92	44.45	45.04	44.96	$-2.23^{+0.51}_{-0.51}$
N217	42.79	23.70	$1.60^{+0.05}_{-1.59}$	4	44.57	43.94	45.00	44.35	$-1.97^{+0.51}_{-0.50}$
N222	42.79	21.35	$0.25^{+0.30}_{-0.24}$	3	44.95	43.95	45.36	44.35	$-2.28^{+0.52}_{-0.52}$
N240	44.07	22.63	$0.99^{+0.11}_{-0.22}$	2	45.22	45.23	45.41	45.89	$-2.43^{+0.55}_{-0.56}$
N242	42.66	23.42	$5.00^{+0.16}_{-0.16}$	4	44.29	43.82	44.50	44.20	$-1.82^{+0.50}_{-0.50}$
N261	42.55	23.49	$0.52^{+0.02}_{-0.51}$	4	44.58	43.71	44.80	44.06	$-2.59^{+0.53}_{-0.53}$
N262	42.90	20.18	$1.79^{+0.06}_{-1.77}$	1	44.21	44.06	44.74	44.49	$-2.43^{+0.50}_{-0.50}$
N266	43.49	23.61	$0.62^{+0.08}_{-0.06}$	4	44.95	44.65	44.90	45.19	$-2.08^{+0.51}_{-0.51}$
N278	43.00	23.29	$0.80^{+0.30}_{-0.14}$	1	44.72	44.16	44.72	44.60	$-1.81^{+0.50}_{-0.50}$
N286	42.73	21.68	$1.31^{+0.04}_{-1.30}$	2	44.34	43.89	45.10	44.28	$-2.91^{+0.52}_{-0.52}$

Continued on Next Page. . .

Table 3.2 – Continued

ID	$\log L_X{}^{\mathrm{g}}$	$\log N_H{}^{\mathrm{h}}$	$E\,(B-V)$	N_{pt}	$\log L_{bol}{}^{\mathrm{c},g}$	$\log L_{bol,X}{}^{\mathrm{d},g}$	$\log L_{\mathrm{tot,obs}}{}^{\mathrm{e},g}$	$\log L_{bol,\mathrm{T09}}{}^{\mathrm{f},g}$	$\log \lambda_{edd}{}^{\mathrm{i}}$
N304	43.20	20.94	$0.17^{+0.15}_{-0.07}$	3	44.62	44.35	45.07	44.84	$-2.57^{+0.52}_{-0.53}$
N309	43.04	21.30	$0.88^{+0.30}_{-0.54}$	1	44.59	44.20	45.04	44.66	$-2.46^{+0.51}_{-0.51}$
N323$^{\mathrm{j}}$	43.50	21.97	$0.19^{+0.16}_{-0.09}$	4	44.90	44.66	45.18	45.21	$-1.79^{+0.55}_{-0.55}$
N349	42.94	21.84	$0.55^{+0.02}_{-0.01}$	4	44.44	44.09	44.61	44.53	$-2.24^{+0.50}_{-0.50}$
N352	42.73	23.13	$5.00^{+0.00}_{-0.16}$	3	44.70	43.89	45.29	44.28	$-2.39^{+0.51}_{-0.52}$
N370	43.01	20.96	$0.30^{+0.08}_{-0.07}$	4	44.65	44.17	44.95	44.62	$-2.38^{+0.51}_{-0.51}$
N373	42.63	22.77	$1.52^{+0.05}_{-1.51}$	4	44.11	43.79	44.36	44.16	$-2.09^{+0.51}_{-0.50}$
N384	43.64	23.39	$2.38^{+0.08}_{-1.63}$	2	44.93	44.80	45.15	45.37	$-1.90^{+0.50}_{-0.50}$
N390	44.13	22.35	$1.39^{+0.05}_{-1.37}$	1	45.66	45.29	45.59	45.96	$-0.82^{+0.50}_{-0.51}$
N402	42.81	23.20	$1.24^{+0.17}_{-0.18}$	4	44.47	43.97	44.64	44.37	$-0.46^{+0.59}_{-0.58}$
N405	43.24	23.41	$1.40^{+0.05}_{-1.34}$	3	44.83	44.40	45.25	44.89	$-2.54^{+0.53}_{-0.53}$
N437	42.83	21.36	$0.58^{+0.03}_{-0.11}$	4	44.62	43.99	45.31	44.40	$-2.40^{+0.51}_{-0.51}$

Continued on Next Page. . .

Table 3.2 – Continued

ID	$\log L_X$[g]	$\log N_H$[h]	$E(B-V)$	N_{pt}	$\log L_{bol}$[c,g]	$\log L_{bol,X}$[d,g]	$\log L_{\mathrm{tot,obs}}$[e,g]	$\log L_{bol,\mathrm{T09}}$[f,g]	$\log \lambda_{edd}$[i]
N442	43.16	23.89	$0.13^{+0.04}_{-0.02}$	4	44.97	44.32	44.85	44.79	$-1.41^{+0.50}_{-0.51}$
N448	43.47	23.16	$1.39^{+0.05}_{-0.97}$	1	44.89	44.62	45.09	45.16	$-1.91^{+0.50}_{-0.50}$
N451[j]	43.96	21.06	$0.01^{+0.30}_{-0.00}$	3	45.53	45.11	45.53	45.75	$0.29^{+0.63}_{-0.60}$
N471	42.84	22.90	$0.96^{+0.19}_{-0.16}$	3	44.90	44.00	45.58	44.41	$-2.73^{+0.55}_{-0.55}$
N473[j]	43.28	18.23	$0.13^{+0.01}_{-0.00}$	3	44.60	44.44	45.05	44.94	$-2.33^{+0.69}_{-0.71}$
S 44	43.38	22.87	$0.77^{+0.10}_{-0.11}$	3	44.69	44.54	45.00	45.06	$-2.11^{+0.50}_{-0.50}$
S 84	42.72	22.42	$0.98^{+0.13}_{-0.21}$	2	44.72	43.87	45.06	44.26	$-2.61^{+0.53}_{-0.53}$
S 88	43.49	22.42	$0.50^{+0.01}_{-0.00}$	4	44.94	44.65	45.21	45.19	$-2.70^{+0.56}_{-0.56}$
S 91	43.08	23.57	$0.68^{+0.17}_{-0.22}$	3	44.72	44.24	44.96	44.70	$-2.02^{+0.50}_{-0.50}$
S103[j]	42.90	19.98	$0.95^{+0.03}_{-0.94}$	2	44.35	44.06	44.92	44.48	$-2.40^{+0.50}_{-0.50}$
S117	43.12	20.46	$0.01^{+0.00}_{-0.01}$	3	44.58	44.28	44.78	44.75	$-1.60^{+0.50}_{-0.50}$
S118	44.23	23.30	$1.31^{+0.30}_{-1.30}$	2	45.26	45.39	45.26	46.08	> -0.93

Table 3.2 – Continued

ID	$\log L_X{}^{\mathrm{g}}$	$\log N_H{}^{\mathrm{h}}$	$E(B-V)$	N_{pt}	$\log L_{bol}{}^{\mathrm{c},g}$	$\log L_{bol,X}{}^{\mathrm{d},g}$	$\log L_{\mathrm{tot,obs}}{}^{\mathrm{e},g}$	$\log L_{bol,\mathrm{T09}}{}^{\mathrm{f},g}$	$\log \lambda_{edd}{}^{\mathrm{i}}$
S134	43.33	23.26	$0.96^{+0.26}_{-0.16}$	2	44.52	44.48	44.47	44.99	$-1.93^{+0.50}_{-0.50}$
S137	42.92	23.38	$0.44^{+0.14}_{-0.15}$	3	44.63	44.08	44.80	44.51	$-2.17^{+0.51}_{-0.51}$
S139	42.84	23.71	$0.10^{+0.30}_{-0.09}$	4	44.96	43.99	44.98	44.41	$-1.84^{+0.54}_{-0.54}$
S151	42.50	21.76	$1.25^{+0.30}_{-0.98}$	2	44.53	43.66	44.99	44.01	> -1.56
S155	42.73	21.22	$0.41^{+0.09}_{-0.11}$	3	44.16	43.89	44.76	44.28	$-2.46^{+0.50}_{-0.50}$
S156	43.28	22.65	$0.43^{+0.30}_{-0.29}$	4	44.72	44.43	44.91	44.94	$-2.25^{+0.51}_{-0.52}$
S159	43.57	21.76	$1.22^{+0.04}_{-1.10}$	1	44.63	44.73	44.75	45.29	$-2.36^{+0.51}_{-0.51}$
S160	43.02	23.19	$0.28^{+0.30}_{-0.20}$	4	44.58	44.18	44.16	44.63	$-1.90^{+0.64}_{-0.97}$
S161	43.19	22.86	$0.47^{+0.05}_{-0.07}$	3	44.69	44.35	44.84	44.83	$-2.40^{+0.51}_{-0.52}$
S162	42.69	22.69	$0.22^{+0.01}_{-0.21}$	4	44.55	43.85	44.49	44.24	$-2.47^{+0.53}_{-0.53}$
S164	43.53	23.56	$1.03^{+0.03}_{-1.02}$	2	45.04	44.69	45.29	45.24	$-2.42^{+0.54}_{-0.54}$
S171	42.55	21.32	$0.53^{+0.02}_{-0.02}$	2	44.44	43.71	44.78	44.06	> -1.41

Continued on Next Page. . .

Table 3.2 – Continued

ID	$\log L_X^{\text{g}}$	$\log N_H^{\text{h}}$	$E(B-V)$	N_{pt}	$\log L_{bol}^{\text{c},g}$	$\log L_{bol,X}^{\text{d},g}$	$\log L_{\text{tot,obs}}^{\text{e},g}$	$\log L_{bol,\text{T09}}^{\text{f},g}$	$\log \lambda_{edd}^{\text{i}}$
S176	43.01	22.35	$0.01^{+0.30}_{-0.00}$	3	45.01	44.16	44.87	44.61	$-1.58^{+0.52}_{-0.54}$
S179[j]	43.38	22.85	$0.90^{+0.03}_{-0.89}$	2	44.87	44.54	44.82	45.06	$-1.93^{+0.50}_{-0.50}$
S184	42.86	21.16	$0.01^{+0.00}_{-0.01}$	3	44.74	44.02	45.16	44.44	$-2.26^{+0.54}_{-0.55}$
S193[j]	43.29	21.05	$0.53^{+0.30}_{-0.18}$	2	44.90	44.45	45.18	44.95	> -1.00
S200	42.92	21.91	$0.35^{+0.01}_{-0.02}$	4	44.77	44.08	44.83	44.51	$-1.32^{+0.51}_{-0.51}$
S203	42.75	22.81	$0.44^{+0.06}_{-0.10}$	4	44.83	43.90	45.35	44.30	$-3.01^{+0.57}_{-0.57}$
S214	43.16	21.70	$0.42^{+0.03}_{-0.07}$	3	44.68	44.32	44.81	44.80	$-2.14^{+0.50}_{-0.51}$
S220	43.21	23.23	$0.64^{+0.06}_{-0.06}$	3	44.56	44.37	44.71	44.86	$-2.22^{+0.50}_{-0.50}$
S227	43.32	21.46	$0.49^{+0.01}_{-0.01}$	2	44.38	44.47	44.52	44.98	$-2.33^{+0.50}_{-0.51}$
S229	42.98	20.07	$0.06^{+0.03}_{-0.01}$	2	44.36	44.14	44.53	44.58	$-1.26^{+0.53}_{-0.52}$
S249	43.36	23.74	$0.47^{+0.12}_{-0.15}$	4	44.89	44.52	44.88	45.04	$-1.80^{+0.50}_{-0.50}$
S263[j]	43.47	22.77	$5.00^{+0.16}_{-0.16}$	1	44.31	44.63	44.70	45.17	$-2.67^{+0.51}_{-0.51}$

Table 3.2 – Continued

ID	$\log L_X$[g]	$\log N_H$[h]	$E(B-V)$	N_{pt}	$\log L_{bol}$[c,g]	$\log L_{bol,X}$[d,g]	$\log L_{\mathrm{tot,obs}}$[e,g]	$\log L_{bol,\mathrm{T09}}$[f,g]	$\log \lambda_{edd}$[i]
S271	43.29	23.11	$0.54^{+0.30}_{-0.53}$	2	44.97	44.45	45.04	44.96	$-2.19^{+0.52}_{-0.52}$
S273	42.41	21.37	$0.20^{+0.30}_{-0.16}$	2	44.33	43.57	44.79	43.90	$-2.39^{+0.50}_{-0.50}$
S276	42.65	22.65	$0.01^{+0.10}_{-0.00}$	3	44.97	43.81	45.13	44.19	$-2.40^{+0.57}_{-0.62}$
S286[j]	43.74	20.85	$0.30^{+0.30}_{-0.20}$	2	45.27	44.89	45.29	45.48	$-0.68^{+0.51}_{-0.51}$
S293	42.56	19.49	$5.00^{+0.00}_{-0.16}$	2	44.28	43.71	45.06	44.07	$-3.18^{+0.54}_{-0.55}$
S300	42.74	21.50	$0.66^{+0.30}_{-0.65}$	4	44.56	43.90	44.68	44.30	$-1.38^{+0.51}_{-0.51}$

[c]Method 1 in Section 3.4.3; described in detail in Section 3.4.2.
[d]Method 2 in Section 3.4.3; described in detail in Section 3.4.1.
[e]Method 3 in Section 3.4.3.
[f]Method 4 in Section 3.4.3; from Treister et al. (2009).
[g]All luminosities are in cgs (erg s^{-1}).
[h]Gas column density in cm^{-2}.
[i]Calculated using L_{bol} from Method 1.
[j]Broad-Line AGN (Cowie et al. 2003; Wirth et al. 2004; Szokoly et al. 2004).

Chapter 4

Moderate-luminosity Growing Black Holes from $1.25 < z < 2.7$: Varied Accretion in Disk-Dominated Hosts

Abstract

We compute black hole masses and bolometric luminosities for 57 obscured active galactic nuclei (AGN) in the redshift range $1.25 \leq z \leq 2.67$, selected from the GOODS-South deep multi-wavelength survey field via their X-ray emission. We determine host galaxy morphological parameters by separating the galaxies from their central point sources in deep *HST* images, and host stellar masses and colors by multi-wavelength SED fitting. 90% of GOODS AGN at these redshifts have detected rest-frame optical nuclear point sources; bolometric luminosities range from $2 \times 10^{43-46}$ erg s^{-1}. The black holes are growing at a range of accretion rates, with $\sim 60\%$ of the sample having $L/L_{Edd} < 0.1$. 70% of host galaxies have stellar masses $M_* > 10^{10} M_\odot$, with a range of colors suggesting a complex star formation history. We find no evolution of AGN

---

[1]This Chapter has been submitted as a paper to the Astrophysical Journal.

bolometric luminosity within the sample, and no correlation between AGN bolometric luminosity and host stellar mass, color or morphology. Fully half the sample of host galaxies is disk-dominated, with another 25% having strong disk components. $\lesssim 15\%$ of the systems appear to be at some stage of a major merger. These moderate-luminosity AGN hosts are therefore inconsistent with a dynamical history dominated by mergers strong enough to destroy disks, indicating minor mergers or secular processes dominate the co-evolution of galaxies and their central black holes at $z \sim 2$.

4.1   Introduction

The black hole-galaxy connection is well-established at local (e.g., Ferrarese & Ford 1999; Gebhardt et al. 2000; Marconi & Hunt 2003; Häring & Rix 2004) and moderate (e.g., Treu et al. 2004; Woo et al. 2005; Peng et al. 2006; Bennert et al. 2010, 2011a) redshifts. However, the pathways leading to the observed co-evolution are unclear, especially for moderate-luminosity AGN and host galaxies, which cumulatively dominate the observed X-ray background and the constitute a large fraction of the underlying black hole growth in the universe (Hasinger et al. 2005; Treister & Urry 2012). Clues to understanding the co-evolution of galaxies and their central supermassive black holes come from detailed study of both moderate-luminosity growing black holes and the galaxies that host them.

Examination of both AGN and host galaxies requires separation of their blended signal, preferentially with a combination of space- and ground-based data at multiple wavelengths. Using deep *Hubble Space Telescope* (*HST*) data to extract nuclear point sources from AGN+host images requires care but provides the leverage needed to determine AGN bolometric (total) luminosities and host galaxy stellar masses and morphologies (Simmons & Urry 2008; Simmons et al. 2011).

Until recently, such analyses for large, uniform AGN+host samples in the rest-frame optical were only possible to $z \lesssim 1.3$ using deep survey data taken with the Advanced Camera for Surveys (ACS) on *HST*. Results of multiple studies of host galaxy morphologies and black hole growth rates at those redshifts indicate a complex picture, with moderate-luminosity AGN predominantly powered by high-mass, slow-growing black holes (Simmons et al. 2011) in host galaxies with a range of morphologies (Sánchez et al. 2004; Bundy et al. 2008; Gabor et al. 2009).

Mergers are often invoked to trigger black hole accretion (e.g., Sanders et al. 1988; Croton et al. 2006; Hopkins et al. 2006a), but mergers are equally common in galaxies hosting actively growing and inactive black holes (Grogin et al. 2005). Moreover, moderate-luminosity AGN at $z \sim 1$, which are powered by high-mass black holes that have already undergone significant growth, commonly found in disk-dominated systems (Simmons et al. 2011). This raises the issue of whether black hole growth is similar at $z \sim 2$, where star formation (Lilly et al. 1996; Madau et al. 1998) and AGN activity (e.g., Fan et al. 2001; Wall et al. 2005) both peak, or whether mergers are relatively more important.

The recently-installed Wide Field Camera-3 (WFC3) instrument on *HST* now provides high-resolution, rest-frame optical images of AGN and host galaxies to $z \sim 2$. With the Cosmic Assembly Near-infrared Deep Extragalactic Legacy Survey (CANDELS; Grogin et al. 2011) imaging in the deep *Chandra* legacy fields, we can separate AGN and hosts at rest-frame optical and UV wavelengths, enabling detailed investigations of the properties of both moderate-luminosity growing black holes and their host galaxies.

In Section 4.2 we describe our sample selection and analysis methods. Section 4.3 presents the AGN host galaxy morphologies, stellar masses and colors, as well as estimates of black hole masses and growth rates for the AGN in the sample. Section 4.4

discusses these results in the overall context of black hole-galaxy co-evolution, specifi-
cally merger-driven versus secular growth scenarios.

Throughout this paper, we adopt a ΛCDM cosmology with $H_0 =$
71 km s^{-1} Mpc^{-1}, $\Omega_M = 0.27, \Lambda_0 = 0.73$ (Spergel et al. 2003).

4.2   Data

4.2.1   Sample Selection

The *Chandra* Deep Field - South is one of the best-observed parts of the sky, with deep
multi-wavelength coverage from both ground- and space-based observatories. In par-
ticular, the 4 Megaseconds of combined X-ray observations within the field (Xue et al.
2011) allow for selection of AGN at $z \sim 2$ that is relatively unbiased with respect to ob-
scuration. Examination of those AGN and their hosts at rest-frame optical wavelengths
is possible with the multi-epoch deep observations of the GOODS-South field (chosen
to coincide with the CDF-S; see Giavalisco et al. 2004) within the CANDELS survey
(Grogin et al. 2011). We match the X-ray sources to WFC3 sources using a maximum-
likelihood method (Cappelluti et al. 2009; Cardamone et al. 2010) that considers both
positional overlap and uncertainties as well as multi-wavelength source fluxes to deter-
mine the most probable optical match to each X-ray source.

We select AGN within the *Chandra*-GOODS-S-CANDELS field according to the
following criteria:

1. Redshifts (compiled by Xue et al. 2011) within the range $1.25 < z < 2.67$, so that
   the observed wavelength ranges spanned by the F125W and F160W WFC3 *HST*
   filters are in the rest-frame *B* band;

2. Source type identification as AGN within the Xue et al. (2011) 4 Ms X-ray catalog.

Briefly, AGN are identified via X-ray luminosity, photon index, X-ray-to-optical flux ratio, X-ray excess over measured star formation, and/or optical spectroscopic features. The criteria are described further in Xue et al.;

3. Extended source detection within the WFC3 image with a signal-to-noise of at least 5 per pixel to ensure robustness of morphological fitting; and

4. Extended source detections in at least five optical and infrared bands, to facilitate accurate determination of stellar masses and rest-frame colors.

Of the 57 X-ray-selected AGN in the sample using the above criteria, 41 are considered luminous AGN by Xue et al. owing to their having absorption-corrected, rest-frame $0.5 - 8$ keV luminosities $L_X \geq 3 \times 10^{42}$ erg s^{-1}. An additional 14 sources have $10^{42} \leq L_X < 3 \times 10^{42}$ erg s^{-1}, and the remaining two have luminosities of 9.1 and 9.5×10^{41} erg s^{-1}. The median and mean X-ray luminosities of the sample are 4.4 and 7.3×10^{42} erg s^{-1}, respectively, and the most luminous X-ray AGN in the sample has $L_X = 2.6 \times 10^{44}$ erg s^{-1}, consistent with expected detections within the volume of GOODS-S based on the AGN luminosity function (Croom et al. 2004).

The CANDELS survey (Grogin et al. 2011) includes several deep and wide fields on the sky with both the WFC3 and ACS cameras on *HST*. We perform morphological fits on the publicly available co-added six-epoch images in both the F125W and F160W bands, which were drizzled to a resolution of $0''.06$ per pixel. For details of the image processing, see Koekemoer et al. (2011).

Morphological decomposition of two-dimensional AGN+host galaxy images requires accurate determination of the point-spread function (PSF). We determine the PSF of the F125W and F160W CANDELS images using the PSF-modeling routines in the IRAF package `daophot`. This method balances the noise-free attributes of a simulated PSF model with the detailed particulars of the actual PSF of multi-drizzled,

multi-epoch data. We verified that the WFC3 PSF is very stable across the deep mosaic in the GOODS-S field, so we determine a single PSF for each band and use it in the morphological analysis of each of the sources.

4.2.2   Morphological Fitting

We perform two-dimensional parametric morphological fitting on the F125W and F160W images for the 57 sources using `GALFIT` (Peng et al. 2002), which is very reliable for recovering both normal galaxy morphologies and AGN-host decomposition (see, e.g., Häussler et al. 2007; Simmons & Urry 2008; Pierce et al. 2010a, for simulations).

Our detailed fitting procedure is similar to that performed in previous simulations and studies of AGN host morphologies (Simmons & Urry 2008; Simmons et al. 2011). We determine initial guesses for fit parameters such as total source magnitude, half-light radius, axis ratio, position angle and centroid position using SExtractor (Bertin & Arnouts 1996). The value of the sky background varies slightly across the CANDELS mosaic, so we fix the SExtractor-determined value for each source and each iteration of the morphological fitting in order to avoid the confusion of sky background and extended source light that can ensue when the sky background is allowed to vary along with the other fit components.

We fit each galaxy with two models in each band: (1) a host galaxy modeled by a Sérsic profile (Sérsic 1968), and (2) a host galaxy with a central point source. We determine the final fit parameters via an iterative process that initially fits only the central portion of the AGN+host, to find the best-fit centroid positions of each fit component. Those positions are then held fixed in successive iterations, which zoom outward to eventually encompass a large enough image region such that the extended portions of the central source are well sampled. Where necessary, we fit nearby, bright and/or ex-

tended companions in order to simultaneously model their extended light distributions. Companion fitting (and masking of fainter, more compact companions further from the central source) ensures a more realistic fit to the central source. The first three fits to each source are performed with the use of a customized adaptive batch-fitting code. Each source is then followed up individually to ensure the true minimum reduced χ^2_ν value within the parameter space is achieved.

For each source and each fit (Sérsic only and Sérsic+Point Source), we perform one final iteration where every parameter (with the exception of the sky background) is allowed to vary. This final iteration ensures that `GALFIT` has found the true best fit and also allows for an estimate of the computational uncertainties for each parameter, including the centroid positions of each component. For all sources, the differences between the final fit parameters and those of the penultimate iteration are well within the reported parameter uncertainties; thus, we are confident that we have found the true best-fit parameters for each source and fit type. Typically, an AGN+host galaxy in the sample requires 6-8 total iterations for a Sérsic+PSF fit, with 1-4 fitted companions. Some of the sources require additional iterations, usually due to the presence of multiple (occasionally more than 4) bright, nearby companions.

The final step in the determination of AGN+host morphologies involves comparing the Sérsic-only and the Sérsic+Point Source fits for each of the 57 sources in order to determine whether we significantly detect a central point source. Detailed simulations of the recovery of central point sources within ACS data (Simmons & Urry 2008) suggest that failed detections of intrinsically-detectable point sources (*i.e.*, false negatives) are rare, but spurious point-source detection (*i.e.*, false positive) rates are strongly dependent on host morphology, ranging from $\sim 1\%$ in a sample of pure disk galaxies to $\sim 25\%$ for a sample of pure bulges. When `GALFIT` does not detect a central point source, therefore, this is most likely a robust indicator that any light from a central AGN is
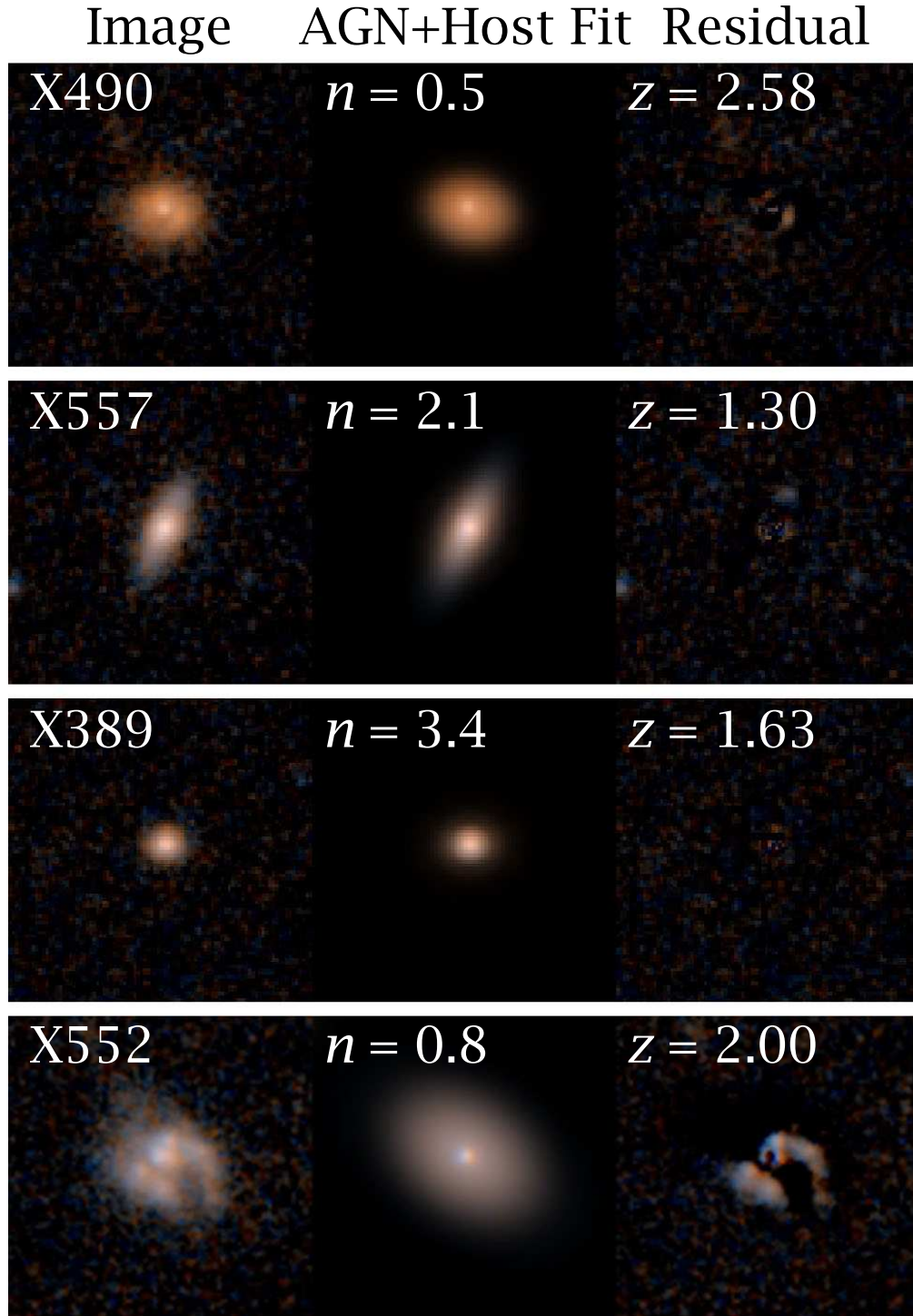
Fig. 4.1.— *HST* WFC3 $F125W + F160W$ images (left), 2-dimensional morphological fits (center), and residuals (image - fit; right) for four X-ray selected AGN+hosts in this sample (from top to bottom): a disk-dominated, intermediate, and strong-bulge host morphology, as well as a clumpy/asymmetric host galaxy. Object 389 does not have a detected nuclear point source; the other three have point source detections to $\geq 5\sigma$.

below the detection threshold of the image. Detection of a central point source in a Sérsic+Point Source fit, on the other hand, is not a guarantee of its authenticity.

We therefore assess the robustness of each point-source detection based on a number of criteria. First, if an F-test indicates that the addition of a point source significantly improves the χ_ν^2 goodness-of-fit parameter, we consider the point source genuine. Alternatively, we consider a point source genuine if the Sérsic-only fit converges to an unrealistically high value for the Sérsic index n. Lastly, we examine the central portion of the fit residuals. We consider a point source genuine if the residual of the Sérsic-only fit shows obvious signs of additional light from an unresolved source (however, in practice at least one of the other two criteria also apply if this last criterion is true).

Figure 4.1 shows a selection of fitted AGN+hosts; we present the full catalog of best-fit morphological parameters for each source in Table 4.1. The uncertainties reported in Table 4.1 are determined by combining in quadrature the reported computational uncertainties from `GALFIT` and the uncertainties in morphological parameter recovery determined from the simulation of over 50,000 AGN host galaxies by Simmons & Urry (2008). The latter typically dominate the overall uncertainty in a morphological fit.

4.3   Results

4.3.1   AGN Host Morphologies

Just under half (25) of the host galaxies in this sample are best described as single-component galaxies with smooth residuals after subtracting a single-component host fit. Fourteen have clumpy morphologies, with multiple offset components either embedded in a larger component or very closely separated. Eighteen host galaxies ($\approx 32\%$) show signs of asymmetric features or tidal tails in the images and/or fit residuals; 8 of these

appear to be involved in major mergers, consistent with an independent assessment of an overlapping sample using visual morphologies (Kocevski et al. 2011).

Using the F-test to assess the significance of improvements to the fit with the addition of a central point source, we find that 90% of AGN+hosts have point source detections with at least 3σ significance. The majority are at least 5σ point-source detections. We quote point-source-subtracted host morphologies for the 51 sources that have a point source at a minimum significance level of 3σ; for the remaining six sources we quote the morphology from the Sérsic-only fit. As expected, for those sources where the addition of a point source was not significant, the host morphology does not significantly change between the Sérsic only and the Sérsic + point source fit.

We show the fitted Sérsic indices for the AGN host galaxies in Figure 4.2. Morphologies of the hosts, or (for the clumpy hosts) of the component within the host associated with the nuclear source, are typically disky. Just over half the sample has $n < 1.5$ (29 of 57 hosts), an unambiguously disk-dominated morphology. An additional 15 have $1.5 \leq n < 3$, which is consistent with intermediate morphologies (bulge-to-total ratios between 20 and 65%). Indeed, Simmons & Urry (2008) have shown that even galaxies fit with $n = 4$ can have a significant disk component (up to 45%). Five sources have $3 < n < 4$, and 8 have $n > 4$. The overall sample can therefore be characterized as having a mix of morphological types, but disks are present in roughly three-quarters of the sample, and $\sim 50\%$ of hosts are consistent with having a bulge fraction of less than 20%. (In fact, 21 of the 29 disk-dominated sources have $n \leq 1$, consistent with a bulge-to-total ratio of $\leq 10\%$.)

The redshift range over which the $F125W$ and $F160W$ WFC3 filters sample the rest-frame B band spans approximately 2.6 Gyr of cosmic time. Splitting the sample into two sub-samples of $\Delta t \approx 1.3$ Gyr each reveals no difference in the distribution of morphologies between the two bins, according to a Kolmogorov-Smirnov (K-S) test.
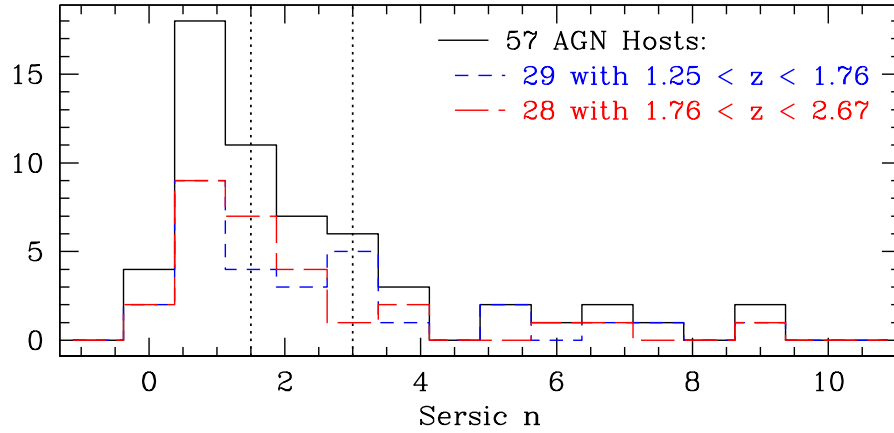
Fig. 4.2.— Distribution of fitted Sérsic indices for the sample of 57 AGN host galaxies from $1.25 < z < 2.67$. The sample is characterized by disky morphologies (median $n = 1.5$). This is conservative: extensive simulations of AGN host morphologies (Simmons & Urry 2008) show that while a fitted $n \lesssim 1.5$ strictly confines the bulge contribution to less than 20%, AGN host galaxies with fitted $n = 4$ can still have significant intrinsic disks. We follow Simmons & Urry in separating host galaxies into three groups based on cuts at $n = 1.5$ and 3 (dotted lines). Sérsic indices for sub-samples in two redshift bins spanning equal time intervals ($\Delta t \approx 1.3$ Gyr) are consistent with being drawn from the same parent sample.

4.3.2 Host Galaxy Stellar Masses and Colors

We determine stellar masses of the host galaxies using the multi-wavelength GOODS+CANDELS $BVIzJHKs$ SEDs, using FAST (Kriek et al. 2009) and the stellar population synthesis templates of Maraston (2005). (To test the dependence of recovered stellar masses on the choice of template, we also calculated stellar masses using the templates of Bruzual & Charlot 2003; we found that the recovered stellar mass is not strongly dependent on the choice of template set.) The distribution of masses is shown in Figure 4.3. The minimum and maximum masses of the sample are 2×10^8 and 6×10^{11} $M_\odot$, respectively; the average and median masses are 1.7×10^{10} and 2.3×10^{10} $M_\odot$, respectively. 70% of the sample has $M_* > 10^{10}$ $M_\odot$, which is expected since AGN are typically found in massive hosts (Cardamone et al. 2010); this probably reflects a selection effect missing slow-growing black holes in low-mass galaxies rather than an intrinsic distribution (Aird et al. 2012). The average uncertainty in the mass is 0.8 dex.

We visually inspected each of the best-fit templates from FAST and verified the goodness-of-fit. We use the best-fit templates to determine the rest-frame $(U - V)$ colors of each host galaxy, following Brammer et al. (2009) in assuming a Calzetti et al. (2000) dust law to correct for dust, such that $(U - V)_{corr} = (U - V) - \Delta A_V$, where $\Delta A_V = 0.47 A_V$. We show the color-mass diagrams for the AGN host sample in Figure 4.4, compared to inactive galaxies with the same redshifts (from the NEWFIRM medium-band survey; Whitaker et al. 2011). We separate the sample into two redshift bins divided at $z = 1.76$, so that each bin represents a time interval of $\Delta t \approx 1.3$ Gyr.

A K-S test indicates no significant difference between the stellar mass distributions of the AGN hosts in the two redshift bins. The uncorrected $U - V$ colors between the bins are inconsistent with being drawn from the same parent sample at the 97% level, but the significance is reduced to 75% ($\sim 1\sigma$) once the dust correction is applied:
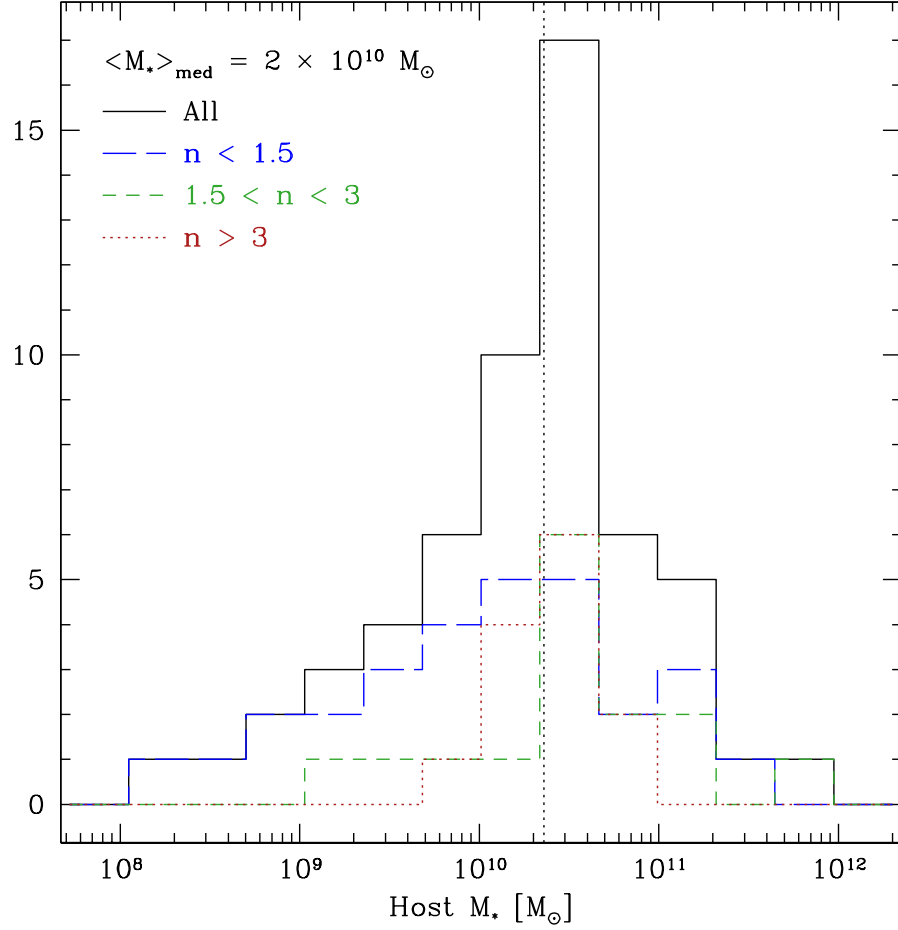
Fig. 4.3.— Histogram of stellar masses for AGN hosts with $1.25 < z < 2.67$. The full sample (solid black line) has a median value of $2 \times 10^{10}\ M_\odot$ (dotted line); we also show histograms for the unambiguously disk-dominated ($n < 1.5$; blue long-dash line), intermediate ($1.5 < n < 3$; green short-dash line), and strong-bulge ($n > 3$; red dotted line) sub-samples. Disk-dominated host galaxies tend to have lower masses than those with strong-bulge morphologies (K-S $\approx 93\%$).
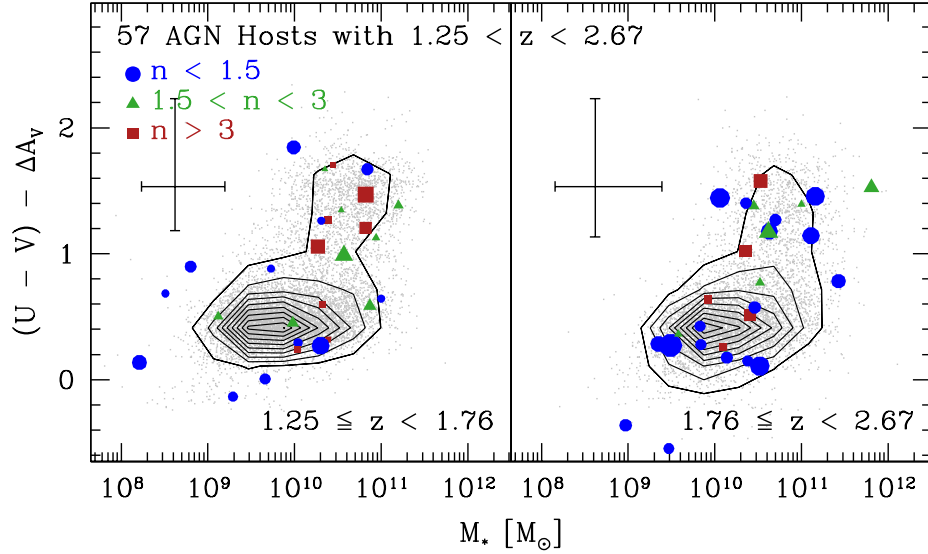
Fig. 4.4.— Rest-frame $(U-V)_{AB}$ color versus stellar mass for the host galaxies of AGN with $1.25 < z < 2.67$, separated into two redshift bins of approximately equal $\Delta t \approx 1.3$ Gyr. Disk-dominated (blue circles) host galaxies populate both the "blue cloud" and "red sequence" portions of the diagram. Intermediate-morphology (green triangles) host galaxies are more likely to populate the green valley; strong-bulge (red squares) hosts are more likely to have redder colors, but not exclusively. Although the stellar mass distributions are statistically indistinguishable, dust-corrected color distributions of AGN host galaxies between the two redshift bins are marginally statistically different (at the 75% level according to a K-S test). Median error bars are shown in each panel. The size of each point representing a host galaxy is proportional to its AGN bolometric luminosity. Contours and gray points show the positions of inactive galaxies in the same redshift bins (Whitaker et al. 2011).

correcting for dust shifts more galaxies into the blue cloud in the lower redshift bin than in the higher. Comparison of the colors of morphological sub-samples in different redshift bins is highly uncertain due to small numbers in each sub-sample. However, we observe intrinsically red disk-dominated and blue strong-bulge hosts in each redshift bin.

Note that, although the stellar mass determination is unaffected (within the uncertainties) by the choice of model templates, the value of the dust correction A_V can vary significantly depending on the choice of template. We include differences in each source's dust-correction between the Bruzual & Charlot (2003) and Maraston (2005) templates in the uncertainties shown in Figure 4.4, noting that the choice of template does not change the overall result.

4.3.3 Black Hole Masses and Accretion Rates

Black hole mass, one of the fundamental properties of an AGN, can be measured directly only for very nearby sources. If a black hole is unobscured, measurements of broad spectral lines from the region near the black hole allow for calculations of central masses via the virial method. However, this is not generally possible for obscured sources like those that dominate the present sample. Instead, we use well-characterized relations between host galaxy properties and black hole masses, which allow estimates of black hole masses out to high redshift as long as evolutionary corrections are considered.

Locally, black hole mass correlates with the velocity dispersion (*e.g.,* Ferrarese & Merritt 2000; Gebhardt et al. 2000), mass (*e.g.,* Magorrian et al. 1998; Häring & Rix 2004) and optical luminosity (*e.g.,* Marconi & Hunt 2003; Ferrarese & Ford 2005; Graham 2007) of the stellar bulge. These relations may evolve as a result of multiple effects (Treu et al. 2004; Borys et al. 2005; Woo et al. 2005; Peng et al. 2006; Alexander et al. 2008; Woo et al. 2008; Jahnke et al. 2009; Decarli et al. 2010; Merloni et al. 2010; Bluck

et al. 2011). It appears that bulge stellar populations are younger at earlier times, and it also appears that bulge growth may trail behind black hole growth at early times. However, the evolutionary corrections are highly uncertain. Recent work (Cisternas et al. 2011; Merloni et al. 2010; Bennert et al. 2011b) suggests that the relationship between the central black hole mass and the *total* stellar mass of the host galaxy does not evolve to $z \sim 2$. Other groups find that the relation evolves by a factor of $\sim 2 - 4$ to $z \sim 2$ (Trakhtenbrot & Netzer 2010), but the highest-redshift measurement of a single black hole with spatially-resolved spectroscopy (to date; Inskip et al. 2011) is consistent with the local black hole-galaxy relation.

There are therefore many sources of uncertainty in the estimation of $z \sim 2$ black hole masses using galaxy-black hole correlations. In order to accurately characterize the uncertainties of our estimated black hole masses, we calculate black hole masses from host galaxy stellar masses via Monte Carlo simulations that account for the uncertainties in each quantity involved in the calculation as well as the scatter in the black hole mass-host stellar mass correlation of Häring & Rix (2004). We simulate 10^5 observations via Gaussian-random sampling within the uncertainties for each source and report the median black hole masses and 1σ widths of the distributions of each source as our uncertainties.

Table 4.1 gives the black hole mass estimates for each of our sources. We find that the black hole masses span a large range, from $2^{+19}_{-1.5} \times 10^5 M_\odot$ to $2^{+21}_{-1.8} \times 10^9 M_\odot$, with median and mean masses of $4 \times 10^7 M_\odot$ and $3 \times 10^7 M_\odot$, respectively. Typical uncertainties are -0.7 and $+1.0$ dex, with asymmetries in the uncertainties primarily due to uncertainties in the host stellar masses, which are also calculated by Monte Carlo methods (Kriek et al. 2009).

In addition to black hole masses, bolometric (total) luminosities are useful quantities because they allow for an estimate of the mass accretion rate onto the black hole (modulo

the radiative efficiency). Simmons et al. (2011) have shown that the model-dependent bolometric corrections to the hard X-ray luminosity of Treister et al. (2009) are in very good agreement with bolometric luminosities recovered for obscured AGN by leveraging the observed point-source luminosities to extract the SEDs from the far-infrared to X-ray of each AGN. We therefore use the absorption-corrected X-ray luminosity of each source, along with the bolometric corrections of Treister et al. (2009), to estimate the bolometric luminosities of each source. Given the X-ray luminosities in the sample, the bolometric correction ranges from 25 to 76.

With estimates of both bolometric luminosity and black hole mass, we explore the growth rates of the black holes in the sample in Figure 4.5. The growth rates of moderate-luminosity AGN at $z \sim 2$ span several orders of magnitude, from super-Eddington accretion to $10^{-3} L_{Edd}$, with average and median L/L_{Edd} values of 0.06 and 0.05, respectively. One-quarter of the sample (19 of 57 AGN) has $L/L_{Edd} < 0.01$; 21 AGN have $0.01 \leq L/L_{Edd} \leq 0.1$. The sample cannot therefore be characterized by a single growth rate/Eddington ratio, but approximately 60% of the sample is growing at less than 10% of the Eddington (maximum) rate.

4.4   Discussion

Because moderate-luminosity AGN far outnumber more luminous objects like quasars, they make up a large fraction of black hole growth in the universe (Hasinger et al. 2005). They therefore represent the most common mode of black hole feeding that we can observe, and their feedback mechanism(s) represents the typical means of black hole-galaxy co-evolution.

The host galaxies of the sample are generally characterized by strong disk contributions. Fully half of the sample of host galaxies is consistent with having less than 20%
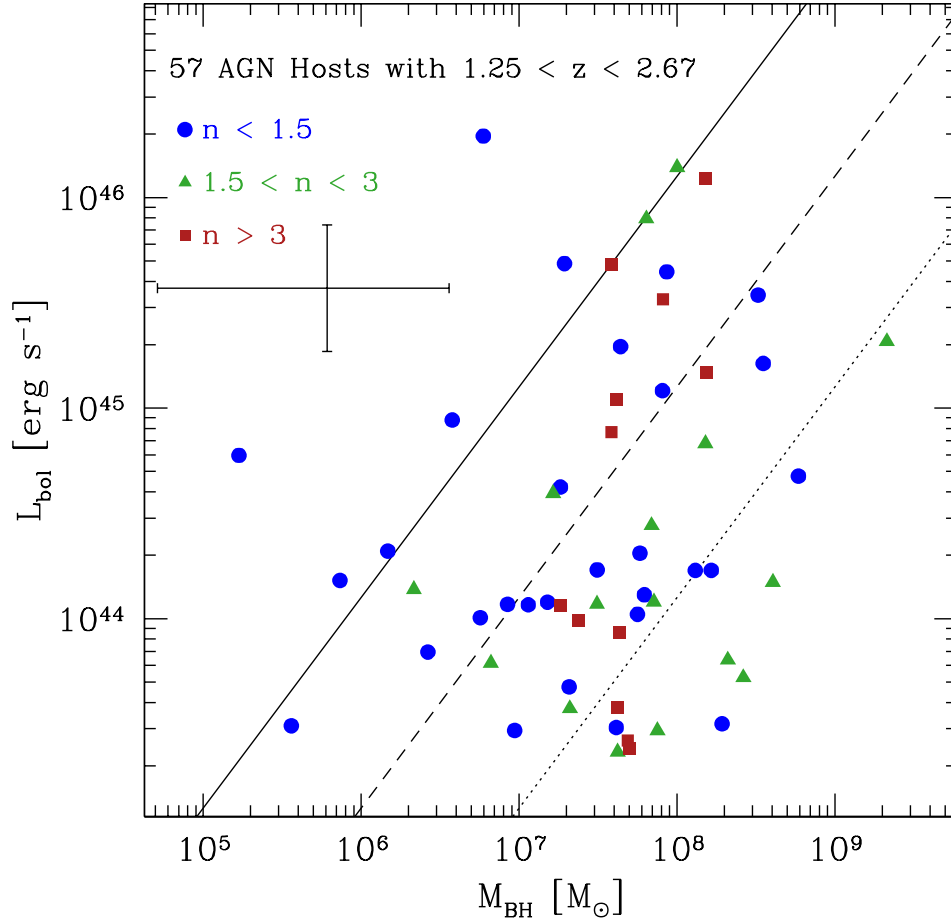
Fig. 4.5.— Bolometric luminosity vs. black hole mass for AGN in disk-dominated (blue circles), intermediate (green triangles) and strong-bulge (red squares) host galaxies at $1.25 < z < 2.7$ in this sample. Lines shown indicate constant Eddington ratio: $L = L_{Edd}$ (solid line), $L = 0.1 L_{Edd}$ (dashed line), and $L = 0.01 L_{Edd}$ (dotted line). Growing black holes at these redshifts span three orders of magnitude of growth rate, from Eddington-limited (and possibly super-Eddington) rates to highly sub-Eddington. One-third of the sample has $L/L_{Edd} \leq 0.01$; another $\sim 30\%$ have $0.01 \leq L/L_{Edd} \leq 0.1$. Bolometric luminosity is uncorrelated with host galaxy morphology.

bulge contribution, and a further one-quarter of the AGN are hosted in galaxies with be-tween 20 and 65% of their light from a bulge. Very few host galaxies in the sample are unambiguously consistent with the label "bulge-dominated": Simmons & Urry (2008) showed that even a host galaxy with a fitted Sérsic index of $n \geq 4$ (traditionally asso-ciated with a pure bulge or elliptical; there are 8 in the sample) may have a strong disk contribution (up to 45% in some cases). Non-detection of a bulge, on the other hand, is a reliable result according to multiple sets of host galaxy simulations (Sánchez et al. 2004; Simmons & Urry 2008; Gabor et al. 2009; Pierce et al. 2010a).

That 75% of moderate-luminosity $z \sim 2$ AGN hosts in the CDF-S have strong disk components agrees quantitatively with the pilot study of Schawinski et al. (2011). Using visual classifications, Kocevski et al. (2011) find a slightly lower fraction of disks (51%). However, visual classifications of host galaxies with even faint central nuclear emission may be biased toward recovering more bulge-like host morphologies (Simmons et al. 2012, in preparation). Given that 90% of moderate-luminosity AGN+hosts at $z \sim 2$ have detected central point sources, the disk fraction of the Kocevski et al. sample should be considered a lower limit.

The high fraction of disky morphologies in moderate-luminosity AGN hosts at $z \sim 2$ (Figure 4.2) means the majority of the host galaxies in the sample have assembled without building up prominent bulges or disrupting their dominant disks. This implies that major mergers, which tend to destroy disks and lead to elliptical morphologies (e.g., Toomre 1977; Walker et al. 1996; Martig et al. 2012), play a small role in the growth of these galaxies and their central black holes. Those galaxies that appear to be highly disturbed also do not host the highest-luminosity AGN, as might be expected if the processes that disrupted the host also fed large amounts of material onto the black hole. Black hole-galaxy co-evolution scenarios in which major mergers trigger accretion onto the central supermassive black hole (Sanders et al. 1988; Di Matteo et al. 2005;

Hopkins et al. 2006a), leading from an Eddington-limited quasar phase in a merger remnant host to a longer phase of slow black hole growth with a moderate- or low-luminosity AGN hosted by an elliptical galaxy, are inconsistent with the morphologies of moderate-luminosity AGN hosts at this early epoch.

Disk-dominated hosts are more likely to be observed as blue than bulges: although there are a substantial number of intrinsically red disks in the sample, uncorrected colors of the sub-samples with $n < 1.5$ and $n > 3$ are different at the 99% level, according to a K-S test. However, this difference disappears once the dust correction is applied, primarily because several of the strong-bulge hosts appear to be intrinsically blue, but dust-reddened. Blue early-type galaxies have also been seen for AGN hosts in other surveys at lower redshifts (Sánchez et al. 2004; Pierce et al. 2010b; Cardamone et al. 2010).

However, the rest-frame $U - V$ colors of $z \sim 2$ AGN hosts are not uniformly consistent with the "blue cloud" population at the same redshift, as expected from galaxy formation simulations where mergers trigger black hole growth and a burst of star formation (Hopkins et al. 2006b; Somerville et al. 2008). Even after a dust correction is applied, $\sim 50\%$ of host galaxies are red, in both redshift bins.

Merger scenarios tying the evolutionary stage of a post-merger to the decaying accretion rate of its central supermassive black hole also predict a correlation between AGN luminosity and host galaxy morphology. However, $z \sim 2$ AGN bolometric luminosity does not depend on host galaxy morphology: as seen in Figure 4.5, black holes growing at or near the Eddington limit are found in disk-dominated, intermediate, and strong-bulge host galaxies, as are the slowest-growing black holes in the sample.

Nor does the bolometric luminosity depend on redshift: black holes at all redshifts in the sample grow at all rates we are able to detect. In Figure 4.6 we show the bolometric luminosity versus redshift for the moderate-luminosity AGN in this sample. We also

plot the flux limit of the sample, which defines a redshift-dependent lower limit to the bolometric luminosity.

Figure 4.6 shows that the observed AGN populate every part of the parameter space that we do not select against. The range of AGN luminosities sampled implies a range of mass accretion rates spanning over two orders of magnitude. For an assumed radiative efficiency of $\epsilon = 0.15$ (Elvis et al. 2002), the black holes in the sample are growing at a rate of no more than $\sim 2 M_\odot$ per year for the highest-luminosity black hole. Lower accretion rates are more typical of the sample, with the average and median values being 0.03 and $0.02 M_\odot$ yr^{-1}, respectively, and the lowest-luminosity AGN in the sample accreting at $0.003 M_\odot$ yr^{-1}.

Such characteristically low mass accretion rates imply that slow- and moderate-growth periods of a typical supermassive black hole do not require large, bulk flows of matter into the central region of the host galaxy, as one might expect from merger-triggered gas infall. Indeed, the median rate of $0.02 M_\odot$ yr^{-1} is roughly consistent with expected stellar mass loss from a passively evolving stellar population (Ciotti et al. 1991; for a recent treatment, see Ciotti & Ostriker 2012).

4.5   Conclusions

We describe 57 AGN host galaxies from $1.25 \leq z \leq 2.67$ in the GOODS-South field selected from the 4 Ms X-ray catalogs of Xue et al. (2011). Using *HST* WFC3/IR $F125W$ and $F160W$ images from CANDELS, we perform parametric morphological fits in the rest-frame B band. We additionally calculate stellar masses, black hole masses, bolometric AGN luminosities, and rest-frame host galaxy $(U - V)$ colors for each source.

Our major results are as follows:

- Host galaxy morphologies span a range from disk-dominated to bulge-dominated,
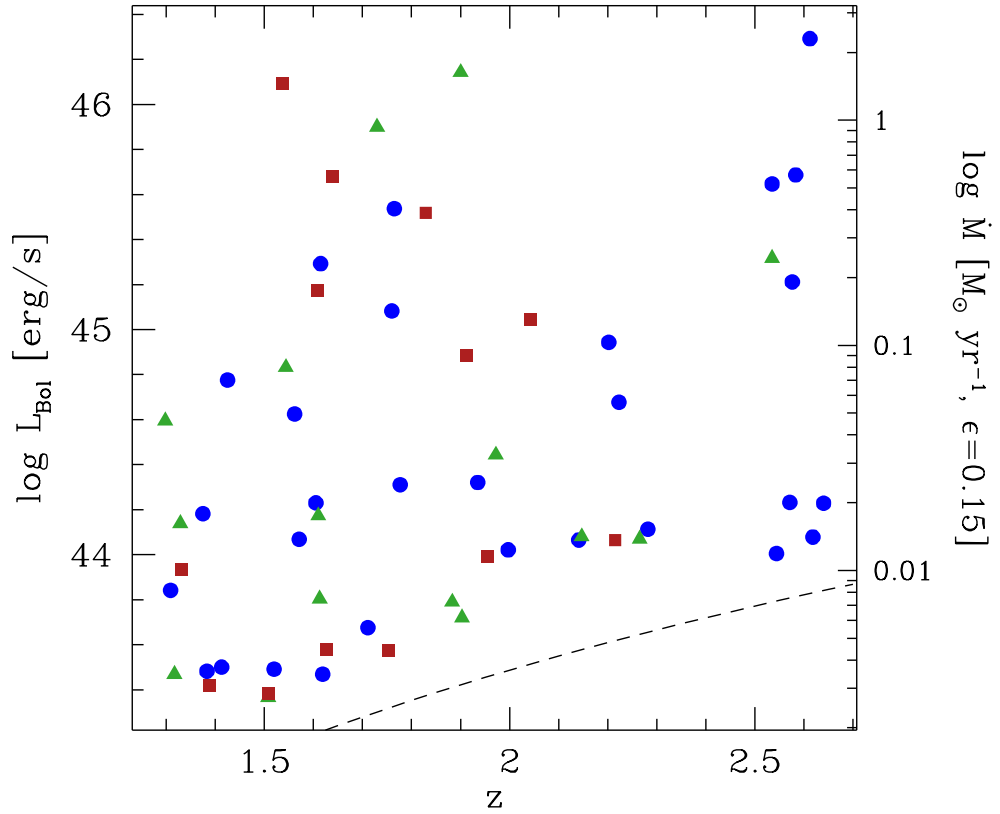
Fig. 4.6.— Bolometric luminosity vs. redshift for moderate-luminosity AGN in the CANDELS/GOODS-S field. Given the conversion of the X-ray flux limit of the Xue et al. (2011) survey (dashed line) to a bolometric limit, our sources fill the observable area. The bolometric luminosity is converted into a mass accretion rate on the right vertical axis, assuming a radiative efficiency of $\epsilon = 0.15$ (Elvis et al. 2002).

but approximately 50% of the sample is unambiguously disk-dominated, and another $\sim 25\%$ of the host sample have fitted Sérsic indices consistent with strong (if not dominant) disk components.

- Host morphologies are statistically indistinguishable between two redshift bins of approximately equal time intervals ($\Delta t \approx 1.3$ Gyr; $1.25 < z < 1.76$ and $1.76 < z < 2.67$).

- Uncorrected host galaxy colors between the two redshift bins do appear different, with blue colors more likely at higher redshifts, but the significance of this difference is reduced (from $\approx 97\%$ to $\approx 74\%$ according to a K-S test) once a dust correction is applied.

- We detect central point sources in the rest-frame B band to at least 3σ in 90% of sources. The majority of detections are greater than 5σ.

- Central black hole masses, estimated from stellar masses, span a wide range (from $10^5 - 10^9 M_\odot$), with a median mass of $4 \times 10^7 M_\odot$.

- AGN bolometric luminosities range from 2×10^{43} to 2×10^{46} erg s^{-1}; this is limited only by the flux limits of the 4 Ms *Chandra* data and expected detection numbers based on the AGN luminosity function at these redshifts (Croom et al. 2004). Essentially, we find AGN accreting at all levels we are capable of detecting, with no redshift trend.

- AGN bolometric luminosity is uncorrelated with host stellar mass, color or morphology, in contrast to the predictions of some models of merger-driven accretion.

Moderate-luminosity AGN, which collectively comprise a substantial fraction of total black hole growth at these redshifts, span several orders of magnitude in growth rate

and are hosted by galaxies with a range of star formation rates, as indicated by a range of dust-corrected colors. While their host galaxies also span a range of morphologies, strong disks dominate. That fully half of growing black holes at these luminosities are hosted in galaxies with a (conservative) minimum of 80% of their optical light coming from an undisturbed disk likely indicates the importance of secular processes and minor mergers (that do not produce a significant bulge) in the co-evolution of black holes and galaxies.

Table 4.1:: GOODS AGN sample with point source and host galaxy fits, X-ray and bolometric luminosities, host stellar masses and black hole masses for AGN+hosts between $1.25 < z < 2.67$.

	Optical Position				Rest-frame B		$\log L$ [erg/s]		$\log M$ [M$_\odot$]	
ID[a]	RA	DEC	z	Sérsic n	$\log L_{\mathrm{PS}}/L_{\mathrm{Host}}$	PS Signif. (σ)	L_X	L_{bol}	Host M_*	M_{BH}
121	53.026794	-27.765278	1.33	$2.13^{+0.34}_{-0.34}$	-1.15 ± 0.77	5	42.61	44.14	$9.12^{+1.98}_{-0.51}$	$6.34^{+2.13}_{-0.70}$
137	53.033417	-27.782642	2.61	$0.88^{+0.34}_{-0.34}$	-0.75 ± 0.73	> 5	44.41	46.29	$9.49^{+1.35}_{-0.66}$	$6.78^{+1.47}_{-0.84}$
155	53.040958	-27.836111	1.93	$0.34^{+0.27}_{-0.27}$	-0.05 ± 0.24	> 5	42.76	44.32	$8.97^{+1.30}_{-0.56}$	$6.17^{+1.41}_{-0.74}$
163	53.044960	-27.774416	1.61	$1.56^{+0.29}_{-0.29}$	-1.41 ± 0.62	> 5	42.64	44.17	$11.20^{+0.47}_{-0.26}$	$8.61^{+0.53}_{-0.37}$
184	53.052288	-27.774778	1.61	$1.40^{+0.33}_{-0.33}$	-1.18 ± 0.77	> 5	42.69	44.23	$10.84^{+0.43}_{-0.18}$	$8.22^{+0.47}_{-0.31}$
185	53.052372	-27.827280	2.15	$1.54^{+0.44}_{-0.44}$	-0.84 ± 0.73	> 5	42.56	44.08	$10.52^{+1.53}_{-1.35}$	$7.85^{+1.72}_{-1.54}$
199	53.057919	-27.833555	2.54	$1.79^{+0.26}_{-0.26}$	-1.61 ± 0.48	> 5	43.60	45.32	$11.81^{+0.93}_{-0.63}$	$9.33^{+1.04}_{-0.76}$
202	53.058956	-27.819613	2.14	$1.01^{+0.36}_{-0.36}$	-0.64 ± 0.71	> 5	42.55	44.07	$9.83^{+0.81}_{-0.82}$	$7.06^{+0.92}_{-0.95}$

Continued on Next Page...

Table 4.1 – Continued

	Optical Position				Rest-frame B		$\log L$ [erg/s]		$\log M$ [M$_\odot$]	
ID[a]	RA	DEC	z	Sérsic n	$\log L_{\mathrm{PS}}/L_{\mathrm{Host}}$	PS Signif. (σ)	L_X	L_{bol}	Host M_*	M_{BH}
205	53.060123	-27.853054	1.54	$2.83^{+0.30}_{-0.30}$	-0.95 ± 0.74	> 5	43.19	44.83	$10.87^{+0.41}_{-0.51}$	$8.18^{+0.50}_{-0.59}$
211	53.061958	-27.851082	1.83	$6.76^{+0.84}_{-0.84}$	-1.29 ± 0.71	> 5	43.76	45.52	$10.53^{+1.12}_{-0.39}$	$7.91^{+1.20}_{-0.54}$
221	53.065670	-27.879000	1.97	$2.20^{+0.29}_{-0.29}$	-0.56 ± 0.70	5	42.87	44.44	$10.45^{+1.01}_{-0.30}$	$7.84^{+1.08}_{-0.46}$
225	53.066292	-27.800610	1.52	$0.90^{+1.39}_{-0.86}$	$\cdots$	< 1	42.07	43.49	$8.51^{+1.73}_{-1.61}$	$5.56^{+1.94}_{-1.83}$
226	53.066837	-27.816639	1.41	$0.58^{+0.32}_{-0.32}$	-1.13 ± 0.76	> 5	42.08	43.50	$11.00^{+0.60}_{-1.14}$	$8.29^{+0.73}_{-1.26}$
231	53.068459	-27.866526	2.20	$1.18^{+0.64}_{-0.64}$	0.05 ± 0.20	> 5	43.28	44.94	$9.35^{+1.33}_{-0.81}$	$6.58^{+1.46}_{-0.98}$
242	53.071621	-27.769861	1.33	$8.74^{+0.47}_{-0.47}$	$\cdots$	2	42.44	43.93	$10.39^{+0.80}_{-0.80}$	$7.64^{+0.91}_{-0.91}$
244	53.072121	-27.819002	2.28	$0.76^{+0.20}_{-0.20}$	$\cdots$	1	42.59	44.11	$10.36^{+1.69}_{-0.39}$	$7.79^{+1.80}_{-0.59}$
247	53.074337	-27.869667	1.88	$2.22^{+0.30}_{-0.30}$	-1.49 ± 0.57	> 5	42.32	43.79	$9.58^{+1.89}_{-1.04}$	$6.82^{+2.08}_{-1.24}$
257	53.076458	-27.848778	1.54	$3.31^{+0.33}_{-0.33}$	-1.08 ± 0.76	> 5	44.24	46.09	$10.82^{+0.33}_{-0.17}$	$8.18^{+0.38}_{-0.29}$
288	53.086922	-27.873026	1.42	$0.79^{+1.54}_{-0.75}$	-0.90 ± 0.85	> 5	43.14	44.78	$8.21^{+0.97}_{-0.81}$	$5.23^{+1.09}_{-0.96}$
293	53.088795	-27.850554	1.57	$0.53^{+0.26}_{-0.26}$	-0.64 ± 0.71	> 5	42.55	44.07	$9.66^{+1.03}_{-0.33}$	$6.93^{+1.10}_{-0.49}$
296	53.090752	-27.782528	1.56	$0.39^{+0.30}_{-0.30}$	-0.89 ± 0.74	> 5	43.02	44.62	$9.99^{+1.37}_{-0.63}$	$7.26^{+1.49}_{-0.78}$

Continued on Next Page. . .

Table 4.1 – Continued

	Optical Position				Rest-frame B		$\log L$ [erg/s]		$\log M$ [M$_\odot$]	
ID[a]	RA	DEC	z	Sérsic n	$\log L_{\mathrm{PS}}/L_{\mathrm{Host}}$	PS Signif. (σ)	L_X	L_{bol}	Host M_*	M_{BH}
301	53.092419	-27.803249	1.76	$1.27^{+0.32}_{-0.32}$	-1.34 ± 0.67	> 5	43.40	45.08	$10.63^{+0.89}_{-1.26}$	$7.91^{+1.04}_{-1.40}$
305	53.093834	-27.801357	1.91	$3.63^{+1.34}_{-1.34}$	-0.98 ± 0.80	3	43.24	44.89	$10.41^{+0.63}_{-2.75}$	$7.59^{+0.82}_{-3.00}$
308	53.094002	-27.767834	1.73	$2.65^{+0.85}_{-0.85}$	-0.60 ± 0.71	> 5	44.08	45.90	$10.57^{+0.50}_{-1.04}$	$7.81^{+0.63}_{-1.13}$
310	53.094086	-27.804220	2.54	$0.99^{+0.29}_{-0.29}$	-0.89 ± 0.74	> 5	43.87	45.65	$10.52^{+1.60}_{-0.68}$	$7.94^{+1.75}_{-0.86}$
325	53.099957	-27.808554	2.22	$8.78^{+1.19}_{-1.19}$	-0.62 ± 0.71	> 5	42.55	44.06	$9.92^{+1.10}_{-0.39}$	$7.26^{+1.18}_{-0.56}$
337	53.103535	-27.847334	2.27	$1.97^{+0.33}_{-0.33}$	-1.25 ± 0.74	> 5	42.55	44.07	$10.13^{+1.07}_{-0.37}$	$7.49^{+1.15}_{-0.54}$
360	53.108372	-27.797722	1.71	$0.11^{+0.28}_{-0.07}$	-0.78 ± 0.72	> 5	42.22	43.68	$10.04^{+1.10}_{-0.65}$	$7.32^{+1.21}_{-0.79}$
389	53.119244	-27.765888	1.63	$3.35^{+0.54}_{-0.54}$	$\cdots$	< 1	42.14	43.58	$10.32^{+1.20}_{-0.72}$	$7.62^{+1.32}_{-0.87}$
394	53.120205	-27.798887	1.38	$0.73^{+0.31}_{-0.31}$	-1.08 ± 0.76	> 5	42.06	43.48	$10.31^{+0.62}_{-0.25}$	$7.62^{+0.67}_{-0.38}$
428	53.129620	-27.827780	1.51	$1.81^{+0.59}_{-0.59}$	-0.70 ± 0.74	> 5	41.96	43.37	$10.35^{+0.72}_{-0.57}$	$7.62^{+0.81}_{-0.68}$
435	53.131165	-27.773222	2.22	$1.27^{+0.24}_{-0.24}$	-0.44 ± 0.63	> 5	43.06	44.68	$11.43^{+0.35}_{-0.92}$	$8.77^{+0.51}_{-0.99}$
436	53.131287	-27.841389	1.61	$2.77^{+0.35}_{-0.35}$	-1.84 ± 0.34	> 5	42.33	43.80	$10.94^{+0.70}_{-0.37}$	$8.32^{+0.77}_{-0.49}$
437	53.131454	-27.814999	1.78	$0.21^{+0.18}_{-0.17}$	$\cdots$	< 1	42.75	44.31	$10.46^{+1.03}_{-0.82}$	$7.77^{+1.16}_{-0.96}$

Continued on Next Page...

Table 4.1 – Continued

	Optical Position				Rest-frame B		$\log L$ [erg/s]		$\log M$ [M$_\odot$]	
ID[a]	RA	DEC	z	Sérsic n	$\log L_{\mathrm{PS}}/L_{\mathrm{Host}}$	PS Signif. (σ)	L_X	L_{bol}	Host M_*	M_{BH}
451	53.137287	-27.844805	2.62	$0.95^{+0.31}_{-0.31}$	-1.05 ± 0.76	4	42.56	44.08	$9.84^{+0.66}_{-0.26}$	$7.18^{+0.71}_{-0.44}$
462	53.140289	-27.797556	1.39	$7.47^{+1.00}_{-1.00}$	-0.66 ± 0.71	>5	42.01	43.42	$10.44^{+0.48}_{-0.58}$	$7.69^{+0.57}_{-0.67}$
463	53.140999	-27.766834	1.90	$2.47^{+0.27}_{-0.27}$	-0.63 ± 0.70	>5	42.26	43.72	$11.00^{+0.67}_{-0.30}$	$8.42^{+0.73}_{-0.43}$
464	53.141037	-27.755833	2.04	$6.37^{+0.81}_{-0.81}$	-1.27 ± 0.73	>5	43.37	45.04	$10.36^{+0.92}_{-1.34}$	$7.62^{+1.07}_{-1.49}$
482	53.146084	-27.780027	2.64	$1.20^{+0.34}_{-0.34}$	-1.19 ± 0.78	5	42.69	44.23	$10.70^{+1.60}_{-0.85}$	$8.12^{+1.74}_{-1.03}$
490	53.148834	-27.821222	2.58	$0.51^{+0.29}_{-0.29}$	-0.92 ± 0.74	>5	43.51	45.21	$11.11^{+1.26}_{-0.89}$	$8.55^{+1.41}_{-1.05}$
493	53.149918	-27.814083	1.31	$0.72^{+0.28}_{-0.28}$	-0.84 ± 0.73	>5	42.36	43.84	$9.29^{+0.14}_{-0.10}$	$6.42^{+0.24}_{-0.23}$
498	53.150707	-27.843723	1.61	$3.54^{+0.33}_{-0.33}$	-1.02 ± 0.75	>5	43.47	45.17	$10.82^{+0.72}_{-0.37}$	$8.19^{+0.79}_{-0.49}$
501	53.150791	-27.774445	2.57	$0.74^{+0.32}_{-0.32}$	-1.13 ± 0.76	>5	42.69	44.23	$10.14^{+1.41}_{-0.65}$	$7.50^{+1.55}_{-0.82}$
504	53.151455	-27.825945	1.51	$6.82^{+0.70}_{-0.70}$	-1.07 ± 0.76	>5	41.98	43.38	$10.39^{+0.85}_{-0.48}$	$7.70^{+0.93}_{-0.60}$
517	53.157288	-27.833723	1.62	$0.31^{+0.29}_{-0.27}$	-0.87 ± 0.73	>5	42.05	43.47	$9.73^{+0.92}_{-0.48}$	$6.97^{+1.01}_{-0.62}$
525	53.160500	-27.776361	2.54	$0.80^{+0.27}_{-0.27}$	-0.66 ± 0.71	>5	42.50	44.00	$9.47^{+1.31}_{-0.59}$	$6.76^{+1.42}_{-0.77}$
545	53.165207	-27.785999	1.32	$2.30^{+0.38}_{-0.38}$	-1.21 ± 0.77	>5	42.05	43.47	$10.54^{+0.60}_{-0.21}$	$7.88^{+0.64}_{-0.34}$

Table 4.1 – Continued

	Optical Position				Rest-frame B		$\log L$ [erg/s]		$\log M$ [M$_\odot$]	
ID[a]	RA	DEC	z	Sérsic n	$\log L_{\rm PS}/L_{\rm Host}$	PS Signif. (σ)	L_X	L_{bol}	Host M_*	M_{BH}
549	53.165585	-27.769861	1.76	$1.03^{+0.33}_{-0.33}$	-1.20 ± 0.77	> 5	43.78	45.54	$11.16^{+0.54}_{-0.70}$	$8.51^{+0.65}_{-0.79}$
552	53.166874	-27.798834	2.00	$0.76^{+0.32}_{-0.32}$	-1.13 ± 0.77	> 5	42.51	44.02	$10.38^{+0.87}_{-0.31}$	$7.75^{+0.93}_{-0.46}$
557	53.170666	-27.741056	1.30	$2.07^{+0.28}_{-0.28}$	-0.77 ± 0.72	5	42.99	44.60	$9.98^{+0.75}_{-0.47}$	$7.22^{+0.83}_{-0.59}$
575	53.179371	-27.812611	1.64	$5.53^{+0.51}_{-0.51}$	-0.94 ± 0.74	> 5	43.90	45.68	$10.27^{+0.66}_{-0.31}$	$7.58^{+0.72}_{-0.44}$
577	53.180168	-27.820696	1.90	$2.79^{+0.29}_{-0.29}$	-0.71 ± 0.71	> 5	44.29	46.14	$10.62^{+0.57}_{-0.23}$	$8.00^{+0.62}_{-0.37}$
579	53.181038	-27.817280	1.75	$5.50^{+0.31}_{-0.31}$	$\cdots$	< 1	42.14	43.57	$10.03^{+1.12}_{-0.53}$	$7.32^{+1.22}_{-0.68}$
589	53.185040	-27.819805	1.95	$3.86^{+0.54}_{-0.54}$	-1.36 ± 0.66	> 5	42.49	43.99	$10.10^{+1.51}_{-1.32}$	$7.38^{+1.69}_{-1.51}$
593	53.185875	-27.810055	2.58	$1.37^{+0.77}_{-0.77}$	-0.18 ± 0.38	4	43.90	45.69	$10.06^{+0.80}_{-1.28}$	$7.29^{+0.96}_{-1.42}$
625	53.198872	-27.844002	1.62	$1.10^{+0.31}_{-0.31}$	-1.06 ± 0.76	> 5	43.58	45.29	$10.30^{+1.37}_{-0.44}$	$7.64^{+1.49}_{-0.59}$
656	53.218037	-27.761694	1.38	$1.26^{+0.28}_{-0.28}$	-0.83 ± 0.73	> 5	42.65	44.18	$8.80^{+0.23}_{-0.23}$	$5.87^{+0.33}_{-0.34}$

[a]X-ray IDs from Xue et al. (2011)

Chapter 5

Conclusions

5.1   Summary and Discussion

Studying growing black holes and the galaxies that host them out to the peak of the activity of both AGN and star formation requires a balanced approach combining data from deep multi-wavelength surveys and in-depth analysis of simulated AGN+hosts in order to understand the results.

The simulations in this thesis show that we can reliably separate AGN from host galaxy at moderate redshifts and within a wide range of host-to-AGN luminosity ratios. A lack of detection of a point source is a robust result regardless of the host galaxy morphology. The rate of spurious point-source detection, on the other hand, is morphologically dependent: while detected point sources are likely real when they are relatively bright compared to the host galaxy, the likelihood of a detected fainter point source being real is lower for an intrinsically bulge-dominated galaxy than for a disk-dominated galaxy.

Recovery of morphological parameters is very robust for single-Sérsic fits. For two-component galaxies having a bulge and a disk, the picture is somewhat more complex.

146

Two-component fits are statistically reliable for a large sample, but individually, automated fits have an uncertainty in B/Tot of $\sim 50\%$. The Sérsic index maps to the bulge-to-total ratio at all redshifts, but the relationship is quite shallow, so given the uncertainties the mapping is not 1:1. Nevertheless, it is generally possible to constrain the bulge-to-total ratio to a range of likely parameters given a fitted Sérsic index (see Table 2.4). If a galaxy fits with $n < 1.5$ it is unambiguously disk-dominated, but may have a small bulge contribution ($\lesssim 20\%$). If a galaxy fits with $n > 4$, it is most likely bulge-dominated, but may still have a significant disk ($\lesssim 45\%$). Galaxies with fitted Sérsic values of $3 < n < 4$ are still likely to be bulge-dominated, but may have a slightly stronger disk contribution. Galaxies with $1.5 < n < 3$ have intermediate morphologies likely indicative of the presence of a bulge and a disk in roughly equal amounts, but this can vary within $0.2 < (B/Tot) < 0.65$. The presence of a central active nucleus increases the uncertainties in recovered fit parameters, but fitted host galaxy and AGN parameters are generally reliable and do indeed map to intrinsic parameters.

The results of the AGN host galaxy simulations were used to inform the rest of the analysis in this thesis, namely the study of AGN (selected via their hard X-ray emission; Alexander et al. 2003; Xue et al. 2011) and their host galaxies from $0.25 < z < 2.67$. This redshift range, which spans ~ 8 Gyr of cosmic time, was observed in the rest-frame optical by *HST* using the ACS ($BVIz$ bands) and WFC3 (JH) bands. Owing to the two different instruments and particularly to the fact that, at the time of this thesis, deep WFC3 data was available for only the CDF-S, the analysis was separated into two chapters. The first of these (Chapter 2) describes analysis of 87 AGN and their host galaxies with $0.25 \leq z \leq 1.25$ in the CDF-S and CDF-N fields (320 square arcminutes) and observed using ACS. Because the survey is sensitive to moderate AGN luminosities yet the galaxies (and therefore their central black holes) are massive, the majority of these moderate-luminosity AGN are in a slow-growth phase, having already reached

high typical black hole masses. Most of the sample is accreting considerably less than $1 M_\odot \ \mathrm{yr}^{-1}$, implying higher growth rates must have been typical for the sample at earlier times in order for them to have grown to the masses at which they are observed in the age of the universe to that point.

The morphologies of the host galaxies are roughly an equal mix of bulge-dominated, intermediate, and disk-dominated systems. Because major mergers destroy disks, neither the disk-dominated nor the intermediate sub-samples are consistent with a history of major mergers: approximately two-thirds of the hosts of moderate-luminosity AGN at $0.25 < z < 1.25$ have massive black holes whose growth history is dominated by some other mechanism. At some point in the past these black holes must have been accreting at higher rates, but the material feeding them was typically not driven inward by major mergers, because such mergers would have destroyed the disks that dominate one-third of the sample and are strongly present (if not dominant) in another one-third. This finding is also consistent with the results of other work at $z \lesssim 1$ (Grogin et al. 2005; Ballo et al. 2007; Pierce et al. 2007; Gabor et al. 2009; Cisternas et al. 2011) using multiple different techniques to compare AGN host galaxies to inactive galaxies and finding no increased incidence of ongoing merger signatures among the AGN hosts. Mergers do not preferentially trigger activity in moderate-luminosity AGN at $z \sim 1 - 2$ on timescales short enough for direct signatures of the merger to still be visible, nor have they triggered activity in the past for a majority of this sample.

Direct examination of the more distant past weakens even further the case for major mergers as an important pathway for the growth of supermassive black holes. Examination of 57 AGN+host galaxies in the deep WFC3 data available for the CDF-S reveals that fully half of the host galaxy sample at $1.25 < z < 2.67$ is unambiguously disk-dominated, with another one-quarter of the sample having intermediate morphologies (i.e., strong disks). Even less of the $z \sim 2$ sample is consistent with past or ongoing

major mergers than the $z \sim 1$ sample. Studies that compare to inactive galaxies at these redshifts (Schawinski et al. 2011; Kocevski et al. 2011) find similar results. Given the fact that AGN at the luminosities probed by the two sets of observations in this thesis collectively contribute at least half of the AGN emission at these redshifts (See Figure 1.1 in this thesis; Hasinger et al. 2005), this work makes clear that major mergers are not a major pathway to the co-evolution of black holes and galaxies for these most common of growing black holes.

The only limits to black hole accretion rates seen in these samples are the limits provided by the Eddington limit on the maximum luminosity for a given black hole mass and the lower limits from X-ray flux limits. We observe AGN at all luminosities at which we are able to detect them (a result echoed by others, e.g., Woo & Urry 2002; Aird et al. 2012). Additionally, the host morphologies of moderate-luminosity AGN are not correlated with bolometric AGN luminosity across the range of redshifts probed by this study. In other words, black hole mass may be correlated with galaxy mass, but within this sample, the accretion rate onto the black hole is not tied to the type of galaxy providing material to the black hole.

The redshift range spanned by the collective sample in this thesis covers more than half the Hubble time, and with the exception of the lowest redshifts ($0.25 < z < 0.47$, covering the smallest volume in the pencil-beam fields) the sample is large enough to allow examination of the evolution of host galaxy morphology in multiple redshift bins. Figure 5.1 shows the evolution of the morphological mix of host galaxies of moderate-luminosity AGN in the combined samples of Chapters 3 and 4. The redshift bins are selected to cover 5 equal-length epochs ($\Delta t \approx 1.3$ Gyr). The disk-dominated fraction is highest at the earliest times, and steadily evolves from $\approx 60\%$ in the bin covering $1.76 < z < 2.67$ to $\lesssim 20\%$ in the lowest-redshift bin, $0.47 < z < 0.66$. The fractions of intermediate and bulge-dominated host galaxies increase by roughly equal amounts

over this redshift range.

This result is qualitatively consistent with results showing that the morphological fraction of inactive galaxies becomes less bulge-dominated at higher redshifts (even for massive galaxies; Buitrago et al. 2011). A full comparison to flux-limited (and even volume-limited) samples of inactive galaxies (e.g., Ravindranath et al. 2004; Grogin et al. 2005) is difficult owing to the strong dependence of morphology on stellar mass and color. Studies examining AGN hosts versus inactive galaxies for mass- and redshift-matched samples use independent methods but find that inactive galaxies are generally similar to host galaxies to $z \sim 3$ (Schawinski et al. 2011; Kocevski et al. 2011; Rosario et al. 2011). However, only the smallest of these samples performs a full host-point source decomposition, which is an important (if time-consuming) step: $\sim 90\%$ of moderate-luminosity X-ray selected AGN+host galaxies have detected nuclear point sources, and nuclear point sources can influence both parametric and visual morphological classification. Detailed analysis with quantitative host-AGN decomposition is required in future work in order to accurately compare AGN host galaxies to inactive galaxies. In particular, such work may benefit from high-resolution analysis at $z < 2$ in rest-frame V and even I bands, which is now possible using the J and H bands on the *HST* WFC3 instrument.

5.2   Future Directions

This thesis has shown that mergers do not dominate one of the primary modes of black hole growth from $0.25 < z < 2.67$, raising the question: what *is* the most important pathway to the growth of supermassive black holes?

Although a large proportion of the host galaxies in this thesis have morphologies inconsistent with a history involving a major merger, minor mergers remain a likely
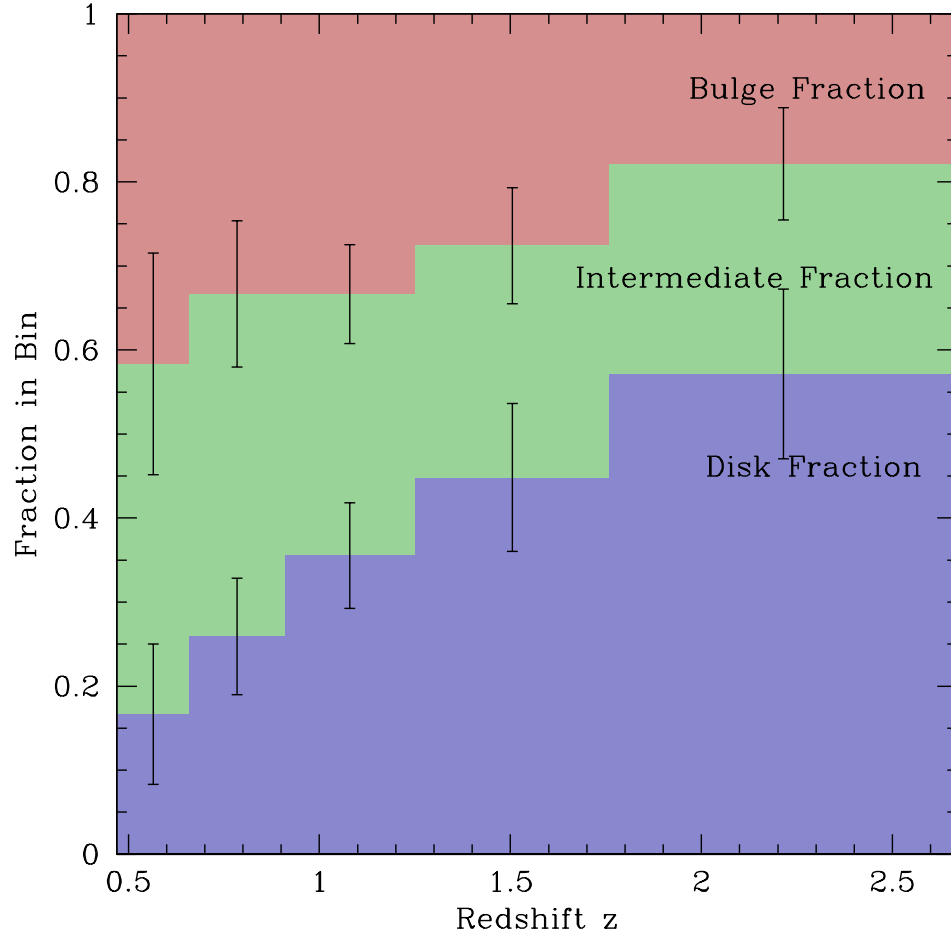
Fig. 5.1.— Morphological fractions in five redshift bins from $0.25 \leq z \leq 2.67$. Disk-dominated fraction is shown in blue, intermediate fraction in green, and bulge-dominated fraction in red. The morphological fraction of the host galaxies of moderate-luminosity AGN evolves from being $\sim 60\%$ disk-dominated at $z \sim 2.2$ to only $\sim 20\%$ disk-dominated at $z \sim 0.6$.

mode by which galaxies of this size have grown. In particular, minor mergers (with, e.g., mass ratios of $\sim 1:5$) may not destroy a disk, although they likely lead to the formation of a significant bulge (Parry et al. 2009; Hopkins et al. 2012; Martig et al. 2012). The signatures of minor mergers are more difficult to detect, especially at higher redshifts. At $z \sim 2$, they may be impossible to detect even in a massive galaxy at the current deepest depths of CANDELS (as simulated by Schawinski et al. 2012, submitted). However, these signatures may be detectable at more moderate redshifts in the deepest *HST* data, such as that used in this thesis.

Future work to determine the effect of minor mergers on the growth of moderate-luminosity AGN ideally will involve a combination of parametric and visual morphologies. Parametric morphological analysis such as that performed in this thesis can reliably separate nuclear from host galaxy light, and subtraction of a smooth host galaxy profile can reveal faint asymmetric features characteristic of a minor merger. To quantify other signatures of minor mergers, however, requires pattern detection abilities that currently evade computer-driven algorithms. The large sample of visual classifications from Galaxy Zoo (Lintott et al. 2008, 2011) is promising in this regard, as the high number of classifications per galaxy allow scientists to characterize the likelihood a galaxy falls into a certain morphological class, accurately quantifying what is otherwise a qualitative assessment. Combining multiple merger indicators of for a sample of AGN+host galaxies as well as inactive galaxies is a promising means of assessing the role of minor mergers in the growth of black holes.

Secular (i.e., merger-free) galaxy evolution may also play an important role in black hole-galaxy co-evolution. It may be that natural processes within a galaxy evolving in relative isolation can provide enough material for a seed black hole to grow into a supermassive black hole (e.g., Ciotti & Ostriker 2012). However, disentangling this pathway to black hole growth is difficult, as hierarchical galaxy evolution dictates that most

galaxies have at least some history of minor mergers that could theoretically be mostly responsible for black hole growth. Investigation of the role of secular processes in black hole growth requires examination of that rare subset of galaxies that have undergone no merger processes strong enough to even be classified as a minor merger.

Galaxy morphologies may again provide the key to this analysis. As mergers with mass ratios as low as $1 : 10$ are thought to cause the buildup of a bulge component (Toomre 1977; Walker et al. 1996; Hopkins et al. 2012; Martig et al. 2012), selecting bulgeless galaxies places a strict mass limit on the merger activity in the formation history of such a galaxy sample. Previous work has shown that some bulgeless galaxies do indeed have central black holes (Kormendy et al. 2010, 2011; **?**), although such work has been limited to very small samples and/or very low-mass galaxies. More massive pure disk galaxies do exist, and the study of their central supermassive black holes will shed light on whether such systems obey black hole-galaxy correlations as well as providing limits on the level of black hole growth that is possible in the absence of significant merger activity.

Such work is already underway for a local sample (Simmons et al. 2012, in preparation) using Galaxy Zoo classifications to identify bulgeless galaxies and optical AGN identification from the Sloan Digital Sky Survey. This ongoing work also makes use of preliminary results from simulations similar to those described in Chapter 2, in which simulated AGN with a variety of colors and luminosities were added to real galaxies in order to assess the effects of a central point source on visual morphological analysis. The use of simulated AGN+hosts to inform analysis of real AGN+host images continues to be a highly useful method.

Lastly, the multi-wavelength SEDs of obscured AGN obtained via separation of AGN from galaxy emission provide leverage to extract a full bolometric SED of obscured AGN. This technique was developed in this thesis and has many possible uses

in addition to that described in Chapter 3. The addition of further bandpasses to the work enables a more detailed observed AGN-only SED, which allows for detailed study of AGN even in systems where the host galaxy dominates, or where higher-resolution spectra are not available.

On the other hand, the point-source SED fitting technique is still reliable even if only one band is available for host-AGN decomposition, a somewhat surprising result that enables the technique to be applied more widely. The COSMOS field, for example, is well covered at multiple wavelengths from far-infrared to X-ray, which allows for selection of highly complete samples of AGN. Multi-component SED fitting has been used in previous studies (e.g., Lusso et al. 2011, Lusso et al 2012, submitted), but such fits can be highly uncertain due to a large number of free parameters compared to the number of data points. The addition of one extra piece of information, namely an estimate of the obscuration along the line of sight to the AGN, could significantly improve the accuracy of multi-component SED fitting.

And, in systems where an independent estimate of warm/hot dust from an AGN region exists, this technique provides a comparison and potentially a way to characterize how much of the dust along the line of sight (measured by this technique) is due to dust in the AGN region versus that in the host galaxy. Combining newly-available in-depth analysis of obscured AGN and detailed host galaxy morphological information is a very promising future direction for research.

REFERENCES

Aird, J., Coil, A. L., Moustakas, J., et al., **2012**, "PRIMUS: The Dependence of AGN Accretion on Host Stellar Mass and Color," *ApJ*, 746, 90

Alexander, D. M., Bauer, F. E., Brandt, W. N., et al., **2003**, "The Chandra Deep Field North Survey. XIII. 2 Ms Point-Source Catalogs," *AJ*, 126, 539–574

Alexander, D. M., Brandt, W. N., Smail, I., et al., **2008**, "Weighing the Black Holes in z 2 Submillimeter-Emitting Galaxies Hosting Active Galactic Nuclei," *AJ*, 135, 1968–1981

Alonso-Herrero, A., Pérez-González, P. G., Rieke, G. H., et al., **2008**, "The Host Galaxies and Black Holes of Typical z~0.5-1.4 AGNs," *ApJ*, 677, 127–136

Antonucci, R., **1993**, "Unified models for active galactic nuclei and quasars," *ARA&A*, 31, 473–521

Bahcall, J. N., Kirhakos, S., Saxe, D. H., et al., **1997**, "Hubble Space Telescope Images of a Sample of 20 Nearby Luminous Quasars," *ApJ*, 479, 642–+

Ballo, L., Cristiani, S., Fasano, G., et al., **2007**, "Black Hole Masses and Eddington Ratios of AGNs at z 1: Evidence of Retriggering for a Representative Sample of X-Ray-selected AGNs," *ApJ*, 667, 97–116

Barger, A. J., Cowie, L. L., Capak, P., et al., **2003**, "Optical and Infrared Properties of the 2 Ms Chandra Deep Field North X-Ray Sources," *AJ*, 126, 632–665

Barger, A. J., Cowie, L. L., Mushotzky, R. F., et al., **2005**, "The Cosmic Evolution of Hard X-Ray-selected Active Galactic Nuclei," *AJ*, 129, 578–609

Bauer, F. E., Alexander, D. M., Brandt, W. N., et al., **2004**, "The Fall of Active Galactic Nuclei and the Rise of Star-forming Galaxies: A Close Look at the Chandra Deep Field X-Ray Number Counts," *AJ*, 128, 2048–2065

Bennert, V. N., Auger, M. W., Treu, T., et al., **2011**a, "A Local Baseline of the Black Hole Mass Scaling Relations for Active Galaxies. I. Methodology and Results of Pilot Study," *ApJ*, 726, 59

Bennert, V. N., Auger, M. W., Treu, T., et al., **2011**b, "The Relation between Black Hole Mass and Host Spheroid Stellar Mass Out to z ˜ 2," *ApJ*, 742, 107

Bennert, V. N., Treu, T., Woo, J.-H., et al., **2010**, "Cosmic Evolution of Black Holes and Spheroids. IV. The M $_{BH}$-L $_{sph}$ Relation," *ApJ*, 708, 1507–1527

Bentz, M. C., Peterson, B. M., Pogge, R. W., et al., **2006**, "The Radius-Luminosity Relationship for Active Galactic Nuclei: The Effect of Host-Galaxy Starlight on Luminosity Measurements," *ApJ*, 644, 133–142

Bertin, E. & Arnouts, S., **1996**, "SExtractor: Software for source extraction." *A&AS*, 117, 393–404

Binney, J. & Merrifield, M., **1998**, *Galactic astronomy*, Galactic astronomy / James Binney and Michael Merrifield. Princeton, NJ : Princeton University Press, 1998. (Princeton series in astrophysics) QB857 .B522 1998 ($35.00)

Binney, J. & Tremaine, S., **1987**, *Galactic dynamics*

Bluck, A. F. L., Conselice, C. J., Almaini, O., et al., **2011**, "On the co-evolution of super-massive black holes and their host galaxies since z= 3," *MNRAS*, 410, 1174–1196

Borys, C., Smail, I., Chapman, S. C., et al., **2005**, "The Relationship between Stellar and Black Hole Mass in Submillimeter Galaxies," *ApJ*, 635, 853–863

Brammer, G. B., Whitaker, K. E., van Dokkum, P. G., et al., **2009**, "The Dead Sequence: A Clear Bimodality in Galaxy Colors from z = 0 to z = 2.5," *ApJ*, 706, L173–L177

Bruzual, G. & Charlot, S., **2003**, "Stellar population synthesis at the resolution of 2003," *MNRAS*, 344, 1000–1028

Buitrago, F., Trujillo, I., Conselice, C. J., et al., **2011**, "Elliptical galaxies have been the predominant morphological class for massive galaxies since only z~1," *ArXiv e-prints*

Bundy, K., Georgakakis, A., Nandra, K., et al., **2008**, "AEGIS: New Evidence Linking Active Galactic Nuclei to the Quenching of Star Formation," *ApJ*, 681, 931–943

Calzetti, D., Armus, L., Bohlin, R. C., et al., **2000**, "The Dust Content and Opacity of Actively Star-forming Galaxies," *ApJ*, 533, 682–695

Cappelluti, N., Brusa, M., Hasinger, G., et al., **2009**, "The XMM-Newton wide-field survey in the COSMOS field. The point-like X-ray source catalogue," *A&A*, 497, 635–648

Cardamone, C. N., Moran, E. C., & Kay, L. E., **2007**, ""Hidden" Seyfert 2 Galaxies in the Chandra Deep Field North," *AJ*, 134, 1263–1275

Cardamone, C. N., Urry, C. M., Schawinski, K., et al., **2010**, "Dust-corrected Colors Reveal Bimodality in the Host-galaxy Colors of Active Galactic Nuclei at z ~ 1," *ApJ*, 721, L38–L42

Cardelli, J. A., Clayton, G. C., & Mathis, J. S., **1989**, "The relationship between infrared, optical, and ultraviolet extinction," *ApJ*, 345, 245–256

Ciotti, L., D'Ercole, A., Pellegrini, S., et al., **1991**, "Winds, outflows, and inflows in X-ray elliptical galaxies." *ApJ*, 376, 380–403

Ciotti, L. & Ostriker, J. P., **2012**, "AGN Feedback in Elliptical Galaxies: Numerical Simulations," in D.-W. Kim & S. Pellegrini, ed., "Astrophysics and Space Science Library," volume 378 of *Astrophysics and Space Science Library*, 83

Cisternas, M., Jahnke, K., Inskip, K. J., et al., **2011**, "The Bulk of the Black Hole Growth Since z ~ 1 Occurs in a Secular Universe: No Major Merger-AGN Connection," *ApJ*, 726, 57

Conselice, C. J., **2003**, "The Relationship between Stellar Light Distributions of Galaxies and Their Formation Histories," *ApJS*, 147, 1–28

Cowie, L. L., Barger, A. J., Bautz, M. W., et al., **2003**, "The Redshift Evolution of the 2-8 keV X-Ray Luminosity Function," *ApJ*, 584, L57–L60

Cowie, L. L., Barger, A. J., Hu, E. M., et al., **2004**, "A Large Sample of Spectroscopic Redshifts in the ACS-GOODS Region of the Hubble Deep Field North," *AJ*, 127, 3137–3145

Croom, S. M., Smith, R. J., Boyle, B. J., et al., **2004**, "The 2dF QSO Redshift Survey - XII. The spectroscopic catalogue and luminosity function," *MNRAS*, 349, 1397–1418

Croton, D. J., Springel, V., White, S. D. M., et al., **2006**, "The many lives of active galactic nuclei: cooling flows, black holes and the luminosities and colours of galaxies," *MNRAS*, 365, 11–28

Dasyra, K. M., Yan, L., Helou, G., et al., **2008**, "HST NICMOS imaging of z~2, 24 micron selected Ultraluminous Infrared Galaxies," *ArXiv e-prints*, 802

Davis, M., Guhathakurta, P., Konidaris, N. P., et al., **2007**, "The All-Wavelength Extended Groth Strip International Survey (AEGIS) Data Sets," *ApJ*, 660, L1–L6

Decarli, R., Falomo, R., Treves, A., et al., **2010**, "The quasar MBH-Mhost relation through cosmic time - II. Evidence for evolution from z = 3 to the present age," *MNRAS*, 402, 2453–2461

Devecchi, B., Volonteri, M., Rossi, E. M., et al., **2012**, "High-redshift formation and evolution of central massive objects - II. The census of BH seeds," *MNRAS*, 421, 1465–1475

Di Matteo, T., Springel, V., & Hernquist, L., **2005**, "Energy input from quasars regulates the growth and activity of black holes and their host galaxies," *Nature*, 433, 604–607

Draine, B. T., **2003**, "Scattering by Interstellar Dust Grains. I. Optical and Ultraviolet," *ApJ*, 598, 1017–1025

Draine, B. T. & Li, A., **2007**, "Infrared Emission from Interstellar Dust. IV. The Silicate-Graphite-PAH Model in the Post-Spitzer Era," *ApJ*, 657, 810–837

Elitzur, M. & Shlosman, I., **2006**, "The AGN-obscuring Torus: The End of the "Doughnut" Paradigm?" *ApJ*, 648, L101–L104

Elvis, M., Risaliti, G., & Zamorani, G., **2002**, "Most Supermassive Black Holes Must Be Rapidly Rotating," *ApJ*, 565, L75–L77

Elvis, M., Wilkes, B. J., McDowell, J. C., et al., **1994**, "Atlas of quasar energy distributions," *ApJS*, 95, 1–68

Fabian, A. C. & Iwasawa, K., **1999**, "The mass density in black holes inferred from the X-ray background," *MNRAS*, 303, L34–L36

Fan, X., Strauss, M. A., Schneider, D. P., et al., **2001**, "High-Redshift Quasars Found in Sloan Digital Sky Survey Commissioning Data. IV. Luminosity Function from the Fall Equatorial Stripe Sample," *AJ*, 121, 54–65

Ferrarese, L. & Ford, H., **2005**, "Supermassive Black Holes in Galactic Nuclei: Past, Present and Future Research," *Space Science Reviews*, 116, 523–624

Ferrarese, L. & Ford, H. C., **1999**, "Nuclear Disks of Gas and Dust in Early-Type Galaxies and the Hunt for Massive Black Holes: Hubble Space Telescope Observations of NGC 6251," *ApJ*, 515, 583–602

Ferrarese, L. & Merritt, D., **2000**, "A Fundamental Relation between Supermassive Black Holes and Their Host Galaxies," *ApJ*, 539, L9–L12

Ford, H. C., Harms, R. J., Tsvetanov, Z. I., et al., **1994**, "Narrowband HST images of M87: Evidence for a disk of ionized gas around a massive black hole," *ApJ*, 435, L27–L30

Gabor, J. M., Impey, C. D., Jahnke, K., et al., **2009**, "Active Galactic Nucleus Host Galaxy Morphologies in COSMOS," *ApJ*, 691, 705–722

Gebhardt, K., Bender, R., Bower, G., et al., **2000**, "A Relationship between Nuclear Black Hole Mass and Galaxy Velocity Dispersion," *ApJ*, 539, L13–L16

Genzel, R., Eckart, A., Ott, T., et al., **1997**, "On the nature of the dark mass in the centre of the Milky Way," *MNRAS*, 291, 219–234

Ghez, A. M., Salim, S., Hornstein, S. D., et al., **2005**, "Stellar Orbits around the Galactic Center Black Hole," *ApJ*, 620, 744–757

Giacconi, R., Zirm, A., Wang, J., et al., **2002**, "Chandra Deep Field South: The 1 Ms Catalog," *ApJS*, 139, 369–410

Giavalisco, M., Ferguson, H. C., Koekemoer, A. M., et al., **2004**, "The Great Observatories Origins Deep Survey: Initial Results from Optical and Near-Infrared Imaging," *ApJ*, 600, L93–L98

Glikman, E., Bogosavljević, M., Djorgovski, S. G., et al., **2010**, "The Faint End of the Quasar Luminosity Function at z ˜ 4," *ApJ*, 710, 1498–1514

Glikman, E., Gregg, M. D., Lacy, M., et al., **2004**, "FIRST-2Mass Sources below the APM Detection Threshold: A Population of Highly Reddened Quasars," *ApJ*, 607, 60–75

Glikman, E., Helfand, D. J., White, R. L., et al., **2007**, "The FIRST-2MASS Red Quasar Survey," *ApJ*, 667, 673–703

Graham, A. W., **2001**, "An Investigation into the Prominence of Spiral Galaxy Bulges," *AJ*, 121, 820–840

Graham, A. W., **2007**, "The black hole mass - spheroid luminosity relation," *MNRAS*, 379, 711–722

Greene, J. E. & Ho, L. C., **2007**, "The Mass Function of Active Black Holes in the Local Universe," *ApJ*, 667, 131–148

Greenhill, L. J., Kondratko, P. T., Lovell, J. E. J., et al., **2003**, "The Discovery of $H_2O Maser Emission in Seven Active Galactic Nuclei and at High Velocities in the Circinus Ga$ $-L14$

Grogin, N. A., Conselice, C. J., Chatzichristou, E., et al., **2005**, "AGN Host Galaxies at z˜0.4-1.3: Bulge-dominated and Lacking Merger-AGN Connection," *ApJ*, 627, L97–L100

Grogin, N. A., Kocevski, D. D., Faber, S. M., et al., **2011**, "CANDELS: The Cosmic Assembly Near-infrared Deep Extragalactic Legacy Survey," *ApJS*, 197, 35

Grogin, N. A., Koekemoer, A. M., Schreier, E. J., et al., **2003**, "Hubble Space Telescope Imaging in the Chandra Deep Field-South. III. Quantitative Morphology of the 1 Million Second Chandra Counterparts and Comparison with the Field Population," *ApJ*, 595, 685–697

Gültekin, K., Richstone, D. O., Gebhardt, K., et al., **2009**, "The M-σ and M-L Relations in Galactic Bulges, and Determinations of Their Intrinsic Scatter," *ApJ*, 698, 198–221

Hambleton, K. M., Gibson, B. K., Brook, C. B., et al., **2011**, "Advanced morphological galaxy classification: a comparison of observed and simulated galaxies," *MNRAS*, 418, 801–810

Häring, N. & Rix, H.-W., **2004**, "On the Black Hole Mass-Bulge Mass Relation," *ApJ*, 604, L89–L92

Hasinger, G., Miyaji, T., & Schmidt, M., **2005**, "Luminosity-dependent evolution of soft X-ray selected AGN. New Chandra and XMM-Newton surveys," *A&A*, 441, 417–434

Häussler, B., McIntosh, D. H., Barden, M., et al., **2007**, "GEMS: Galaxy Fitting Catalogs and Testing Parametric Galaxy Fitting Codes: GALFIT and GIM2D," *ApJS*, 172, 615–633

Heckman, T. M., Kauffmann, G., Brinchmann, J., et al., **2004**, "Present-Day Growth of Black Holes and Bulges: The Sloan Digital Sky Survey Perspective," *ApJ*, 613, 109–118

Heger, A., Fryer, C. L., Woosley, S. E., et al., **2003**, "How Massive Single Stars End Their Life," *ApJ*, 591, 288–300

Herrnstein, J. R., Moran, J. M., Greenhill, L. J., et al., **1999**, "A geometric distance to the galaxy NGC4258 from orbital motions in a nuclear gas disk," *Nature*, 400, 539–541

Hickox, R. C., Jones, C., Forman, W. R., et al., **2009**, "Host Galaxies, Clustering, Eddington Ratios, and Evolution of Radio, X-Ray, and Infrared-Selected AGNs," *ApJ*, 696, 891–919

Hönig, S. F., Beckert, T., Ohnaka, K., et al., **2006**, "Radiative transfer modeling of three-dimensional clumpy AGN tori and its application to NGC 1068," *A&A*, 452, 459–471

Hopkins, P. F. & Hernquist, L., **2009**, "Quasars Are Not Light Bulbs: Testing Models of Quasar Lifetimes with the Observed Eddington Ratio Distribution," *ApJ*, 698, 1550–1569

Hopkins, P. F., Hernquist, L., Cox, T. J., et al., **2006**a, "The Evolution in the Faint-End Slope of the Quasar Luminosity Function," *ApJ*, 639, 700–709

Hopkins, P. F., Kere*V* s, D., Murray, N., et al., **2012**, "Stellar feedback and bulge formation in clumpy discs," *MNRAS*, 427, 968–978

Hopkins, P. F., Richards, G. T., & Hernquist, L., **2007**, "An Observational Determination of the Bolometric Quasar Luminosity Function," *ApJ*, 654, 731–753

Hopkins, P. F., Somerville, R. S., Hernquist, L., et al., **2006**b, "The Relation between Quasar and Merging Galaxy Luminosity Functions and the Merger-driven Star Formation History of the Universe," *ApJ*, 652, 864–888

Hopkins, P. F., Strauss, M. A., Hall, P. B., et al., **2004**, "Dust Reddening in Sloan Digital Sky Survey Quasars," *AJ*, 128, 1112–1123

Hubble, E. P., **1926**, "Extragalactic nebulae." *ApJ*, 64, 321–369

Inskip, K. J., Jahnke, K., Rix, H.-W., et al., **2011**, "Resolving the Dynamical Mass of a z ˜ 1.3 Quasi-stellar Object Host Galaxy Using SINFONI and Laser Guide Star Assisted Adaptive Optics," *ApJ*, 739, 90

Jahnke, K., Bongiorno, A., Brusa, M., et al., **2009**, "Massive Galaxies in COSMOS: Evolution of Black Hole Versus Bulge Mass but not Versus Total Stellar Mass Over the Last 9 Gyr?" *ApJ*, 706, L215–L220

Jogee, S., Barazza, F. D., Rix, H.-W., et al., **2004**, "Bar Evolution over the Last 8 Billion Years: A Constant Fraction of Strong Bars in the GEMS Survey," *ApJ*, 615, L105–L108

Kartaltepe, J. S., **2009**, *A multiwavelength study of (ultra)luminous infrared galaxies in the cosmos field*, Ph.D. thesis, University of Hawai'i at Manoa

Kartaltepe, J. S., Dickinson, M., Alexander, D. M., et al., **2011**, "GOODS-Herschel CANDELS: The Morphologies of Ultraluminous Infrared Galaxies at z˜2," *ArXiv e-prints*

Kaspi, S., Maoz, D., Netzer, H., et al., **2005**, "The Relationship between Luminosity and Broad-Line Region Size in Active Galactic Nuclei," *ApJ*, 629, 61–71

Kauffmann, G. & Haehnelt, M., **2000**, "A unified model for the evolution of galaxies and quasars," *MNRAS*, 311, 576–588

Kauffmann, G. & Heckman, T. M., **2009**, "Feast and Famine: regulation of black hole growth in low-redshift galaxies," *MNRAS*, 397, 135–147

Kauffmann, G., White, S. D. M., & Guiderdoni, B., **1993**, "The Formation and Evolution of Galaxies Within Merging Dark Matter Haloes," *MNRAS*, 264, 201–+

Kelly, B. C., Vestergaard, M., Fan, X., et al., **2010**, "Constraints on Black Hole Growth, Quasar Lifetimes, and Eddington Ratio Distributions from the SDSS Broad-line Quasar Black Hole Mass Function," *ApJ*, 719, 1315–1334

King, A. R., **2010**, "AGN have underweight black holes and reach Eddington," *MNRAS*, 408, L95–L98

Kocevski, D. D., Faber, S. M., Mozena, M., et al., **2011**, "CANDELS: Constraining the AGN-Merger Connection with Host Morphologies at z~2," *ArXiv e-prints*

Kochanek, C. S., Eisenstein, D., Caldwell, N., et al., **2004**, "The AGN and Galaxy Evolution Survey," in "Bulletin of the American Astronomical Society," volume 36 of *Bulletin of the American Astronomical Society*, 1495–+

Koekemoer, A. M., Faber, S. M., Ferguson, H. C., et al., **2011**, "CANDELS: The Cosmic Assembly Near-infrared Deep Extragalactic Legacy SurveyThe Hubble Space Telescope Observations, Imaging Data Products, and Mosaics," *ApJS*, 197, 36

Koekemoer, A. M., Fruchter, A. S., Hook, R. N., et al., **2002**, "MultiDrizzle: An Integrated Pyraf Script for Registering, Cleaning and Combining Images," in "The 2002 HST Calibration Workshop : Hubble after the Installation of the ACS and the NICMOS Cooling System, Proceedings of a Workshop held at the Space Telescope Science Institute, Baltimore, Maryland, October 17 and 18, 2002. Edited by Santiago Arribas, Anton Koekemoer, and Brad Whitmore. Baltimore, MD: Space Telescope Science Institute, 2002., p.339," 339–+

Kollmeier, J. A., Onken, C. A., Kochanek, C. S., et al., **2006**, "Black Hole Masses and Eddington Ratios at 0.3 z 4," *ApJ*, 648, 128–139

Kormendy, J., Bender, R., & Cornell, M. E., **2011**, "Supermassive black holes do not correlate with galaxy disks or pseudobulges," *Nature*, 469, 374–376

Kormendy, J., Drory, N., Bender, R., et al., **2010**, "Bulgeless Giant Galaxies Challenge Our Picture of Galaxy Formation by Hierarchical Clustering," *ApJ*, 723, 54–80

Kormendy, J. & Richstone, D., **1995**, "Inward Bound—The Search For Supermassive Black Holes In Galactic Nuclei," *ARA&A*, 33, 581–+

Kriek, M., van Dokkum, P. G., Labbé, I., et al., **2009**, "An Ultra-Deep Near-Infrared Spectrum of a Compact Quiescent Galaxy at z = 2.2," *ApJ*, 700, 221–231

Krist, J., **1993**, "Tiny Tim : an HST PSF Simulator," in R. J. Hanisch, R. J. V. Brissenden, & J. Barnes, ed., "Astronomical Data Analysis Software and Systems II," volume 52 of *Astronomical Society of the Pacific Conference Series*, 536–+

La Franca, F., Fiore, F., Comastri, A., et al., **2005**, "The HELLAS2XMM Survey. VII. The Hard X-Ray Luminosity Function of AGNs up to z = 4: More Absorbed AGNs at Low Luminosities and High Redshifts," *ApJ*, 635, 864–879

Lilly, S. J., Le Fevre, O., Hammer, F., et al., **1996**, "The Canada-France Redshift Survey: The Luminosity Density and Star Formation History of the Universe to Z approximately 1," *ApJ*, 460, L1

Lintott, C., Schawinski, K., Bamford, S., et al., **2011**, "Galaxy Zoo 1: data release of morphological classifications for nearly 900 000 galaxies," *MNRAS*, 410, 166–178

Lintott, C. J., Schawinski, K., Slosar, A., et al., **2008**, "Galaxy Zoo: morphologies derived from visual inspection of galaxies from the Sloan Digital Sky Survey," *MNRAS*, 389, 1179–1189

Lodato, G. & Natarajan, P., **2006**, "Supermassive black hole formation during the assembly of pre-galactic discs," *MNRAS*, 371, 1813–1823

Lodato, G. & Natarajan, P., **2007**, "The mass function of high-redshift seed black holes," *MNRAS*, 377, L64–L68

Lusso, E., Comastri, A., Vignali, C., et al., **2011**, "The bolometric output and host-galaxy properties of obscured AGN in the XMM-COSMOS survey," *A&A*, 534, A110

Madau, P., Pozzetti, L., & Dickinson, M., **1998**, "The Star Formation History of Field Galaxies," *ApJ*, 498, 106–+

Madau, P. & Rees, M. J., **2001**, "Massive Black Holes as Population III Remnants," *ApJ*, 551, L27–L30

Magorrian, J., Tremaine, S., Richstone, D., et al., **1998**, "The Demography of Massive Dark Objects in Galaxy Centers," *AJ*, 115, 2285–2305

Mainieri, V., Rosati, P., Tozzi, P., et al., **2005**, "The Chandra deep field South/GOODS survey. Optically faint X-ray sources," *A&A*, 437, 805–821

Maiolino, R., Marconi, A., Salvati, M., et al., **2001**, "Dust in active nuclei. I. Evidence for "anomalous" properties," *A&A*, 365, 28–36

Maiolino, R., Ruiz, M., Rieke, G. H., et al., **1997**, "Molecular Gas, Morphology, and Seyfert Galaxy Activity," *ApJ*, 485, 552–+

Malkan, M. A., Gorjian, V., & Tam, R., **1998**, "A Hubble Space Telescope Imaging Survey of Nearby Active Galactic Nuclei," *ApJS*, 117, 25

Maraston, C., **2005**, "Evolutionary population synthesis: models, analysis of the ingredients and application to high-z galaxies," *MNRAS*, 362, 799–825

Marconi, A. & Hunt, L. K., **2003**, "The Relation between Black Hole Mass, Bulge Mass, and Near-Infrared Luminosity," *ApJ*, 589, L21–L24

Marconi, A., Risaliti, G., Gilli, R., et al., **2004**, "Local supermassive black holes, relics of active galactic nuclei and the X-ray background," *MNRAS*, 351, 169–185

Marleau, F. R. & Simard, L., **1998**, "Quantitative Morphology of Galaxies in the Hubble Deep Field," *ApJ*, 507, 585–600

Martig, M., Bournaud, F., Croton, D. J., et al., **2012**, "A Diversity of Progenitors and Histories for Isolated Spiral Galaxies," *ApJ*, 756, 26

Martin, N., Maurice, E., & Lequeux, J., **1989**, "The structure of the Small Magellanic Cloud," *A&A*, 215, 219–242

Mathis, J. S., Mezger, P. G., & Panagia, N., **1983**, "Interstellar radiation field and dust temperatures in the diffuse interstellar matter and in giant molecular clouds," *A&A*, 128, 212–229

McLure, R. J. & Dunlop, J. S., **2001**, "The black hole masses of Seyfert galaxies and quasars," *MNRAS*, 327, 199–207

McLure, R. J. & Dunlop, J. S., **2002**, "On the black hole-bulge mass relation in active and inactive galaxies," *MNRAS*, 331, 795–804

Merloni, A., Bongiorno, A., Bolzonella, M., et al., **2010**, "On the Cosmic Evolution of the Scaling Relations Between Black Holes and Their Host Galaxies: Broad-Line Active Galactic Nuclei in the zCOSMOS Survey," *ApJ*, 708, 137–157

Miyoshi, M., Moran, J., Herrnstein, J., et al., **1995**, "Evidence for a Black-Hole from High Rotation Velocities in a Sub-Parsec Region of NGC4258," *Nature*, 373, 127–+

Mushotzky, R. F., Winter, L. M., McIntosh, D. H., et al., **2008**, "Correlations of the IR Luminosity and Eddington Ratio with a Hard X-Ray-Selected Sample of Active Galactic Nuclei," *ApJ*, 684, L65–L68

Netzer, H., Lira, P., Trakhtenbrot, B., et al., **2007**a, "Black Hole Mass and Growth Rate at High Redshift," *ApJ*, 671, 1256–1263

Netzer, H., Lutz, D., Schweitzer, M., et al., **2007**b, "Spitzer Quasar and ULIRG Evolution Study (QUEST). II. The Spectral Energy Distributions of Palomar-Green Quasars," *ApJ*, 666, 806–816

Netzer, H. & Trakhtenbrot, B., **2007**, "Cosmic Evolution of Mass Accretion Rate and Metallicity in Active Galactic Nuclei," *ApJ*, 654, 754–763

Parry, O. H., Eke, V. R., & Frenk, C. S., **2009**, "Galaxy morphology in the ΛCDM cosmology," *MNRAS*, 396, 1972–1984

Peng, C. Y., Ho, L. C., Impey, C. D., et al., **2002**, "Detailed Structural Decomposition of Galaxy Images," *AJ*, 124, 266–293

Peng, C. Y., Ho, L. C., Impey, C. D., et al., **2010**, "Detailed Decomposition of Galaxy Images. II. Beyond Axisymmetric Models," *AJ*, 139, 2097–2129

Peng, C. Y., Impey, C. D., Ho, L. C., et al., **2006**, "Probing the Coevolution of Supermassive Black Holes and Quasar Host Galaxies," *ApJ*, 640, 114–125

Persic, M., Rephaeli, Y., Braito, V., et al., **2004**, "2-10 keV luminosity of high-mass binaries as a gauge of ongoing star-formation rate," *A&A*, 419, 849–862

Peterson, B. M., **1993**, "Reverberation mapping of active galactic nuclei," *PASP*, 105, 247–268

Peterson, B. M. & Wandel, A., **2000**, "Evidence for Supermassive Black Holes in Active Galactic Nuclei from Emission-Line Reverberation," *ApJ*, 540, L13–L16

Pierce, C. M., Lotz, J. M., Laird, E. S., et al., **2007**, "AEGIS: Host Galaxy Morphologies of X-Ray-selected and Infrared-selected Active Galactic Nuclei at 0.2 = z 1.2," *ApJ*, 660, L19–L22

Pierce, C. M., Lotz, J. M., Primack, J. R., et al., **2010**a, "The effects of an active galactic nucleus on host galaxy colour and morphology measurements," *MNRAS*, 405, 718–734

Pierce, C. M., Lotz, J. M., Salim, S., et al., **2010**b, "Host galaxy colour gradients and accretion disc obscuration in AEGIS z ˜ 1 X-ray-selected active galactic nuclei," *MNRAS*, 408, 139–156

Ravindranath, S., Ferguson, H. C., Conselice, C., et al., **2004**, "The Evolution of Disk Galaxies in the GOODS-South Field: Number Densities and Size Distribution," *ApJ*, 604, L9–L12

Richards, G. T., Lacy, M., Storrie-Lombardi, L. J., et al., **2006**, "Spectral Energy Distributions and Multiwavelength Selection of Type 1 Quasars," *ApJS*, 166, 470–497

Rix, H.-W., Barden, M., Beckwith, S. V. W., et al., **2004**, "GEMS: Galaxy Evolution from Morphologies and SEDs," *ApJS*, 152, 163–173

Rosario, D. J., Mozena, M., Wuyts, S., et al., **2011**, "X-ray selected AGN Hosts are Similar to Inactive Galaxies out to z=3: Results from CANDELS/CDF-S," *ArXiv e-prints*

Sánchez, S. F., Jahnke, K., Wisotzki, L., et al., **2004**, "Colors of Active Galactic Nucleus Host Galaxies at 0.5z1.1 from the GEMS Survey," *ApJ*, 614, 586–606

Sanders, D. B., Soifer, B. T., Elias, J. H., et al., **1988**, "Ultraluminous infrared galaxies and the origin of quasars," *ApJ*, 325, 74–91

Sarajedini, V. L., Koo, D. C., Phillips, A. C., et al., **2006**, "The DEEP Groth Strip Survey. VI. Spectroscopic, Variability, and X-Ray Detection of Active Galactic Nuclei," *ApJS*, 166, 69–88

Schawinski, K., Treister, E., Urry, C. M., et al., **2011**, "HST WFC3/IR Observations of Active Galactic Nucleus Host Galaxies at z ˜ 2: Supermassive Black Holes Grow in Disk Galaxies," *ApJ*, 727, L31+

Schawinski, K., Virani, S., Simmons, B., et al., **2009**, "Do Moderate-Luminosity Active Galactic Nuclei Suppress Star Formation?" *ApJ*, 692, L19–L23

Schmidt, M., **1963**, "3C 273 : A Star-Like Object with Large Red-Shift," *Nature*, 197, 1040

Schneider, D. P., Hall, P. B., Richards, G. T., et al., **2007**, "The Sloan Digital Sky Survey Quasar Catalog. IV. Fifth Data Release," *AJ*, 134, 102–117

Scoville, N., Aussel, H., Brusa, M., et al., **2007**, "The Cosmic Evolution Survey (COSMOS): Overview," *ApJS*, 172, 1–8

Sérsic, J. L., **1968**, *Atlas de galaxias australes*, Cordoba, Argentina: Observatorio Astronomico, 1968

Shakura, N. I. & Sunyaev, R. A., **1973**, "Black holes in binary systems. Observational appearance." *A&A*, 24, 337–355

Sheth, K., Elmegreen, D. M., Elmegreen, B. G., et al., **2008**, "Evolution of the Bar Fraction in COSMOS: Quantifying the Assembly of the Hubble Sequence," *ApJ*, 675, 1141–1155

Shull, J. M. & van Steenberg, M. E., **1985**, "Galactic interstellar abundance surveys with IUE. I - Neutral hydrogen," *ApJ*, 294, 599–614

Simard, L., Koo, D. C., Faber, S. M., et al., **1999**, "The Magnitude-Size Relation of Galaxies out to z~1," *ApJ*, 519, 563–579

Simmons, B. D. & Urry, C. M., **2008**, "The Accuracy of Morphological Decomposition of Active Galactic Nucleus Host Galaxies," *ApJ*, 683, 644–658

Simmons, B. D., Van Duyne, J., Urry, C. M., et al., **2011**, "Obscured GOODS Active Galactic Nuclei and Their Host Galaxies at z 1.25: The Slow Black Hole Growth Phase," *ApJ*, 734, 121–+

Somerville, R. S., Hopkins, P. F., Cox, T. J., et al., **2008**, "A semi-analytic model for the co-evolution of galaxies, black holes and active galactic nuclei," *MNRAS*, 391, 481–506

Spergel, D. N., Verde, L., Peiris, H. V., et al., **2003**, "First-Year Wilkinson Microwave Anisotropy Probe (WMAP) Observations: Determination of Cosmological Parameters," *ApJS*, 148, 175–194

Steinhardt, C. L. & Elvis, M., **2011**, "The quasar mass-luminosity plane - II. High mass turn-off evolution and a synchronization puzzle," *MNRAS*, 410, 201–209

Szokoly, G. P., Bergeron, J., Hasinger, G., et al., **2004**, "The Chandra Deep Field-South: Optical Spectroscopy. I." *ApJS*, 155, 271–349

Taylor, E. N., Franx, M., van Dokkum, P. G., et al., **2009**, "A Public, K-Selected, Optical-to-Near-Infrared Catalog of the Extended Chandra Deep Field South (ECDFS) from the Multiwavelength Survey by Yale-Chile (MUSYC)," *ApJS*, 183, 295–319

Taylor, M. B., **2005**, "TOPCAT STIL: Starlink Table/VOTable Processing Software," in P. Shopbell, M. Britton, & R. Ebert, eds., "Astronomical Data Analysis Software and Systems XIV," volume 347 of *Astronomical Society of the Pacific Conference Series*, 29

Toomre, A., **1977**, "Mergers and Some Consequences," in B. M. Tinsley & R. B. G. Larson D. Campbell, ed., "Evolution of Galaxies and Stellar Populations," 401

Trakhtenbrot, B. & Netzer, H., **2010**, "The evolution of M_*/M_{BH} between z = 2 and z = 0," *MNRAS*, 406, L35–L39

Treister, E., Krolik, J. H., & Dullemond, C., **2008**, "Measuring the Fraction of Obscured Quasars by the Infrared Luminosity of Unobscured Quasars," *ApJ*, 679, 140–148

Treister, E. & Urry, C. M., **2005**, "Active Galactic Nuclei Unification and the X-Ray Background," *ApJ*, 630, 115–121

Treister, E. & Urry, C. M., **2006**, "The Evolution of Obscuration in Active Galactic Nuclei," *ApJ*, 652, L79–L82

Treister, E. & Urry, C. M., **2012**, "The Cosmic History of Black Hole Growth from Deep Multiwavelength Surveys," *Advances in Astronomy*, 2012

Treister, E., Urry, C. M., Chatzichristou, E., et al., **2004**, "Obscured Active Galactic Nuclei and the X-Ray, Optical, and Far-Infrared Number Counts of Active Galactic Nuclei in the GOODS Fields," *ApJ*, 616, 123–135

Treister, E., Urry, C. M., Van Duyne, J., et al., **2006**, "Spitzer Number Counts of Active Galactic Nuclei in the GOODS Fields," *ApJ*, 640, 603–611

Treister, E., Urry, C. M., & Virani, S., **2009**, "The Space Density of Compton-Thick Active Galactic Nucleus and the X-Ray Background," *ApJ*, 696, 110–120

Tremaine, S., Gebhardt, K., Bender, R., et al., **2002**, "The Slope of the Black Hole Mass versus Velocity Dispersion Correlation," *ApJ*, 574, 740–753

Treu, T., Malkan, M. A., & Blandford, R. D., **2004**, "The Relation Between Black Hole Mass and Velocity Dispersion at z ˜ 0.37," *ApJ*, 615, L97–L100

Trujillo, I. & Aguerri, J. A. L., **2004**, "Quantitative morphological analysis of the Hubble Deep Field North and Hubble Deep Field South - I. Early- and late-type luminosity-size relations of galaxies out to z˜ 1," *MNRAS*, 355, 82–96

Ueda, Y., Akiyama, M., Ohta, K., et al., **2003**, "Cosmological Evolution of the Hard X-Ray Active Galactic Nucleus Luminosity Function and the Origin of the Hard X-Ray Background," *ApJ*, 598, 886–908

Urrutia, T., Lacy, M., & Becker, R. H., **2008**, "Evidence for Quasar Activity Triggered by Galaxy Mergers in HST Observations of Dust-reddened Quasars," *ApJ*, 674, 80–96

Urry, C. M., Falomo, R., Scarpa, R., et al., **1999**, "Hubble Space Telescope Observations of the Host Galaxies of BL Lacertae Objects," *ApJ*, 512, 88–99

Urry, C. M. & Padovani, P., **1995**, "Unified Schemes for Radio-Loud Active Galactic Nuclei," *PASP*, 107, 803–+

Vestergaard, M., **2002**, "Determining Central Black Hole Masses in Distant Active Galaxies," *ApJ*, 571, 733–752

Vestergaard, M. & Peterson, B. M., **2006**, "Determining Central Black Hole Masses in Distant Active Galaxies and Quasars. II. Improved Optical and UV Scaling Relationships," *ApJ*, 641, 689–709

Volonteri, M., Lodato, G., & Natarajan, P., **2008**, "The evolution of massive black hole seeds," *MNRAS*, 383, 1079–1088

Walker, I. R., Mihos, J. C., & Hernquist, L., **1996**, "Quantifying the Fragility of Galactic Disks in Minor Mergers," *ApJ*, 460, 121

Wall, J. V., Jackson, C. A., Shaver, P. A., et al., **2005**, "The Parkes quarter-Jansky flat-spectrum sample. III. Space density and evolution of QSOs," *A&A*, 434, 133–148

Whitaker, K. E., Labbé, I., van Dokkum, P. G., et al., **2011**, "The NEWFIRM Medium-band Survey: Photometric Catalogs, Redshifts, and the Bimodal Color Distribution of Galaxies out to z ˜ 3," *ApJ*, 735, 86

White, S. D. M. & Rees, M. J., **1978**, "Core condensation in heavy halos - A two-stage theory for galaxy formation and clustering," *MNRAS*, 183, 341–358

Willott, C. J., Simpson, C., Almaini, O., et al., **2004**, "Dust and Gas Obscuration in ELAIS Deep X-Ray Survey Reddened Quasars," *ApJ*, 610, 140–150

Wirth, G. D., Willmer, C. N. A., Amico, P., et al., **2004**, "The Team Keck Treasury Redshift Survey of the GOODS-North Field," *AJ*, 127, 3121–3136

Woo, J., Treu, T., Malkan, M. A., et al., **2008**, "Cosmic Evolution of Black Holes and Spheroids. III. The $M_{BH} - \sigma_* Relation in the Last Six Billion Years$," *ApJ*, 681, 925 − −930

Woo, J. & Urry, C. M., **2002**, "The Independence of Active Galactic Nucleus Black Hole Mass and Radio Loudness," *ApJ*, 581, L5–L7

Woo, J.-H., Urry, C. M., van der Marel, R. P., et al., **2005**, "Black Hole Masses and Host Galaxy Evolution of Radio-Loud Active Galactic Nuclei," *ApJ*, 631, 762–772

Wright, E. L., **2006**, "A Cosmology Calculator for the World Wide Web," *PASP*, 118, 1711–1715

Xue, Y. Q., Luo, B., Brandt, W. N., et al., **2011**, "The Chandra Deep Field-South Survey: 4 Ms Source Catalogs," *ApJS*, 195, 10–+

Yu, Q. & Lu, Y., **2008**, "Toward Precise Constraints on the Growth of Massive Black Holes," *ApJ*, 689, 732–754